

QUALITY IN SELECTIVE LASER MELTING OF ALUMINUM ALLOYS

DIMENSIONAL ACCURACY AND SURFACE ROUGHNESS IN SELECTIVE LASER MELTING OF
ALUMINUM ALLOYS

By
YI FU XUE, B. TECH.
(McMaster University, Canada)

A Thesis
Submitted to the School of Graduate Studies
In Partial Fulfillment of the Requirements
For the Degree
Master of Applied Science

McMaster University
© Copyright by Yi Fu Xue, February 2019

McMaster University MASTER OF APPLIED SCIENCE (2019) Hamilton, Ontario

TITLE: Dimensional Accuracy and Surface Roughness in Selective Laser Melting of Aluminum Alloys

AUTHOR: Yi Fu Xue, B. Tech. (McMaster University)

SUPERVISOR: Dr. M.A. Elbestawi

NUMBER OF PAGES: XI, 117

Abstract

Additive manufacturing (AM) has the ability to fabricate components of high geometric complexity that are difficult or near impossible to be produced by traditional manufacturing technologies. Selective laser melting (SLM) is a commonly used AM technology for metallic fabrications. SLM offers the opportunities to customize the characteristics of the as-built part produced, by adjusting the laser settings. However, high strength aluminum (Al) alloys presents an obstacle for SLM production due to the low alloying content, which increases the alloys' probabilities to form cracks due to thermal stress induced by the SLM build process. The current study focuses on the study of surface roughness and dimensional accuracy of SLM fabrication of Al6061 and AlSi10Mg. Using design of experiment (DOE), wide ranges SLM process parameters were experimented with, and their individual effect along with their interactive effects on the fabricated parts' quality were evaluated. The quality characteristics studied are: microstructures, microhardness, tensile strength (ultimate tensile strength, and yield strength), density, surface roughness, and dimensional accuracy. Regression models were created for each quality characteristics, and the combination of density, surface roughness, and dimensional accuracy results was used to create processing window for SLM that ensures the production of high-quality parts. The work aims to not only be used as-is, to help with the selection of SLM process parameters for Al6061 and AlSi10Mg that will reduce the post-processing time, but also to set a foundation for future development for numerical models that could better predict and describe the relations between SLM process parameters and the part's fundamental qualities.

Acknowledgements:

I would like to acknowledge my supervisor Dr. Elbestawi for guiding me through this endeavor and pushing me pass my limits. I would also like to thank Dr. Singh for being my mentor, seeing the potential in me, and provided me with this opportunity.

I would like to give thanks to Dr. Maamoun for being on this journey with me and being a mentor to me. I am thankful for our collaborations and the works we have accomplished.

I would like to give thanks to Dr. Yakout and the colleagues of AMG, for supporting me. You have made my stay in the office enjoyable.

Thank you to Mohawk College for providing this opportunity for me, as well as the providing me with the valuable teaching experience.

Lastly, I would like to thank my parents. This past six years had been one of the biggest journeys I had taken. From undergraduate to graduate school, I had certainly changed a lot, but you were always there for me. Here I dedicate this work to you, mom and dad.

And the light shineth in darkness; and the darkness comprehended it not.

(John 1:5, King James Version).

Table of Contents

Abstract	I
Acknowledgements:.....	II
List of figures.....	VI
List of tables.....	IX
List of abbreviations and symbols.....	X
Declaration of Academic Achievement	XI
1. Introduction.....	1
1.1. Overview of Additive Manufacturing	1
1.2. Selective Laser Melting	3
1.3. Challenges and current solutions.....	5
1.3.1. Alloy content change.....	6
1.3.2. Alloy mixing	6
1.4. Current work.....	9
2. Literature review	10
2.1. Introduction	10
2.2. Process parameters.....	12
2.3. Surface Roughness	31
2.4. The staircase-effect	33
3. Experimental work.....	43
3.1. Introduction	43
3.2. Design of Experiment	46
3.2.1. Method.....	46
3.2.2. Experiment	54
3.3. Microstructure and mechanical properties	58
3.3.1. Microstructure.....	58
3.3.2. Mechanical properties.....	59
3.4. Density, Surface roughness, and Dimensional accuracy	61
3.4.1. Density.....	61
3.4.2. Surface roughness	62
3.4.3. Dimensional accuracy.....	63
4. Results and Discussion	64
4.1. Powder characterization	64
4.2. Microstructure	69
4.2.1. AlSi10Mg.....	69

4.2.2. Al6061	75
4.3. Mechanical Properties.....	79
4.3.1. Microhardness.....	79
4.3.2. Tensile behaviour	84
4.4. Physical Properties	88
4.4.1. Density.....	88
4.4.2. Surface roughness	92
4.4.3. Dimensional accuracy.....	98
4.5. Optimal processing window	102
5. Conclusion	107
5.1. Future research suggestions	108
Bibliography.....	109

List of figures

FIGURE 1.1-1 SCHEMATIC OF SELECTIVE LASER MELTING PROCESS [16].	3
FIGURE 1.2-3 TEMPERATURE PROFILE DURING THE LAYER-BY-LAYER PROCESS OF SLM [16].	4
FIGURE 1.2-3 THE COMPLEX MICROSTRUCTURE OF Ti-6Al-4V RESULTING FROM RAPID MELTING AND COOLING FROM THE SLM PROCESS [16].	4
FIGURE 1.3-1 MICROGRAPH OF POLISHED SAMPLES. ADDITION OF 0%WT A), 1%WT B), AND 2%WT C) OF ALSi10MG POWDER DISPLAYED HOT TEARING. 3%WT D), AND 4%WT E) OF ALSi10MG ADDITION SHOWED NO SIGN OF CRACKS [5].	7
FIGURE 1.3-2 SCHEMATIC AND COMPARISON BETWEEN A) CONVENTIONAL AL7075 PARTICLE FORMING ELONGATED DENDRITIC GRAIN STRUCTURES C), E), WHICH IS SUSCEPTIBLE TO CRACKS. B) Zr NANO PARTICLE ENHANCED AL7075 FORMS SMALL EQUIAXED GRAINS D), F), THAT ARE STRESS TOLERANT [6].	8
FIGURE 2-1 MAIN EFFECTS OF DMLS AND SLM. [9]	13
FIGURE 2-2 COLUMN DIAGRAM OF RA RESULTS FOR H=25 MM AND T=100 MS: A) TOP SURFACE; B) SIDE SURFACE. COLUMN DIAGRAM OF RA RESULTS FOR v=290 MM/S AND P=150 W: C) TOP SURFACE; D) SIDE SURFACE. E) BAR CHART OF SURFACE ROUGHNESS AND SLOPING ANGLE. [7]	15
FIGURE 2-3 MAIN EFFECT ON LENGTH (A), HEIGHT (B), AND WIDTH (C). [10]	17
FIGURE 2-4 EFFECT OF LASER POWER AND SCAN SPEED ON RELATIVE DENSITY OF 316L STAINLESS STEEL. [11]	19
FIGURE 2-5 SPECIMEN DESIGN [12]	20
FIGURE 2-6 RELATIVE DENSITY AS INFLUENCED BY A) SCANNING SPEED, AND B) LASER POWER. [12]	21
FIGURE 2-7 EFFECT OF SCANNING SPEED AND LASER POWER ON RELATIVE DENSITY [12]	21
FIGURE 2-8 EFFECT OF BUILD PLATFORM PREHEATING A) 40°C, AND B) 200°C RIGHT [12]	22
FIGURE 2-9 (A) OPTICAL MICROGRAPH OF THE XZ CROSS-SECTION FROM THE AS-BUILT LPBF ALZnMgScZr ALLOY. BACKSCATTER ELECTRON MICROGRAPHS OF THE XZ CROSS-SECTIONS FROM THE LPBF ALZnMgScZr ALLOY: (B) AND (C) AS-BUILT, (D) AND (E) AFTER T6 HEAT TREATMENT. [13]	23
FIGURE 2-10 ENGINEERING STRESS-STRAIN CURVES OF THE LPBF ALZnMgScZr ALLOYS IN THE AS-BUILT STATE AND AFTER T6 HEAT TREATMENT. [13]	25
FIGURE 2-11 MICROSTRUCTURE OF SAMPLE BUILD A) WITHOUT PREHEATING, AND B) WITH 2500C PREHEATING. [14]	26
FIGURE 2-12 MICROSTRUCTURE COMPARISON BETWEEN A) 240W LASER POWER, AND B) 960W LASER POWER. [14]	26
FIGURE 2-13 TENSILE STRENGTHS OF SPECIMENS BUILD WITH: A) POWER = 240W, SCAN SPEED = 500MM/S, B) POWER = 960W, SCAN SPEED > 1000MM/S, C) POWER = 960W, SCAN SPEED > 1000MM/S, PREHEATING OF 220°C [14]	27
FIGURE 2-14 TOP SURFACE MORPHOLOGY SIMULATION: A) POWER = 150 W, SCAN SPEED = 400MM/S, LEPUL = 375J/M, B) POWER = 150 W, SCAN SPEED = 300MM/S, LEPUL = 500J/M, C) POWER = 150 W, SCAN SPEED = 2000MM/S, LEPUL = 750J/M, D) POWER = 150 W, SCAN SPEED = 100MM/S, LEPUL = 1500J/M. [15]	28
FIGURE 2-15 VOLUME FRACTION CONTOURS OF THE CROSS-SECTIONS ALONG THE LASER SCAN DIRECTION UNDER VARIOUS LEPULS: A) POWER = 150 W, SCAN SPEED = 400MM/S, LEPUL = 375J/M, B) POWER = 150 W, SCAN SPEED = 300MM/S, LEPUL = 500J/M, C) POWER = 150 W, SCAN SPEED = 2000MM/S. [15]	29
FIGURE 2-16 SCHEMATIC OF RA MEASUREMENT [59]	31
FIGURE 2-17 SCHEMATIC OF Rt AND Rz EVALUATION [59]	32
FIGURE 2-18 THE TRUNCHEON TEST PART [17].	33
FIGURE 2-19 SURFACE PROFILE AT SURFACE INCLINE OF A) 5°, B) 10°, C) 65°. [17]	34
FIGURE 2-20 SCHEMATIC OF HEAT DIFFUSION DURING LASER MELTING PROCESS. [17]	34
FIGURE 2-21 THE SLICED PROFILE SCHEMATIC. [17]	35
FIGURE 2-22 MEASURED AND PREDICTED DISTANCE BETWEEN CONSECUTIVE STEP EDGES. [17]	35
FIGURE 2-23 PRESENCE OF PARTICLES ON HIGHLY SLOPED SURFACE. [17]	36
FIGURE 2-24 SEM PICTURE OF SLIGHTLY INCLINED SURFACE (SLOPING ANGLE 5°) (A) AT LOW MAGNIFICATION, (B) AT HIGH MAGNIFICATIONS, (C) DETAIL OF SLIGHTLY INCLINED SURFACE. [17]	36
FIGURE 2-25 REPRESENTATION IN 3D OF THE PROPOSED MODEL. [17]	37
FIGURE 2-26 SCHEMATIC REPRESENTATION: (A) LATERAL AND TOP VIEW OF A FRACTION OF PARTIALLY BONDED PARTICLES; (B) CROSS SECTION OF THE MODELLED SURFACE. [17]	37
FIGURE 2-27 COMPARISON BETWEEN MEASURED ROUGHNESS ON VALIDATION DATASET (SECOND SAMPLE) AND ROUGHNESS PREDICTED THROUGH NEWLY DEVELOPED MODEL. [17]	38

FIGURE 2-28 SCHEMATIC OF SURFACE ROUGHNESS MODEL. [20]	39
FIGURE 2-29 MEAN ABSOLUTE PERCENTAGE ERROR VALUES (%) FOR DIFFERENT ANALYTICAL MODELS. [20].....	41
FIGURE 2-30 THE TRUNCHEON TEST PART. [20].....	41
FIGURE 2-31 COMPARISON OF A) MEASURED RA ON THE TEST PART AND: B) CAMPBELL MODEL, C) MASON MODEL, D) AHN MODEL, E) PANDEY MODEL, AND F) BYUN MODEL. [20]	42
FIGURE 3-1 THE CUBIC SAMPLES.	55
FIGURE 3-2 SCHEMATIC OF SAMPLE PLACEMENT ON THE BUILD PLATE. THE CUBIC SAMPLE OCCUPIES THE ENTER OF THE BUILD PLATE, WHILE TENSILE COUPONS WERE PLACE TOWARDS THE EDGE OF THE BUILD PLATE.	56
FIGURE 4-1 SEM IMAGES OF POWDER MORPHOLOGY: (A,B) AL6061, (C,D) ALSi10MG.....	65
FIGURE 4-2 PARTICLE SIZE DISTRIBUTION OF THE AL6061 AND ALSi10MG POWDERS.	66
FIGURE 4-3 XRD PHASE PATTERNS OF THE AL6061 AND ALSi10MG POWDERS.....	67
FIGURE 4-4 MICROSTRUCTURE OF THE AS-BUILT ALSi10MG_200C SAMPLES PROCESSED UNDER DIFFERENT SLM PROCESS PARAMETERS; A, C) AS8, B) AS7, D, F) AS3, E, G, H) AS1.....	69
FIGURE 4-5 THE SEM OBSERVATIONS OF THE AS-BUILT ALSi10MG MICROSTRUCTURE ALONG Z- DIRECTION; A) AS8, B) AS3, C) AS1 NEAR TOP SURFACE, D) AS1 NEAR THE CENTER.	71
FIGURE 4-6 SEM OBSERVATION OF ALSi10MG MICROSTRUCTURE ALONG XY PLANE; A) AS8, B) AS3, AND C) AS1.....	72
FIGURE 4-7 XRD PHASE PATTERN MEASURED ON THE TOP SURFACE (ALONG THE XY PLANE) OF DIFFERENT AS-BUILT ALSi10MG SAMPLES.	73
FIGURE 4-8 XRD PHASE PATTERN MEASURED ON THE SIDE SURFACE (ALONG THE Z-DIRECTION) OF DIFFERENT AS-BUILT ALSi10MG SAMPLES.	73
FIGURE 4-9 MICROSTRUCTURE OF THE AS-BUILT AL6061 SAMPLES PROCESSED UNDER DIFFERENT SLM PROCESS PARAMETERS; A,C,E) 6A ALONG THE Z-DIRECTION , B,D,F) 6A ALONG THE XY PLANE, G) 14A, H) 15A.....	75
FIGURE 4-10 MICROSTRUCTURE GRAINS OF THE AS-BUILT AL6061 SAMPLE AT A HIGHER MAGNIFICATION.	76
FIGURE 4-11 XRD PHASE PATTERN MEASURED ON THE SIDE SURFACE (ALONG THE Z-DIRECTION) OF DIFFERENT AS-BUILT AL6061 SAMPLES.	77
FIGURE 4-12 XRD PHASE PATTERN MEASURED ON THE TOP SURFACE (ALONG THE XY PLANE) OF DIFFERENT AS-BUILT ALSi10MG SAMPLES.	77
FIGURE 4-13 EFFECT OF THE SLM PROCESS PARAMETERS ON MICROHARDNESS OF THE AS-BUILT ALSi10MG SAMPLES ALONG THE Z-DIRECTION.....	79
FIGURE 4-14 EFFECT OF THE SLM PROCESS PARAMETERS ON MICROHARDNESS OF THE AS-BUILT ALSi10MG SAMPLES ALONG THE XY PLANE.....	80
FIGURE 4-15 EFFECT OF THE SLM PROCESS PARAMETERS ON MICROHARDNESS OF THE AS-BUILT AL6061 SAMPLES ALONG THE BUILDING DIRECTION.....	81
FIGURE 4-16 EFFECT OF THE SLM PROCESS PARAMETERS ON MICROHARDNESS OF THE AS-BUILT AL6061 SAMPLES ALONG THE XY PLANE.	82
FIGURE 4-17 EFFECT OF THE SLM PROCESS PARAMETERS ON ULTIMATE TENSILE STRENGTH OF THE AS-BUILT ALSi10MG SAMPLES ALONG THE BUILDING DIRECTION.....	84
FIGURE 4-18 EFFECT OF THE SLM PROCESS PARAMETERS ON YIELD STRENGTH OF THE AS-BUILT ALSi10MG SAMPLES.	85
FIGURE 4-19 EFFECT OF THE SLM PROCESS PARAMETERS ON ULTIMATE TENSILE STRENGTH OF THE AS-BUILT AL6061 SAMPLES ALONG THE BUILDING DIRECTION.	86
FIGURE 4-20 EFFECT OF THE SLM PROCESS PARAMETERS ON YIELD STRENGTH OF THE AS-BUILT AL6061 SAMPLES.	87
FIGURE 4-21 PORES OBSERVED INSIDE THE AS-BUILT ALSi10MG SAMPLE FABRICATED AT DIFFERENT SLM PARAMETERS; A, D) AS8, B, E) AS3, C) AS1.	88
FIGURE 4-22 INFLUENCE OF THE SLM PROCESS PARAMETERS ON RELATIVE DENSITY OF THE AS-BUILT ALSi10MG SAMPLES.	89
FIGURE 4-23 PORES OBSERVED INSIDE THE AS-BUILT AL6061 SAMPLES PROCESSED THROUGH DIFFERENT SLM PARAMETERS; A, D) 8A, B, E) 4A, C) 1A.....	90
FIGURE 4-24 THE SLM PROCESS PARAMETERS EFFECT ON RELATIVE DENSITY OF THE AS-BUILT AL6061 SAMPLES.	91
FIGURE 4-25 THE SEM OBSERVATIONS ON THE AS-BUILT SURFACE OF ALSi10MG SAMPLES; A) AS8, B) AS3, C) AS1.	92
FIGURE 4-26 THE 3D SURFACE TEXTURE OF THE AS-BUILT ALSi10MG SAMPLES; A) AS8, B) AS6, C) AS3, D) AS1.....	93
FIGURE 4-27 EFFECT OF THE SLM PROCESS PARAMETERS ON SURFACE ROUGHNESS OF THE AS-BUILT ALSi10MG SAMPLES.	94
FIGURE 4-28 THE SEM OBSERVATIONS ON THE AS-BUILT SURFACE OF AL6061 SAMPLES; A, D) 7A, B, E) 14A, C, F) 1A.....	95
FIGURE 4-29 THE 3D SURFACE TEXTURE OF THE AS-BUILT AL6061 SAMPLES; A) 8A, B) 6A, C) 14A, D) 11A.	96
FIGURE 4-30 EFFECT OF THE SLM PROCESS PARAMETERS ON SURFACE ROUGHNESS OF THE AS-BUILT AL6061 SAMPLES.	97

FIGURE 4-31 EFFECT OF THE SLM PROCESS PARAMETERS ON DIMENSION TOLERANCE OF THE AS-BUILT ALSi10MG SAMPLES.	98
FIGURE 4-32 EFFECT OF THE SLM PROCESS PARAMETERS ON SURFACE FLATNESS OF THE AS-BUILT ALSi10MG SAMPLES.....	99
FIGURE 4-33 EFFECT OF THE SLM PROCESS PARAMETERS ON DIMENSION TOLERANCE OF THE AS-BUILT AL6061 SAMPLES.	100
FIGURE 4-34 EFFECT OF THE SLM PROCESS PARAMETERS ON SURFACE FLATNESS OF THE AS-BUILT AL6061 SAMPLES.....	101
FIGURE 4.5-1 THE OPTIMAL PROCESSING WINDOW GENERATED FOR ALSi10MG AT THE HATCH SPACING VALUE OF 0.19 MM.	104
FIGURE 4.5-2 THE OPTIMAL PROCESSING WINDOW GENERATED FOR AL6061 AT THE HATCH SPACING VALUE OF 0.15 MM.	105

List of tables

TABLE 2-1 PROCESS PARAMETERS FOR Ti-6Al-4V. [7]	14
TABLE 2-2 PROCESS PARAMETER VARIABLES FOR CL50WS TOOL STEEL. [10]	16
TABLE 2-3 CONTROLLED PROCESS PARAMETERS FOR CL50WS TOOL STEEL. [10]	16
TABLE 2-4 PROCESS PARAMETERS FOR AW7075. [12]	20
TABLE 2-5 COMPOSITION OF CHARGE ALLOYS (ALZNMgSrZr), LPBF ALLOY [13], AND AL7050.....	22
TABLE 2-6 PROCESS PARAMETERS FOR ALZNMgSrZr. [13]	23
TABLE 2-7. ROOM TEMPERATURE TENSILE PROPERTIES WITH STANDARD DEVIATIONS IN PARENTHESIS OF THE LPBF ALZNMgScZr ALLOYS IN THE AS-BUILT STATE AND AFTER T6 HEAT TREATMENT. [13].....	24
TABLE 2-8 PROCESS PARAMETERS FOR AlSi10Mg. [14].....	25
TABLE 2-9 PROCESS PARAMETERS FOR 316L STAINLESS STEEL. [17]	34
TABLE 3-1 THE SIX POSSIBLE COMBINATIONS OF POWER, HATCH SPACING, AND SCAN SPEED.	49
TABLE 3-2 ALL POSSIBLE 2^3 FULL FACTORIAL DOE REPRESENTED AT CODE.	49
TABLE 3-3 FULL SET OF 216 DIFFERENT 2^3 FULL FACTORIAL DESIGN.....	50
TABLE 3-4 THE STANDARD DEVIATION, MINIMUM, MAXIMUM, AND RANGE OF THE CALCULATED ENERGIES FOR EACH OF 216 POSSIBLE FULL FACTORIAL DESIGN.	51
TABLE 3-5 POTENTIAL FULL FACTORIAL DESIGNS THAT ARE SUITED BASED ON THE FITNESS REQUIREMENTS.	52
TABLE 3-6 THE SLM PROCESS PARAMETERS APPLIED FOR PRODUCING THE AlSi10Mg_200C SAMPLES.....	57
TABLE 3-7 THE SLM PROCESS PARAMETERS USED FOR BUILDING THE Al6061_200C SAMPLES.....	57
TABLE 4-1 EDS ANALYSIS OF THE Al6061 AND AlSi10Mg POWDERS CHEMICAL COMPOSITION.	66
TABLE 4-2 THE VALUES MEASURED FOR THE PARTICLE SIZE DISTRIBUTION OF THE Al6061 AND AlSi10Mg POWDERS.....	67

List of abbreviations and symbols

AM – Additive Manufacturing

RP – Rapid Prototyping

CNC – Computer Numerical Control

SL – Stereolithography

UV – Ultraviolet

FDM – Fused Deposition Modelling

SGC – Solid Ground Curing

LOM – Laminated Object Manufacturing

SLS – Selective Laser Sintering

DSPC – Direct Shell Production Casting

LAM – Laser Additive Manufacturing

SLM – Selective Laser Melting

EBM – Electron Beam Melting

DED – Direct Energy Deposition

OFAT – One-Factor-At-a-Time

CMM – Coordinate-Measuring Machine

DOE – Design of Experiment

ANOVA – Analysis of Variance

DMLS – Direct Metal Laser Sintering

LEPUL – Laser Energy per Unit Length

Ra – Arithmetic mean roughness

CTE – Coefficient of Thermal Expansion

SD – Standard Deviation

GD&T – Geometric Dimensions and Tolerance

RSM – Response Surface Method

Declaration of Academic Achievement

The main contribution of this thesis is the development of optimal processing window of selective laser melting process for Al6061 and AlSi10Mg, that ensures the satisfaction of quality for part density, surface roughness, and dimensional accuracy. The relationship between laser power, scan speed, hatch spacing, energy density on the part quality was studied as individual effects as well as interactive effects.

1. Introduction

1.1. Overview of Additive Manufacturing

With the high level of attention, interest, and investment in Additive Manufacturing (AM), a technology that was originally used in rapid prototyping (RP), is experiencing a rapid growth [1]. Before going into the details of the research in AM, it is worthwhile to understand the history of AM, which provides information on the conception of this technology as well as the industrial sectors that gave this technology such priority, and thereby the motivation behind most of today's research in AM.

Despite the technical name of AM, AM is neither new nor a revolutionary manufacturing technology. On the most basic level, to build things additively, materials are added together to fabricate the product. For millennia, this had been the technology which man had used to build structures big and small. The novelty of AM, as know today, was not from the method/mode which the product was produced, but rather the ability to translate digital designs into physical parts layer by layer using computer numerical controlled (CNC) machines. This reduces the need for product-specific tools used during manufacturing, thus making it a general method for manufacturing. Compound that with the ability of fast free-form fabrication, AM became the popular in the early days as a method for RP [2].

The first commercial use of AM as known today was in the form of stereolithography (SL) in 1987 by 3D Systems. SL uses ultraviolet (UV) laser to cure and solidify thin layers of liquid UV sensitive polymers. In these early days of AM, technologies developed mostly revolved around polymers as they were stable under wide range of conditions and less prone to oxidations. Until

1992, four more AM technology had been invented, fused deposition modeling (FDM) from Stratasys, solid ground curing (SGC) from Cubital, laminated object manufacturing (LOM) from Helisys, and Selective laser sintering (SLS) from DTM. However, it wasn't until 1993 with the introduction of direct shell production casting (DSPC) from Soligen, that material other than polymers were used in AM. In 1997 with the release of laser additive manufacturing (LAM) by MTS Systems Corp, where powdered titanium alloys were melted by high power laser aimed for the aerospace industries, sparked the development for metal AM. Until current times, three main forms of metal AM exist (Powder bed system, Powder Feed system, and Wire feed system), two of which uses powdered metal as the feed stock that trades high build rate to high precision and geometry complexity [3].

With more interest and research generated around AM, ASTM Committee 42 on Additive Manufacturing was formed in 2009, that standardised the AM technologies which at the time were largely proprietary depending on the commercial AM companies. These standardizations are on the testing, processes, materials, design (including file formats), and terminology. Due the early conception of polymer AM technologies, along with polymer feed stocks' stable nature in most forms, the polymer AM sector had in most matured, with research and development currently are aimed at cost reduction and optimization. Metal AM however are not as developed. Although, as mention above, AM for metal had existed commercially since 1997, due to the volatile and unstable nature of common alloys used in most industries, metal AM research in the fundamentals of the process parameters, and design of alloys are still in great need [3].

1.2. Selective Laser Melting

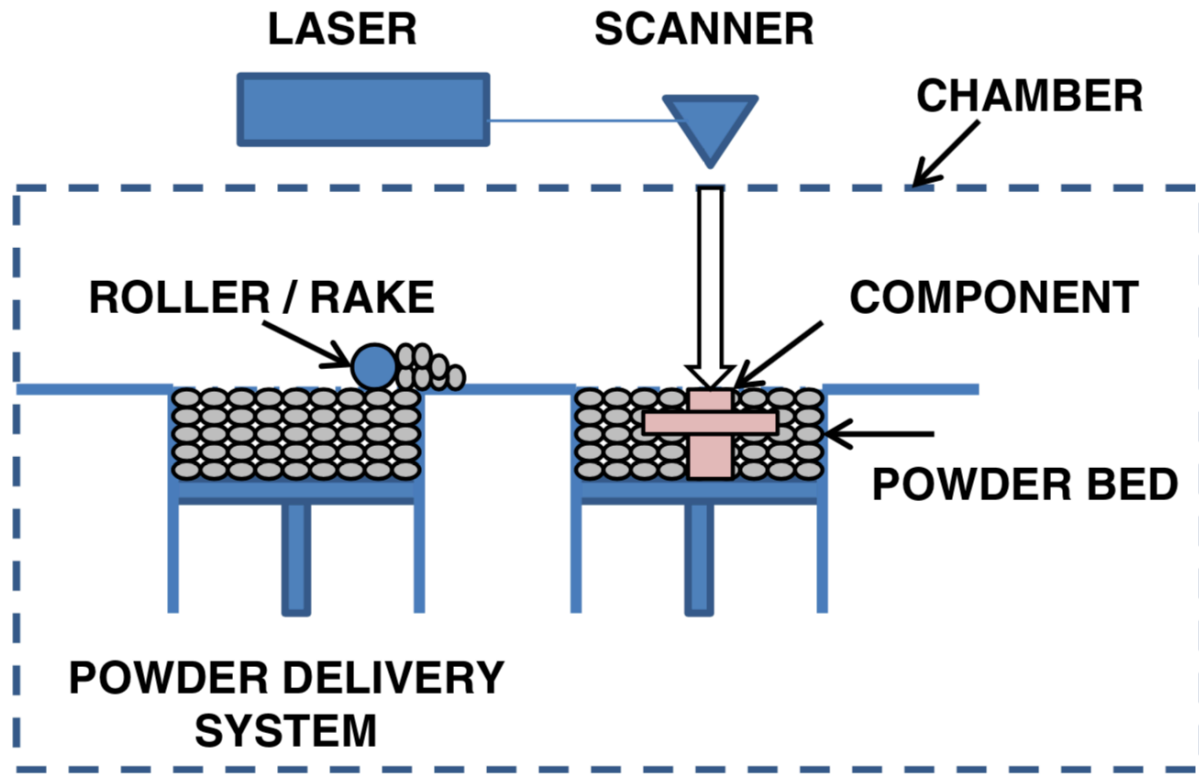


Figure 1.1-1 Schematic of selective laser melting process [16].

Majority of research interests for metal AM are focused on the Selective Laser Melting (SLM) process, as this technology is widely known to be superior in dimension accuracy and surface quality, as well as deposition rate compare to Electron Beam Melting (EBM), Direct Energy Deposition (DED), and Fuse Deposition Melting (FDM). Figure 1.1-1 showcases the schematic of SLM build process. During SLM process, high power laser beam moves to melt and consolidate thin layer of metal powder under inert atmosphere. After the completion of each layer, the build platform is lowered, and a new thin layer is then spread on top of the previous layer, this layer by layer process is repeated to build the three-dimensional component. This technique is used from 3D prototyping to small scale productions. With the growing industry adoption of SLM, it is not without challenges.

As seen in Figure 1.2-3, materials go through complex thermal cycles due to the laser melting and re-melting from the layer to layer process, forming unconventional microstructures, Figure 1.2-3. thus, it was identified that a linkage between the understanding of microstructures, the process parameters, and the material properties of SLM fabricated parts is needed for the production of robust and high-quality products.

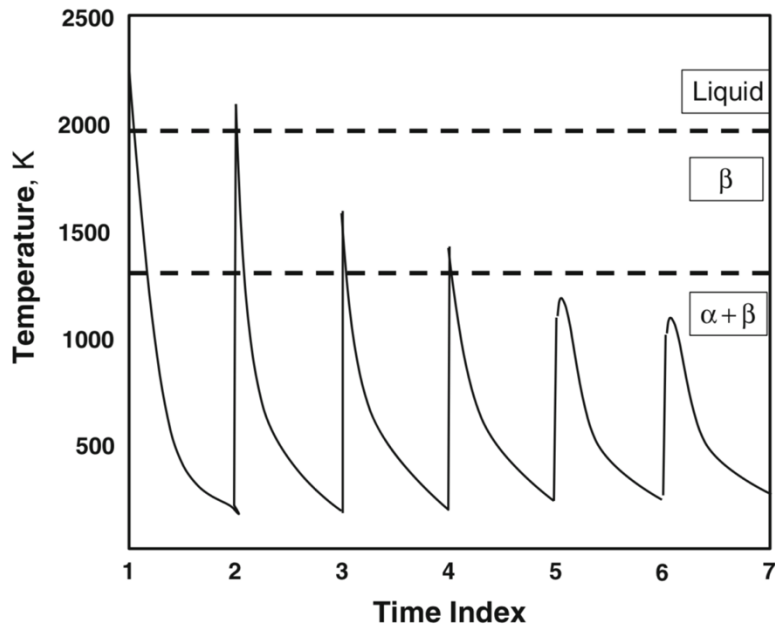


Figure 1.2-3 Temperature profile during the layer-by-layer process of SLM [16].



Figure 1.2-3 The complex microstructure of Ti-6Al-4V resulting from rapid melting and cooling from the SLM process [16].

1.3. Challenges and current solutions

Due to the similar nature of material consolidation of welding and, to an extent, casting, SLM process is currently limited to materials that are capable to undergo melting and solidification rapidly. Currently alloys that are identified to be suitable for SLM is very limited comparing to that of the traditional styles of manufacturing [4]. This list is even smaller selection of aluminum alloys available for SLM. Al alloys are in great demand in the transportation industry due to its lightweight and high strength nature along with relative low cost of raw material. The challenge with Al alloys when comes to SLM is the formations of porosities and voids, which leads to cracking, thus ultimately compromises the mechanical properties. Voids and porosities are present in other alloys when produced with unoptimized process conditions using SLM, which can be fixed by adjusting the energy input of the laser to compensate for over melting or for under melting. However, for high strength Al alloys, due to the solidification nature of alloys that have composition far from eutectic, the solid fraction growth rate during solidification far out reaches comparing to the temperature decrease. This results in the growth of large dendrites during solidification with entrapped gaps between the dendrites too small for liquid metal to flow and to fill, thus forming micron-level pores. Compounding the effect of solid shrinkage from solidification with the pores acting as nucleation sites, cracking forms, which in this case is also known as hot tearing.

1.3.1. Alloy content change

In the industry this problem is solved by using high silicon alloyed aluminum (Al), AlSi10Mg, which is close to A380 casting Al alloy, and relatively robust to SLM. However, its mechanical property is inferior to that of more common used engineered high strength alloy, Al6061, which are used more commonly in the aerospace and automotive industry. Due to the high alloying content, AlSi10Mg solidifies with fine grains, which is desirable to prevent shearing from thermal stress, but it was undesirable for the alloy to experience multiple re-melting and re-solidifications of SLM resulting the formation of silicon particle precipitations from solute diffusion. The silicon particle precipitations reduce the post process machinability due to the high hardness, which also reduces the alloy's tensile strength.

1.3.2. Alloy mixing

To increase the relative density of the low alloying aluminum, Al6061 and Al7075, grain refinement method had been explored in literature. Such technique takes the advantage of solidification nature of liquids, which is to seek lower energy level by forming less surface area [5] [6]. Al6061 and Al7075 by themselves have very low affinity to form small grains, but with introduction of grain refiners in the form of inert nano particles acting as nucleation sites, small equiaxed grains can be formed, which is strain-tolerant, thus elimination of hot tearing [6].

Montero-Sistiaga et al. [5], experimented with Al7075. By increasing the silicon content of the alloy with the introduction of AlSi10Mg, they were able to achieve near crack-free product, Figure 1.3-1.

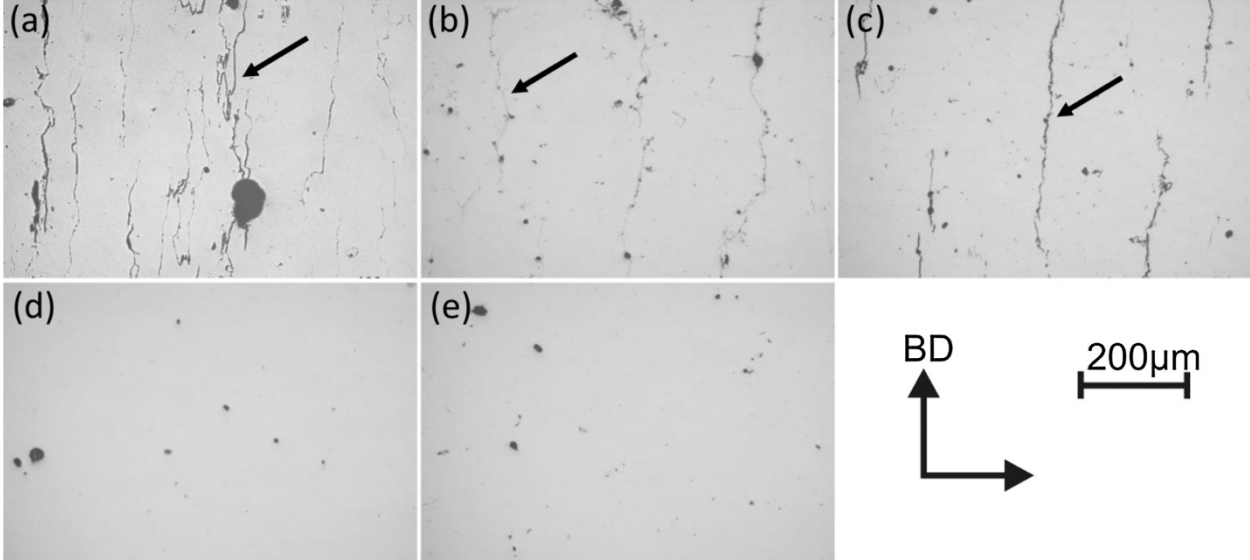


Figure 1.3-1 Micrograph of polished samples. Addition of 0%wt a), 1%wt b), and 2%wt c) of AlSi10Mg powder displayed hot tearing. 3%wt d), and 4%wt e) of AlSi10Mg addition showed no sign of cracks [5].

Martin et al. [6] experimented with the additive of zirconium nano particles to Al6061 and Al7075 with the aim to achieve Al_3Zr nucleant phase, which forms equiaxed grains that is robust to thermal stress, Figure 1.3-2.

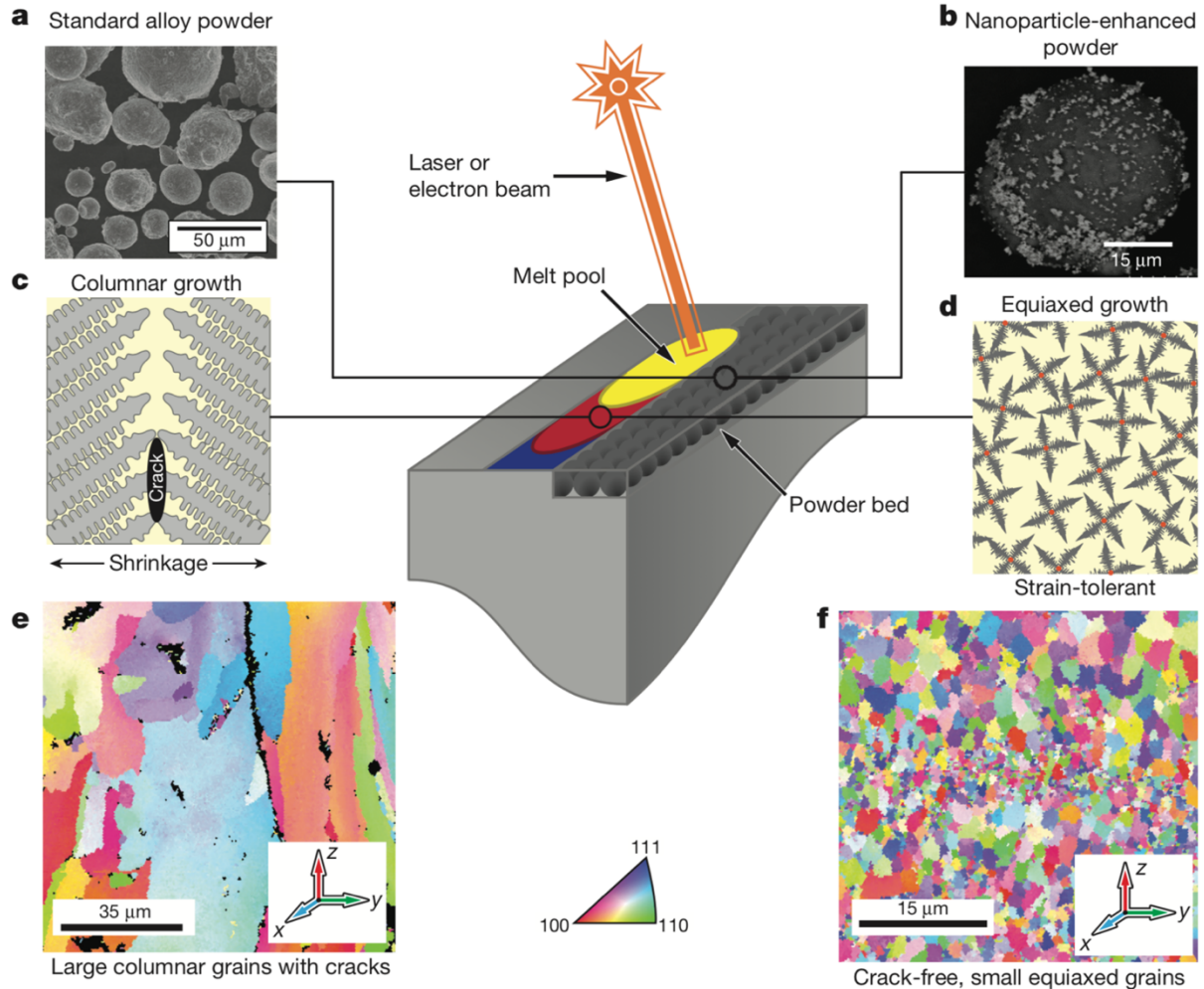


Figure 1.3-2 Schematic and comparison between a) conventional Al7075 particle forming elongated dendritic grain structures c), e), which is susceptible to cracks. b) Zr nano particle enhanced Al7075 forms small equiaxed grains d), f), that are stress tolerant [6].

Such technique can produce very high-quality parts from Al6061 and Al7075, however at the expense of mixing the precious metal nano-particles, which is costly both in raw material as well as the mixing process. More research and study are still needed for specialty alloy designs, and their commercialization for cost reduction. In the meantime, basic process parameters still need to be studied and explored. Parameters in the laser system of SLM machines forms complex interaction with each other, which is very challenging to analyse and to simulate, thus statistical analysis with carefully designed experiments is currently the most suitable method to explore such topic.

1.4. Current work

This work details the process of experiment design to test and analyse sample of Al6061 and AlSi10Mg produced via SLM.

Chapter 2 looks into the current works found in literature on the topics of process parameter studies for SLM, as well as surface roughness models presented by various teams of researchers for both SLM and FDM technologies. Chapter 2 aids in the selection of SLM process parameters for the experimental work in Chapter 3, the details of the experimental design were laid out. Chapter 3 also contains the experimental procedures of quality evaluation, which includes: powder characterization, microstructure examination, microhardness testing, tensile strength testing, density measurement, dimensional accuracy measurement, and surface roughness measurement. The results of the quality evaluations are discussed in Chapter 4, where regression models that describes the relations between laser process parameters and the produced parts' surface quality, dimensional accuracy, and relative density were formulated. Combining the results, a process map was formulated for producing parts with good quality using Al6061 and AlSi10Mg produced via SLM. Chapter 5 concludes the current work, and suggestion for potential future work is provided.

2. Literature review

2.1. Introduction

The state-of-the-art of industrial additive manufacturing (AM) can be broken into three main components: 1. Process parameter influence, 2. Surface roughness, and 3. Topology optimization. These components can be applied to the AM process of selective laser melting (SLM), which is most suitable form for AM of metals.

These three components can be seen as hierarchical in nature, as products produced by the additive manufacturing technique has to first satisfy the material mechanical property requirements, which in essence means lack of internal defects. This is important due to the fact that most post process treatment to the produced parts are superficial, thus proper understanding and control of the SLM machines' process parameters is crucial in order to build a solid foundation for the rest of optimization efforts.

Surface roughness optimization can be pursued when mechanical properties satisfied, and internal defects eliminated. Surface roughness can be considered as the least important components of the three as post process surface treatments are relatively less costly as comparing to typical heat treatment for enhancing mechanical properties, or densification treatments to heal small cracks. However, it is still important to pursuit methods on improving surface roughness for SLM part out of machine as any form of unnecessary post processing adds to the cost of the production [7]. Good surface quality on SLM produced parts can also indicate and enhance its mechanical properties, as the process is layer-by-layer, therefore rough, defective surface layer during the building process can adversely affect the successive layers.

Finally, one of the most promising advantage of the AM technique is the ability to produce parts with high complexity in geometry which are very challenging, and sometime impossible, using tradition manufacturing techniques. It opens the opportunity for topology optimization techniques to be applied, where the design of the parts is defined as physical constrains such as constraint on area and constraint on mechanical loads. The constraints are then used to calculate the optimal shape for the part, which often resembles natural organic growth. Such designs optimize the strength to weight ratio and is only feasible to be produced by AM.

2.2. Process parameters

Process parameters for SLM directly influence the produced part's quality. With the large number of variables that can possibly affect the outcome of the print, finding out and understanding each of their influence on the outcome is very resource intensive.

However, with to the Pareto principle, few out of all the variables contributes to most of the effects [8]. This principle was seen in literature on the topics of SLM as majorities of researchers had experimented with the same process parameters.

Some literature also experimented with the Volumetric energy density(J/mm^3), however since it is the product of the base variables: laser power, laser scanning speed, laser hatch spacing, and layer thickness, studying the base variables will provide more details on the relations between the SLM machine and the characteristics of the parts produced.

In the work done by Delgado et al. [9], build direction, layer thickness, and scan speed, were investigated on the surface roughness and mechanical properties for the iron-based CL 20 (equivalent to 316L). Through full factorial design of experiment (DOE) and analysis of variation (ANOVA), building direction (varied from 0 degree to 90 degrees relative to build platform) was found to have significant influence on the surface roughness. Vertical surface was observed to be rougher than horizontal surface, while the opposite effect was observed for dimensional accuracy. As seen in Figure 2-1, both scan speed and layer thickness had no significant effect on the surface roughness, but did display significant effect for the mechanical properties, which included: tensile strength, elongation, bending strength, and hardness [9].

Although exact relationship between the experimented process parameters cannot be formed due to the lack of variability of the factors' levels (two levels variability in this case), as well as the lack of analysis on the interaction effect between factors, the word did valuable identification on the main effects for surface roughness, dimensional accuracy, and mechanical properties.

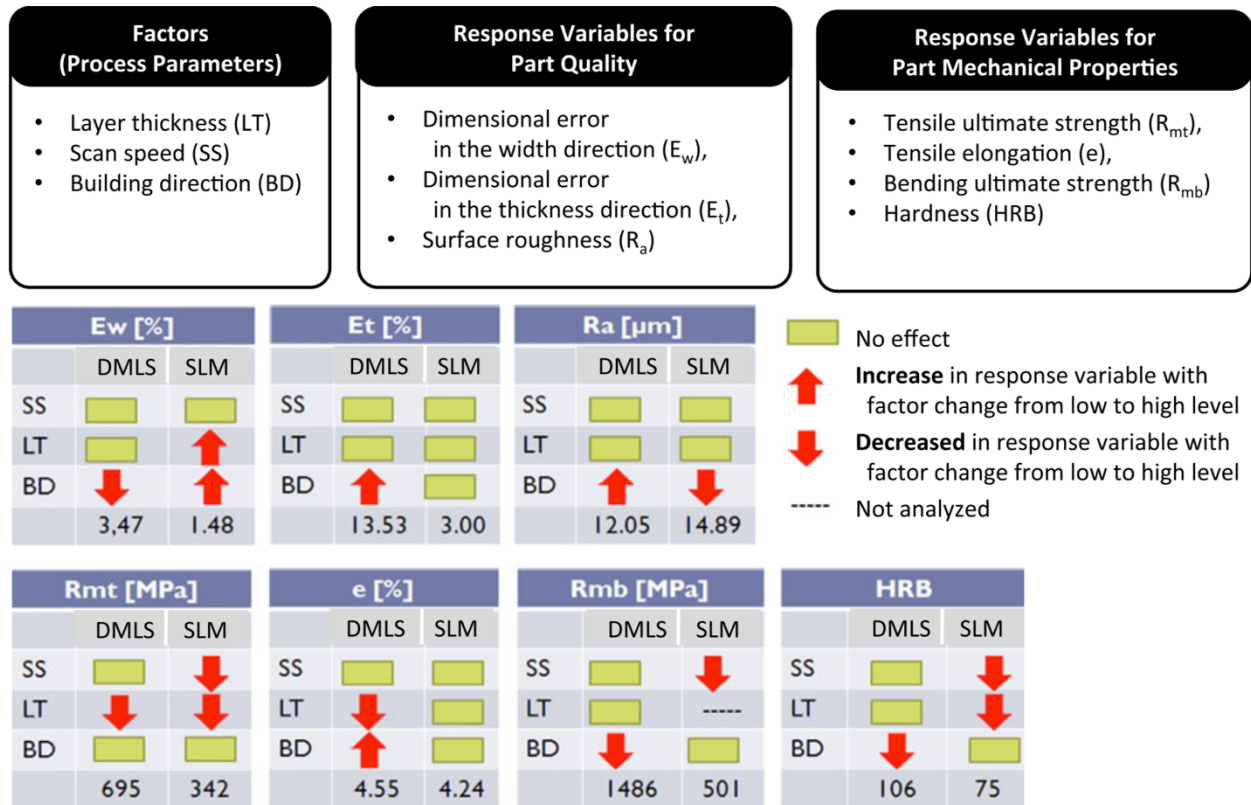


Figure 2-1 Main effects of DMLS and SLM. [9]

Experiments on the effect of SLM parameters on surface roughness of Ti-6Al-4V alloy conducted by Krol and Tanski [7], had studied four parameters listed in Table 2-1.

Parameter	First set, value	Second set, value
Laser Power (W)	75, 100, 125, 150	150
Scanning speed (mm/s)	200, 230, 260, 290	290
Hatch spacing (μm)	25	25, 50, 75, 100
Exposure time (μs)	100	25, 50, 75, 100

Table 2-1 Process parameters for Ti-6Al-4V. [7]

Full factorial DOE was conducted, varying two factors over four levels over the span of two sets of experiments. The aim for the study was mainly to find the set of parameters where top surface roughness is minimized, and they are found out to be:

- Laser power: 150W,
- Scan speed: 290mm/s,
- Exposure time: 25 μs ,
- Hatch spacing: 25 μm .

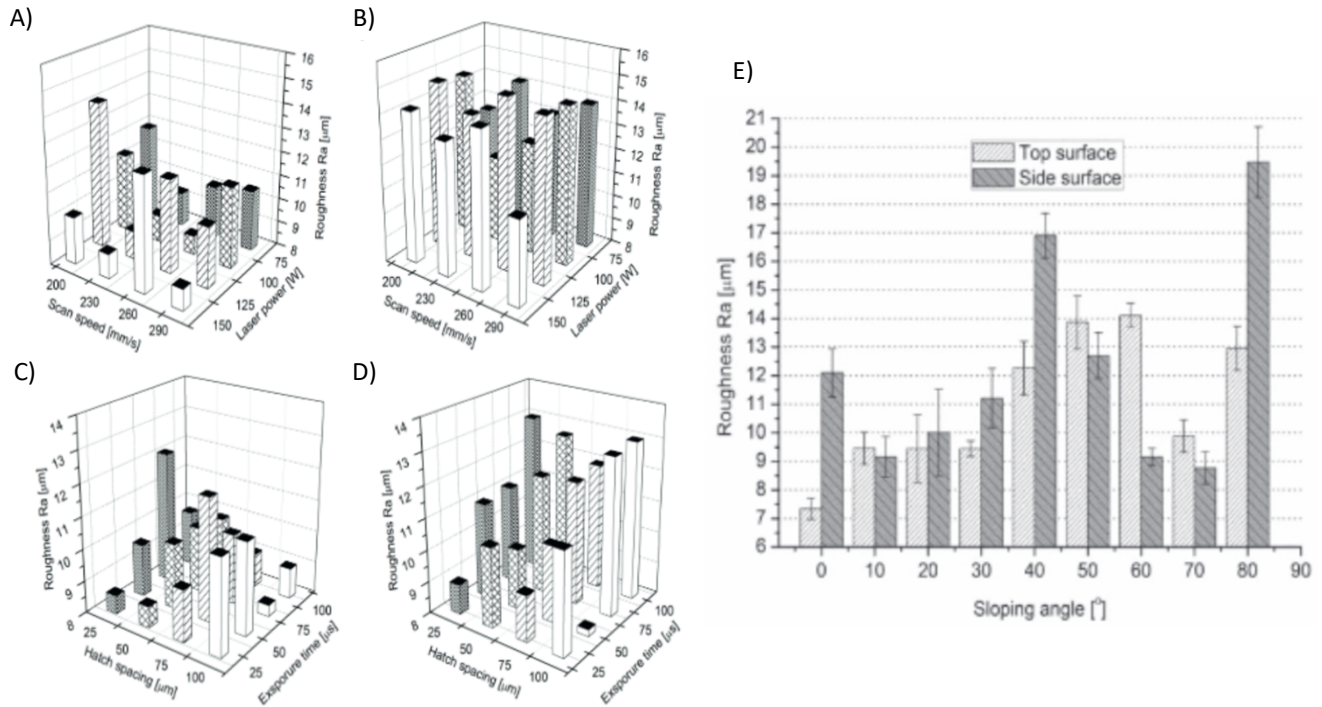


Figure 2-2 Column diagram of Ra results for $h=25\ \mu\text{m}$ and $t=100\ \mu\text{s}$: a) top surface; b) side surface. Column diagram of Ra results for $v=290\ \text{mm/s}$ and $P=150\ \text{W}$: c) top surface; d) side surface. e) Bar chart of surface roughness and sloping angle. [7]

Finally, a one-factor-at-a-time (OFAT) experiment on studying the effect of angle of tilt relative to the build platform was conducted, where 10-20 degrees of tilt results in the optimal surface roughness on both the top and side surface of cubic geometries [7].

Since the study used higher degree of variation per factors, thus higher resolution of relation between factor and surface roughness was observed, which are non-linear as seen in Figure 2-2 a-d. The study concludes that the poor surface roughness on the vertical surfaces are due to powder particles adhering to the side surface, which itself is caused by the balling-effect due to insufficient melting. This is also evident from the surface roughness measurement in Figure 2-2 e. Balling-effect is due to low energy input to the substrate, where one of the main contributors is lack of power, which explained the reason the researchers found that the highest power yielded the best results. However, with solid foundation of DOE, the research

lacks the analysis on the interaction effects between factors, which could explain and relate in more detail, the mechanisms of the formations of defects such as the balling-effect.

On the topic of dimensional accuracy, Gajera and Dave [10] had use the Tauguchi method DOE to study the effect of build orientation and layer thickness on CL50WS tool steel provided by Concept laser[10].

The prismatic samples are printed with variable parameters listed in Table 2-2, and controlled parameters in Table 2-3. Height, width, and length being measured by coordinate-measuring machine (CMM). The researchers varied build orientation using 0 degrees and 90 degrees relative to the build platform, and layer thickness varied from 0.03mm to 0.06mm with 0.01mm increment.

Process parameter	Level 1	Level 2	Level 3	Level 4
Build orientation [degree]	0	90		
Layer thickness [mm]	0.03	0.04	0.05	0.06

Table 2-2 Process parameter variables for CL50WS tool steel. [10]

Parameter	Value
Powder material	CL50
Scan speed	600mm/s
Laser power	120 W
Hatch spacing	0.7 * d

Table 2-3 Controlled process parameters for CL50WS tool steel. [10]

Analysis of variance (ANOVA) was conducted for dimensional measurements of each of the three dimensions, where its statistical significance was confirmed. Through this, it was found that the width variance had no statistically significant relation with either of the varied process parameters. Thermal related effects are significant to the parts dimensional accuracy, as expansion/contraction and curling are commonly caused by uneven temperature

distribution, which is characteristic of direct metal laser sintering (DMLS). Therefore, the observation of the width variance was explained by the uneven temperature distribution, that are dimension (size) and build orientation dependent.

From the observation, it was concluded that layer thickness is the dominant parameter for dimensional accuracy and surface roughness, as seen in Figure 2-3. This is because the reduced temperature difference between each of the melted layers reduces cooling rate, thus reducing shrinkage.

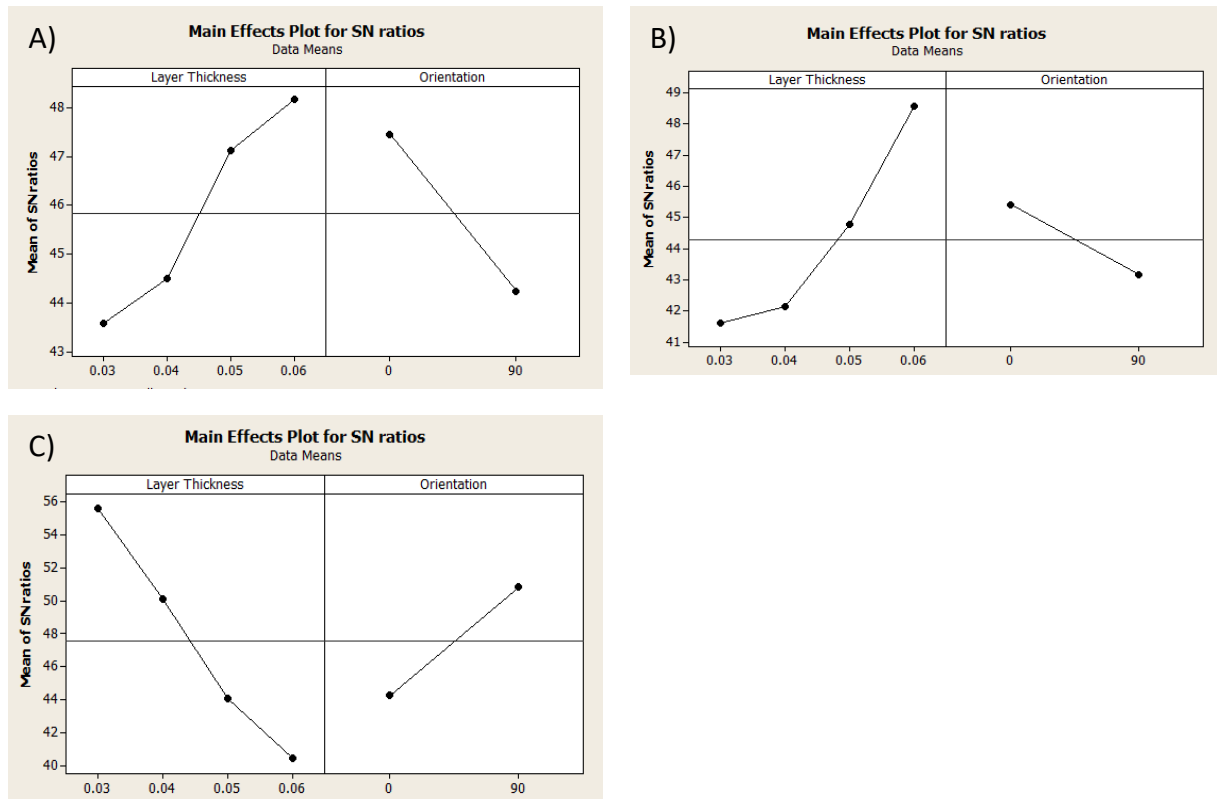


Figure 2-3 Main effect on Length (A), Height (B), and Width (C). [10]

Valuable work on 316L stainless steel was done by Kamath et al. [11], where first, data from prior works were analysed, and simulation conducted. DOE conducted from that knowledge revealed optimal settings for maximum relative density.

Compilation of process parameters and relative density from others' work on 316L stainless steel showed that reducing layer thickness increases relative density, where 30 μ m was the optimal thickness [11]. The work then used Eagar-Tsai simulations to determine the dominant process parameters out of: laser power, scan speed, spot size, and absorptivity, found from the previous works. Using data mining, the simulation ranked the process parameters on its relevancy to the output, in this case melt pool geometry. The work focused on the melt pool geometry because sufficient melt pool depth directly relates to high density parts. Melt pool width and depth was found to be affected most by scan speed and laser power and melt pool length is affected by laser power and absorptivity. Finally, based on the results from a single-track bead experiment, with parameters chosen from the simulation, a DOE with factors being laser power and scan speed was conducted to study the effect on parts' relative density.

From Figure 2-4, the work concludes that the cause of low density/increase of porosity is mainly caused by insufficient melting due to low power and high scan speed, as well as over melting caused by low scan speed. However, operating at high power showed a wider range of scan speed that are robust to porosity formation.

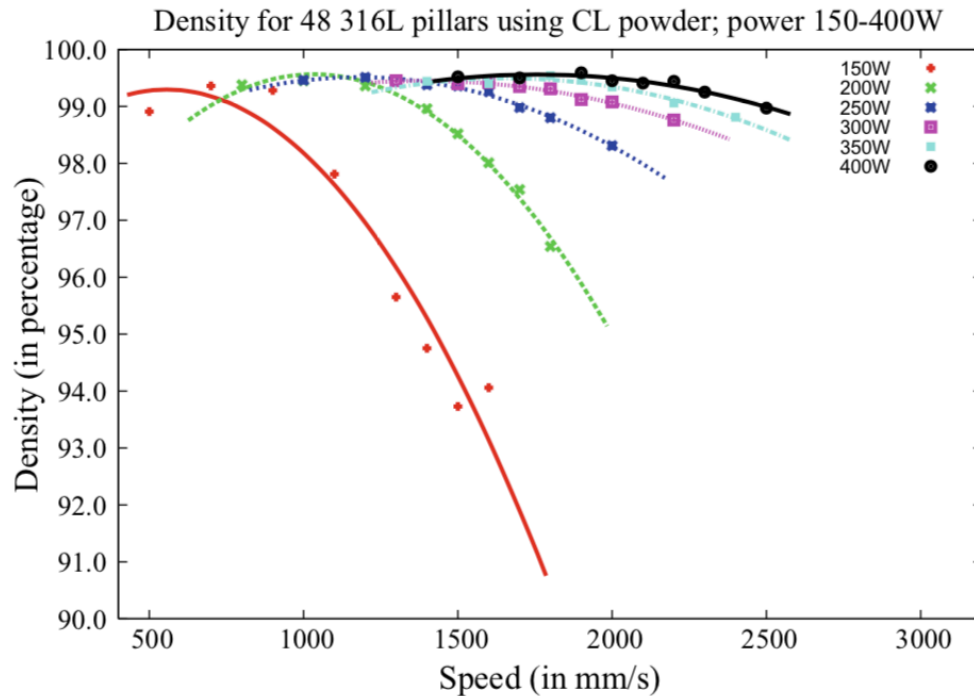


Figure 2-4 Effect of laser power and scan speed on relative density of 316L stainless steel. [11]

Aluminum alloys are known for being relatively cost-effective material with high strength to weight ratio. However, when it comes to SLM, high strength aluminum alloys are known to hot crack, a phenomenon commonly found in manufacturing processes that involves rapid solidification such as casting and welding. Microscale cracks that might evolve into bigger cracks, were formed during solidification due to the dendritic formation, the change in viscosity of the cooling liquid metal, and the change in density of the cooling metal from liquid to solid. Dendrites form gaps between each other during solidification that were not filled by the remaining liquid due to its viscosity, thus the remaining gap becomes cracks.

In 2016, Kaufmann et al. [12] attempted to optimise the SLM process parameter on the aluminum ally EN AW 7075, a common aerospace high strength aluminum alloy that is known for hot cracking. An OFAT experiment was used, to understand the relation between laser power and scan speed, as well as the effect of preheating the build platform on the density and crack formation of the parts.

Process parameters	Values
Laser Power (W)	100, 150, 200, 300, 400, 500, 600
Scanning speed (mm/s)	250, 500, 600, 700, 800, 900, 1000, 1100, 1200, 1300, 1400, 1500, 1600, 1700, 1800, 1900, 2000
Hatch spacing (mm)	0.13
Layer thickness (μm)	50
Preheating temperature ($^{\circ}\text{C}$)	40, 200

Table 2-4 process parameters for AW7075. [12]

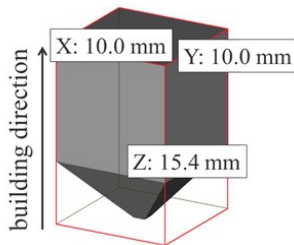


Figure 2-5 specimen design [12]

The cubic samples (Figure 2-5) were produced with the process parameter listed in Table 2-4. Using optical microscope, images were taken on the cut and polished samples, where filters were applied to distinguish pores, thus relative density of the parts were calculated based on porous area. From this a map was compiled (Figure 2-7) where the effect of power and scanning speed on the porosity formation can be observed. High power seems to reduce porosity regardless of the speed. This is also seen in the graphs below. This prompted the suggestion of using high power (500W), as seen in the curve in Figure 2-6 a and b, when producing parts single high scanning speed can then be used. This increases the build rate to

13.0mm³/s, which increases productivity. However, the trade-off for this increase in build rate

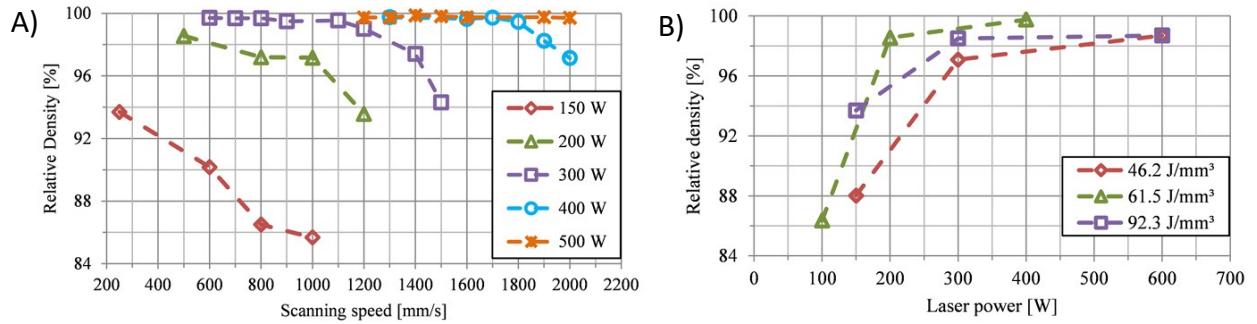


Figure 2-7 relative density as influenced by a) scanning speed, and b) laser power. [12]

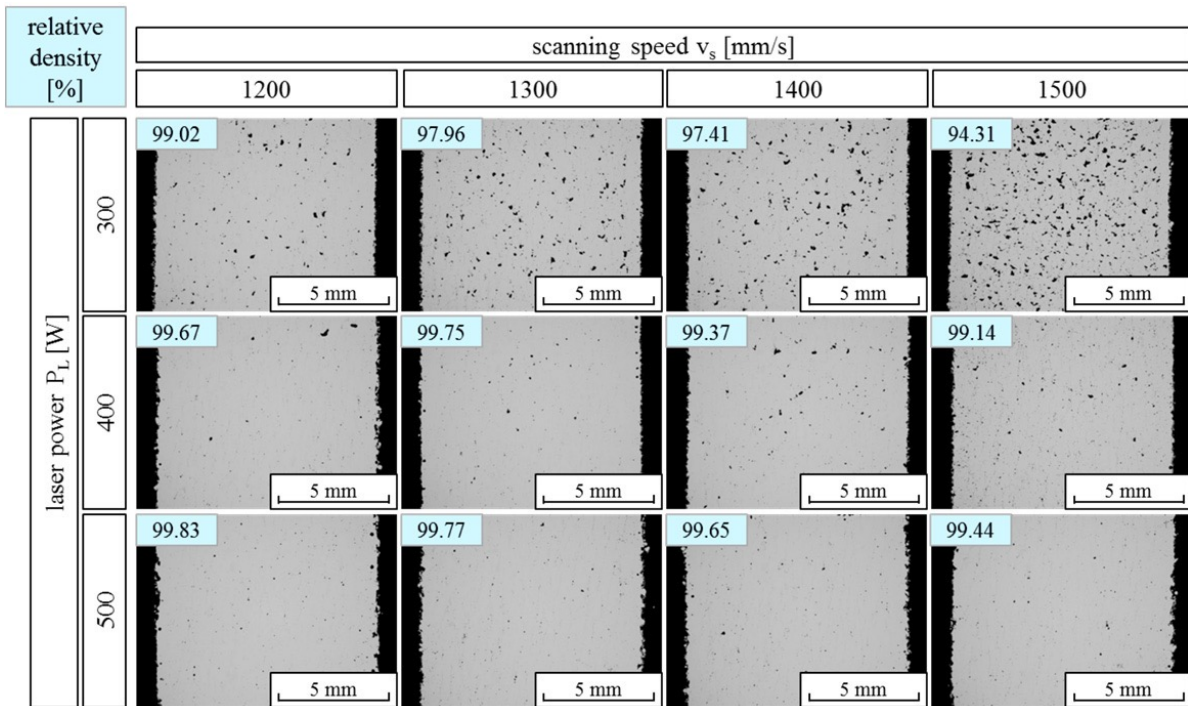


Figure 2-6 Effect of scanning speed and laser power on relative density [12]

is the change of chemical composition, as the element zinc was observed to reduce by 1.6 wt.% due to its low evaporation temperature.

Since one major contributor to hot cracking is large thermal gradient, preheating the build platform to reduce the gradient would reduce crack severity. However, comparison between 40 °C and 200 °C preheating, as seen in Figure 2-8, showed no significant difference in

the crack formation and severity. Thus, it was concluded that 200 °C preheating was not hot enough to reduce the thermal gradient.

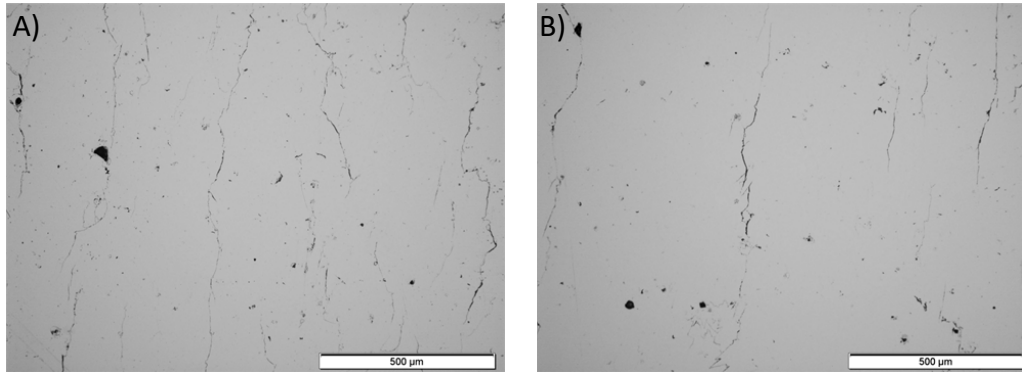


Figure 2-8 Effect of build platform preheating a) 40°C, and b) 200°C right [12]

Recent work on aluminum alloy by Zhou et al. [13] used scandium and zirconium particles addition to the Al-6Zn-2Mg feed stock to produce crack-free parts. The research aims to solve the problem of crack formation of conventional high strength Al alloys such as 2xxx, 6xxx, and 7xxx. The Al-6Zn-2Mg was used as a substitute for the Al7050 alloy commonly used in the aerospace industry, with the Sr particles replacing the Copper particles. The chemical composition of the alloys is listed in Table 2-5.

Wt.%	Al	Zn	Mg	Sr	Cu	Zr
AlZnMgSrZr (nominal) [13]	Bal.	5.96	2.03	0.68	-	0.28
LPBF alloy (experiment) [13]	Bal.	6.04	1.87	0.81	-	0.23
Al7050	Bal.	6.2	2.3	-	2.3	0.1

Table 2-5 Composition of charge alloys (AlZnMgSrZr), LPBF alloy [13], and Al7050.

The work focused on the efficacy on the grain refinement particles, and the mechanical properties of the parts produced. Using the one process parameter listed in Table 2-6, cubic samples of 12mm x 12mm x 12mm along with six 25mm gauge length tensile coupons (ASTM E8/E8M) were produced.

Power(W)	Layer thickness(mm)	Hatch spacing(mm)	Scan speed(mm/s)
350	0.03	0.13	900

Table 2-6 Process parameters for AlZnMgSrZr. [13]

The result showed the presence of very small amount of porosity (<0.4% volume fraction), with no cracks in the cubic samples. In Figure 2-9, duplex microstructures were observed with columnar grains of $50\mu\text{m}$ in length towards the center of the melt pool, and equiaxed grains of $0.2\mu\text{m} - 2\mu\text{m}$ size grown along the border of the melt pool as observed in Figure 2-9 (c, e)

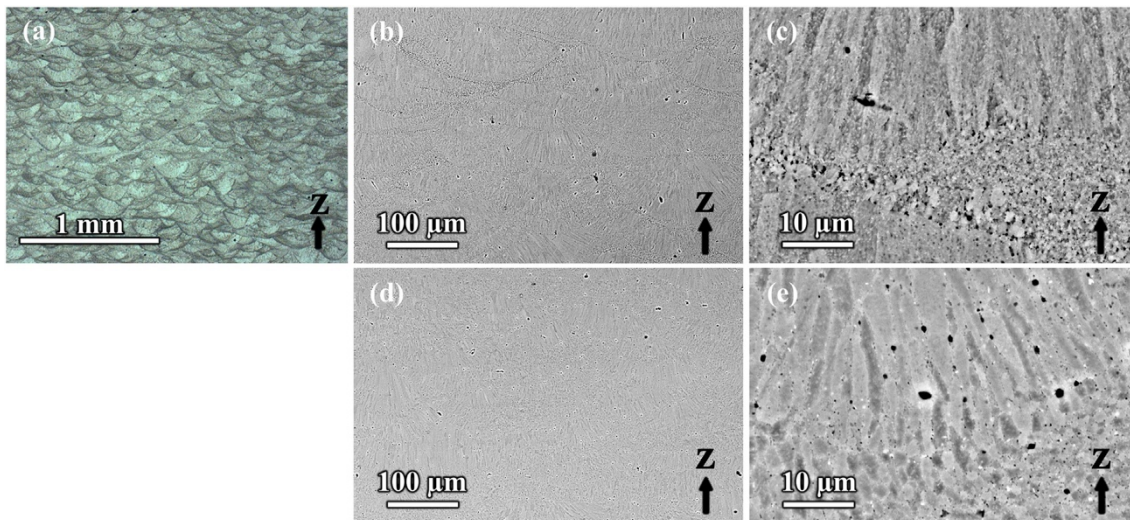


Figure 2-9 (a) Optical micrograph of the XZ cross-section from the as-built LPBF AlZnMgScZr alloy. Backscatter electron micrographs of the XZ cross-sections from the LPBF AlZnMgScZr alloy: (b) and (c) as-built, (d) and (e) after T6 heat treatment. [13]

The formation of the equiaxed grains were facilitated by the formation of $\text{Al}_3(\text{Sr}, \text{Zr})$ particles during solidification, which provides low energy barrier for the heterogeneous nucleation. The equiaxed grains formed along the melt pool boundaries obstruct the growth of long columnar grains typically found in unmodified 6xxx, and 7xxx alloys, which extends across multiple melt pool layers. The reason for the columnar grains still present is because the $\text{Al}_3(\text{Sr}, \text{Zr})$ particles decay and dissolve back into solution at temperature above 800°C , which is the case in at the center of the melt pool. Due to rapid solidification and cooling, the formation of

supersaturated solid solution suppresses the formation of Al₃(Sr, Zr) in the center of the melt pool.

Stress and strain of the as-build samples along with samples that had gone through T6 heat treatment are summarized in Table 2-7. Although inferior to the wrought AA7050 alloy, the yield and ultimate tensile strength post T6 was around 85% of the wrought alloy as seen in Figure 2-10, which is acceptable for certain applications that can make the trade-off between high complexity of design by sacrificing some mechanical strength. Furthermore, optimizing process parameter could have significant improvements on the mechanical properties.

	$\sigma_{0.2}$ (MPa)	UTS (MPa)	EL (%)	E (GPa)
As-build	283.5 (1.5)	386/0 (1.1)	18.4 (0.1)	69.9 (1.7)
T6	418.3 (2.7)	435.7 (2.5)	11.1 (0.9)	65.4 (1.2)
AA7050	496	524	11	71.7
Wrought				

Table 2-7. Room temperature tensile properties with standard deviations in parenthesis of the LPBF AlZnMgScZr alloys in the as-built state and after T6 heat treatment. [13]

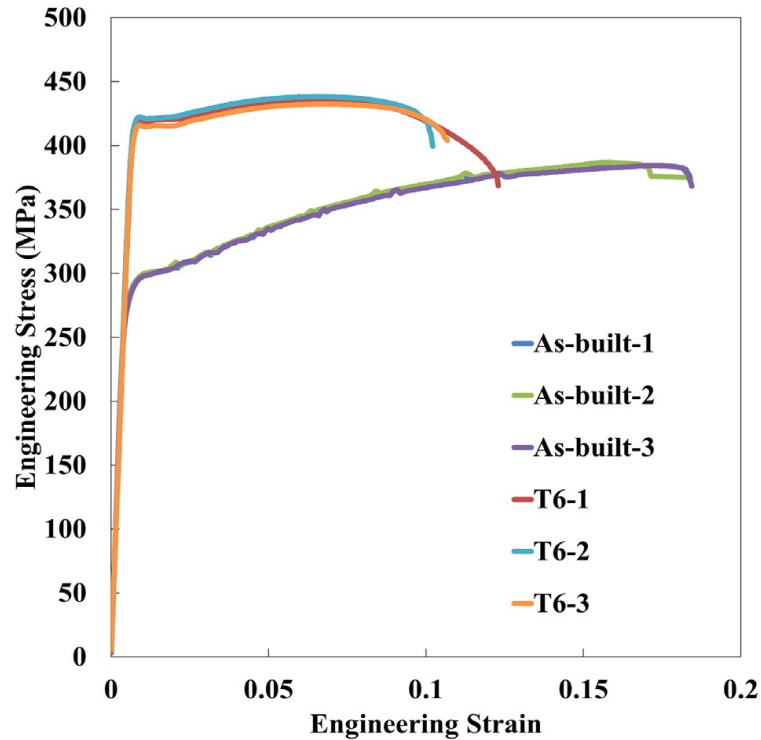


Figure 2-10 Engineering stress-strain curves of the LPBF AlZnMgScZr alloys in the as-built state and after T6 heat treatment. [13]

The AlSi10Mg alloy commonly used in SLM process, due to its good castability, was studied by Buchbinder et al. [14]. Correlation between SLM process parameters and the mechanical properties were drawn, in which it was found that high power laser (960W) coupled with high scan speed (1000mm/s) produces approximately the same mechanical properties as low power (240W) and low speed (500mm/s) setting, suggesting that energy density (J/mm^3) can be a good starting point in predicting the mechanical properties of the final part.

Process parameters	Values
Laser Power (W)	240, 900
Scanning speed (mm/s)	500, 1000
Build-up orientation ($^{\circ}$)	0, 90
Preheating temperature ($^{\circ}C$)	None, 250

Table 2-8 Process parameters for AlSi10Mg. [14]

10mm x 10mm x 10mm cubic samples were built with the process parameters listed in Table 2-8 to test the influence on the laser parameters, the build directions, and the preheating conditions. No significant porosity was observed, and a relative density of over 99% was achieved. Significant difference in microstructure was observed between samples with and without preheating.

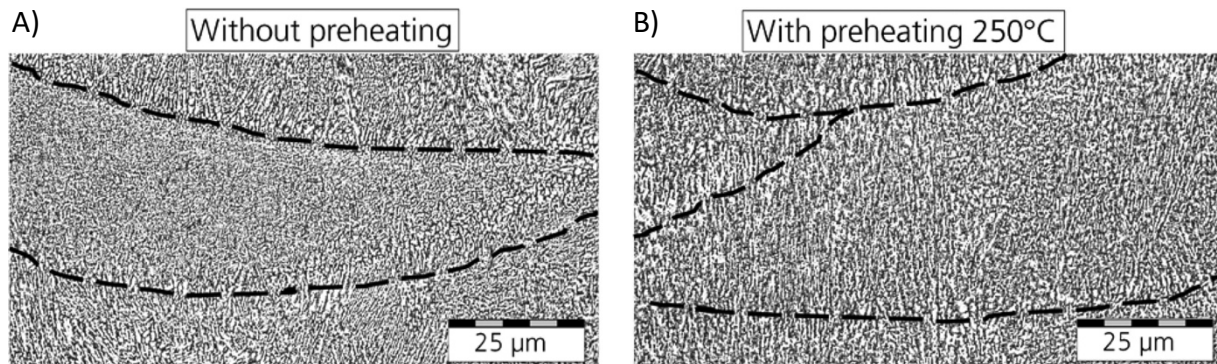


Figure 2-11 Microstructure of sample build a) without preheating, and b) with 250°C preheating. [14]

As seen in Figure 2-11, preheating coarsens the microstructure (grains and dendrites), thus decreasing the hardness from 130 Hv to 84 Hv. This is due to the slower cooling rate; however, it is still above the hardness of the AlSi10Mg alloy produced through casting, which is 75 Hv, due to a much slower cooling rate. The microstructure coarsening was also observed with low scanning speed as observed in Figure 2-12. The cooling rate effect on the mechanical

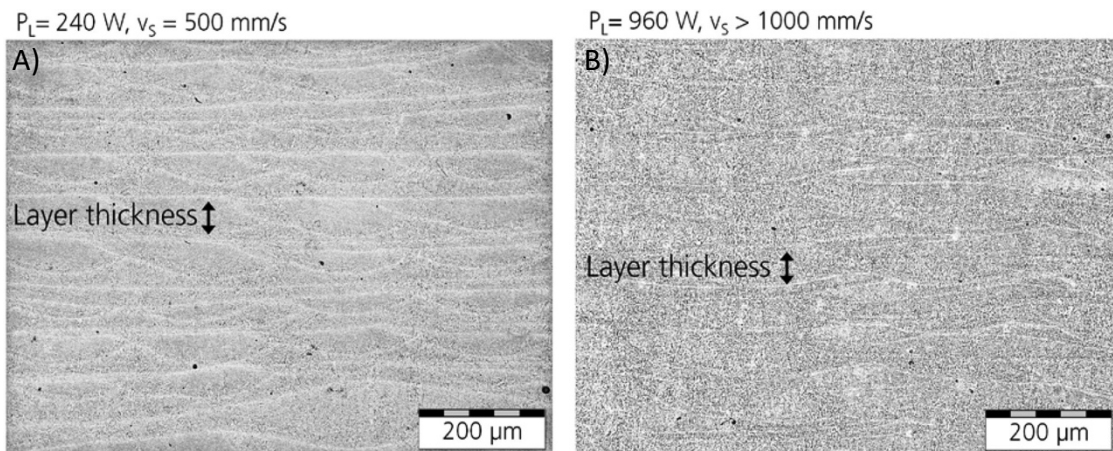


Figure 2-12 Microstructure comparison between a) 240W laser power, and b) 960W laser power. [14]

property was also observed in Figure 2-13, where the fast cooling rate with the combination of laser power and scan speed in Figure 2-13 a) and b), trumps the ultimate tensile and yield strength when comparing to that seen in Figure 2-13 c), which again is due to the grain coarsening effect.

Finally, slight anisotropy in mechanical property was observed in Figure 2-13. Changing the build direction from 0° to 90° decreases the breaking elongation due to the presence of the brittle silicium-rich phases in the grain and melt pool boundary.

This coupled with the low aspect ratio between the melt pool height and width, causes the break elongation to be reduced when load is applied perpendicular to the build direction.

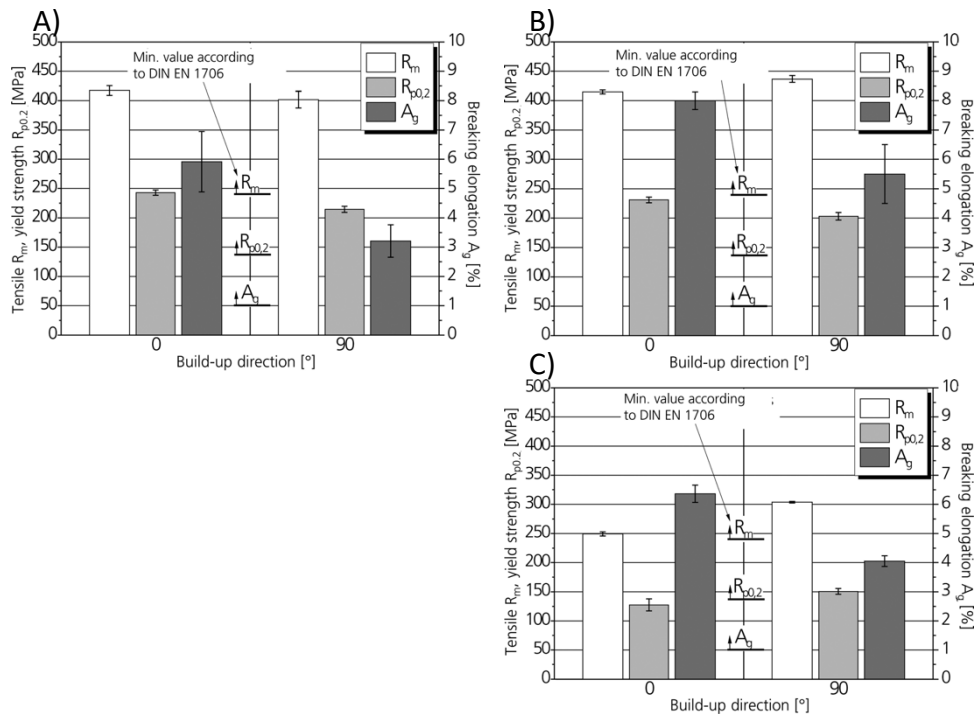


Figure 2-13 Tensile strengths of specimens built with: a) power = 240W, scan speed = 500mm/s, b) power = 960W, scan speed > 1000mm/s, c) power = 960W, scan speed > 1000mm/s, preheating of 220°C [14]

To further understand the mechanisms of the SLM process, as well as to attempt at making predictions on the final properties of a SLM produced part, numerical analysis on TiC/AlSi10Mg was carried out by Dai and Gu [15].

The work simulates the fluid flow caused by surface tension and recoil pressure happening during the laser melting process, which was governed fundamentally by the conservation of mass, momentum, and energy.

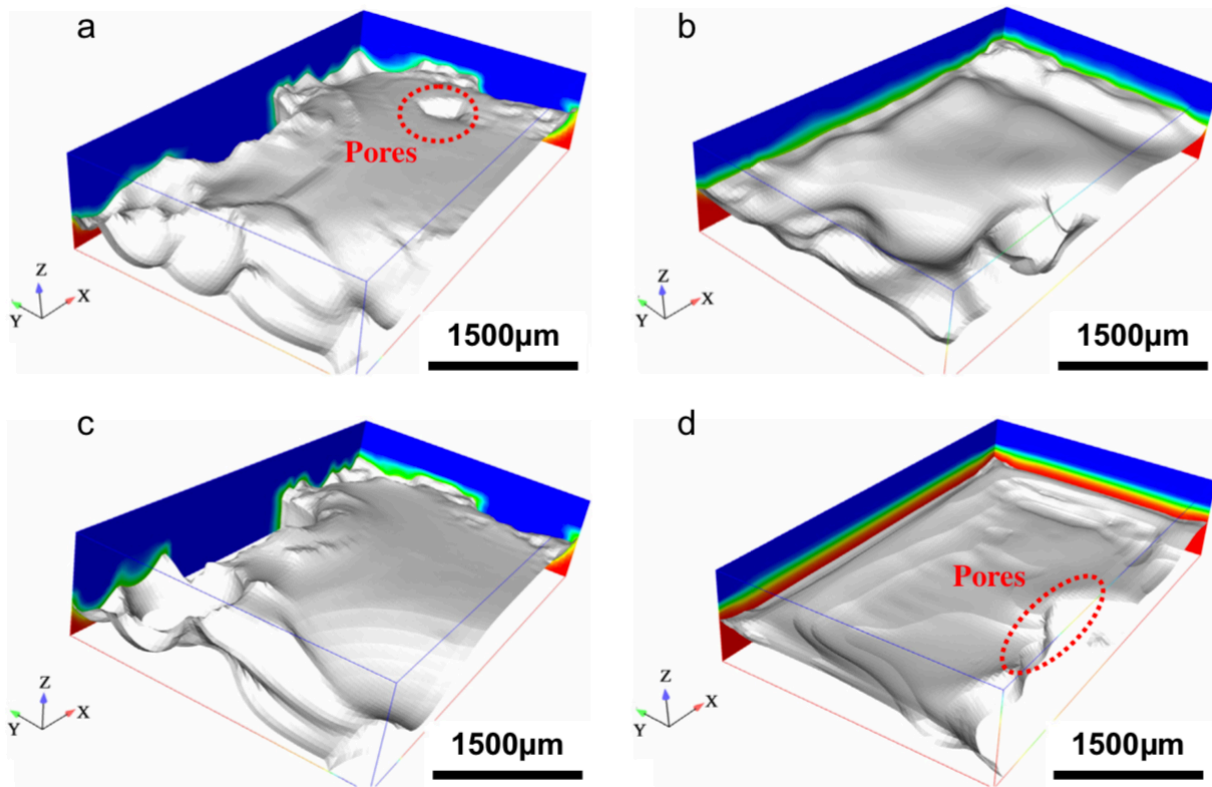


Figure 2-14 top surface morphology simulation: a) power = 150 W, scan speed = 400mm/s, LEPUL = 375J/m, b) power = 150 W, scan speed = 300mm/s, LEPUL = 500J/m, c) power = 150 W, scan speed = 2000mm/s, LEPUL = 750J/m, d) power = 150 W, scan speed = 100mm/s, LEPUL = 1500J/m. [15]

Finally, top surface quality was obtained through simulation by the analysis and simulation of temperature gradient and melt pool dynamics.

Through analysis of surface tension and melt pool dimension using simulation with governing equations, top surface morphology was simulated at different laser energy per unit lengths (LEPULs) (Figure 2-14).

The mechanisms behind the poor surface roughness was due to the high viscosity of the melt, which cannot be overcome by the surface tension difference to spread the melt evenly.

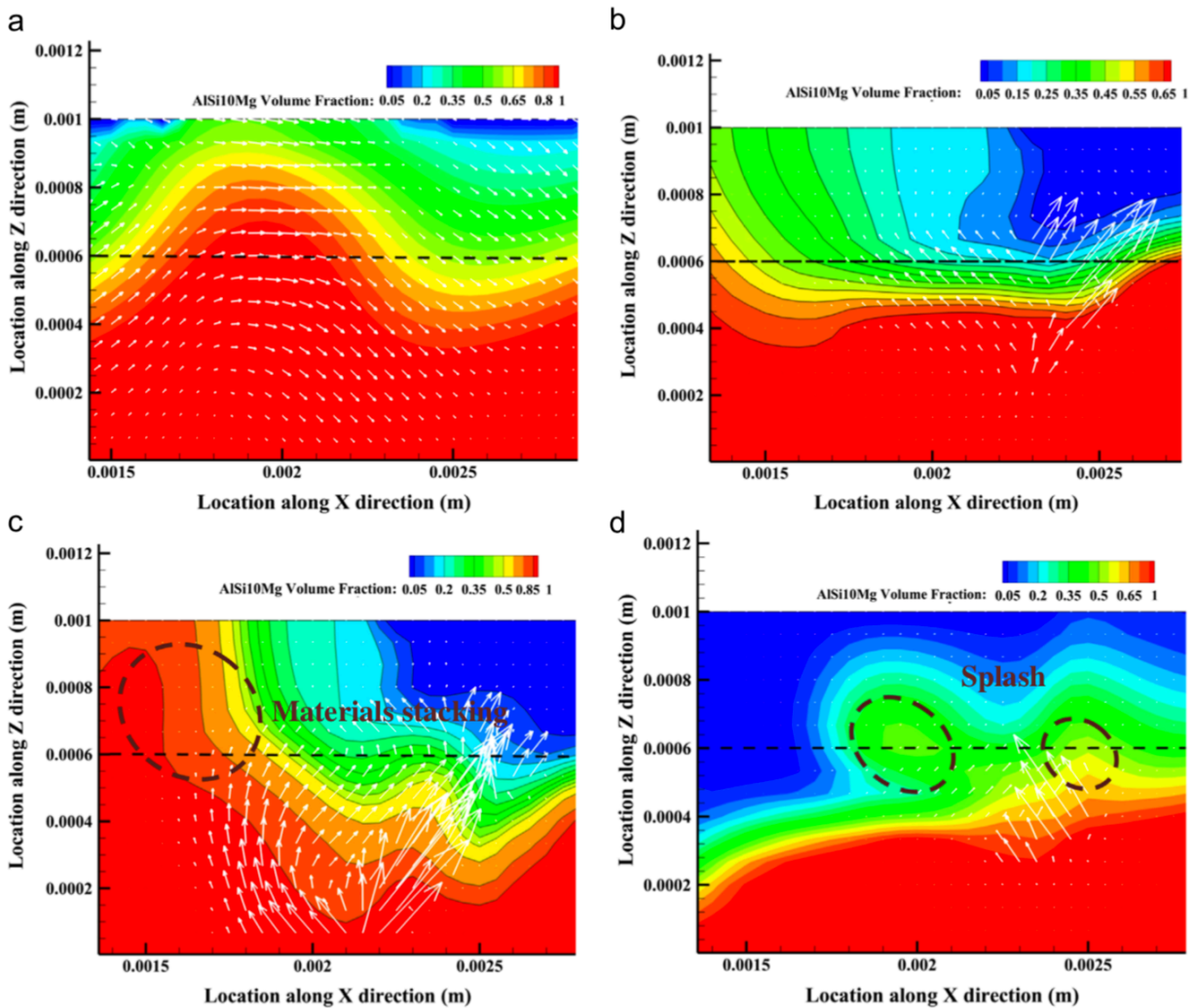


Figure 2-15 Volume fraction contours of the cross-sections along the laser scan direction under various LEPULs: a) power = 150 W, scan speed = 400mm/s, LEPUL = 375J/m, b) power = 150 W, scan speed = 300mm/s, LEPUL = 500J/m, c) power = 150 W, scan speed = 2000mm/s. [15]

As seen in Figure 2-15, at higher LEPUL, 500J/m in this case, the viscosity of the melt becomes low enough for the surface tension to spread evenly but increasing more to 750J/mm reduced the viscosity too much, where high surface tension near the rear of the melt pool pulls material from center to the rear, results in stacking, and ultimately rough surface. Much higher LEPUL of 1500J/m results in material vaporization, limiting the spread of melt due to reduction in volume, thereby resulting in an unstable melt pool.

2.3. Surface Roughness

The importance of surface roughness is beyond cosmetic as it has direct correlation with the products' fatigue life [16] (Eq. 1), therefore it is of high importance to understand, predict, and to control the surface roughness for AM processes.

$$\ln(\text{fatigue life}) = -0.34 \ln(\text{surface roughness}) + \text{constant}. \quad [1]$$

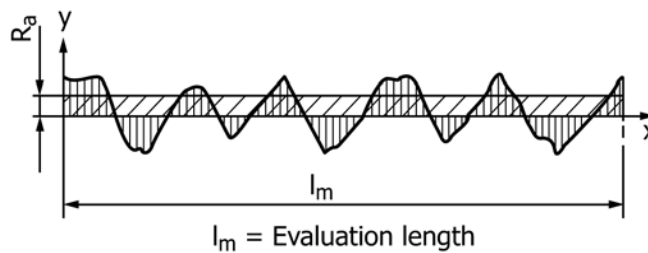


Figure 2-16 Schematic of R_a measurement [59]

According to ASTM B946-11 (2016), the three commonly used surface finish parameters are R_a (Eq. 2), R_t (Figure 2-17), and R_z (Figure 2-17). R_a is the most accepted parameter when reporting surface roughness as it is defined as the arithmetic mean of the peaks and valleys on an evaluated surface (Figure 2-16).

$$R_a = \frac{1}{l_m} \int_{x=0}^{x=l_m} |y| dx \quad [2]$$

Both R_t and R_z introduces bias when comes to surfaces that contains local extremities, as both takes account of the minimums and maximums. Therefore, in many other industries, most AM works uses R_a as the standard parameter of surface roughness evaluation.

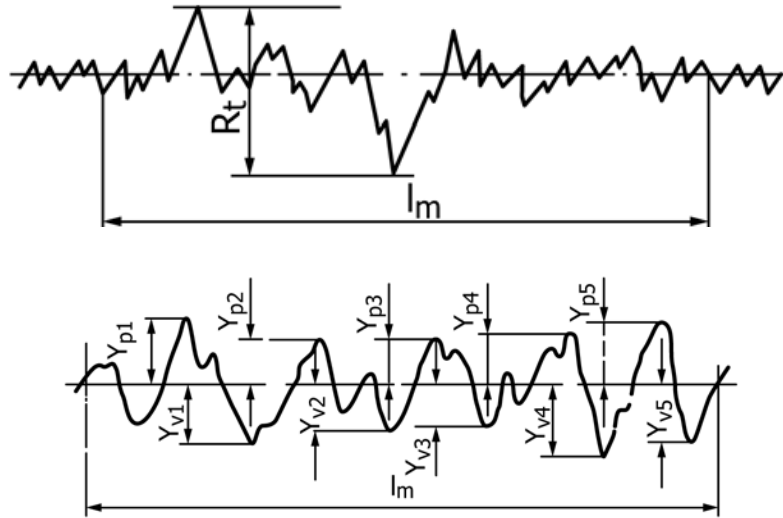


Figure 2-17 Schematic of R_t and R_z evaluation [59]

Strano et al. [17] modified the standard equation for R_a , where by knowing height, f , of the peaks at N locations, the equation can be solved numerically (Eq. 3).

$$R_a \approx \frac{1}{N} \sum_{i=1}^N |f_n| \quad [3]$$

The one-dimensional equation was then modified to take account of the surface roughness of a two-dimensional plane, with the plane defined as $N \times M$ (Eq. 4).

$$R_a \approx \frac{1}{NM} \sum_{i=1}^N \sum_{j=1}^M |f_{ij}| \quad [4]$$

2.4. The staircase-effect

Aside from the process parameters from the machine, the build process imposes dimensional, and most certainly, surface defects during the layer-wise AM process. Since AM process builds in a layer-by-layer manner, continuous smooth surface from the design file are first sliced into discrete layers with a non-zero thickness. The discrete layers coupled with the layer thickness of the AM building process creates visually distinguishable layers, thus depending on the geometry and orientation of the part being build, the layers could create the staircase effect.

The staircase effect is mostly due to the geometry and the design of the parts rather than solidification mechanisms, therefore the complexity to understand and to model the effect of this staircase on the superficial quality of the build parts are less than that of the latter.

Needless to say, novel solutions were developed for unforeseen problems when comes to the staircase effect.

Strano et al. [17] studied the staircase effect on the surface roughness of parts produced by SLM and had created a novel mathematical model that can predict the surface roughness based on the incline angle the surface.

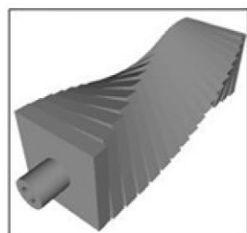


Figure 2-18 The truncheon test part [17]

Process parameters	Level
Laser Power (W)	195
Scanning speed (mm/s)	900
Hatch spacing (mm)	0.1
Layer thickness (μm)	20

Table 2-9 Process parameters for 316L stainless steel. [17]

For the study, truncheon samples (Figure 2-18) were manufactured with stainless steel 316L with process parameter listed in Table 2-9. 18 sections, each with 5° additional rotation, were included. It was observed and confirmed with literature [18], [19], that due to quick melt pool solidification time, ripples were generated from the shear surface tension force on the liquid surface. However, at low inclination angles, the surface roughness can be controlled by

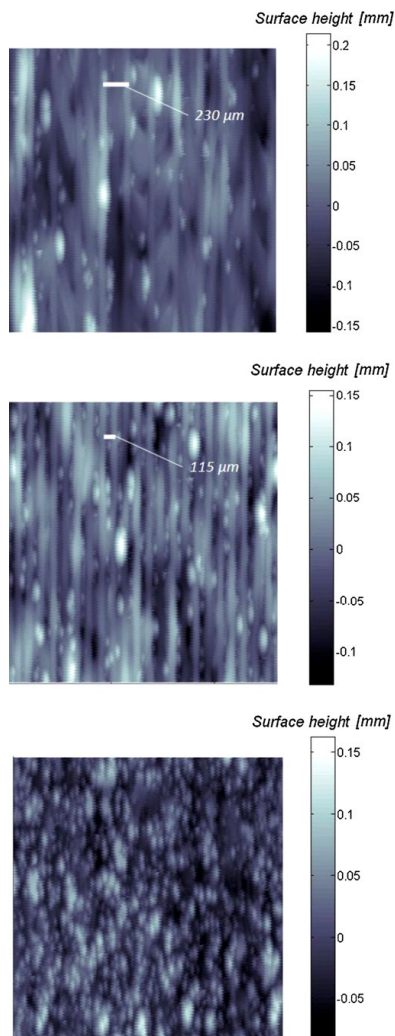


Figure 2-19 Surface profile at surface incline of a) 5° , b) 10° , c) 65° . [17]

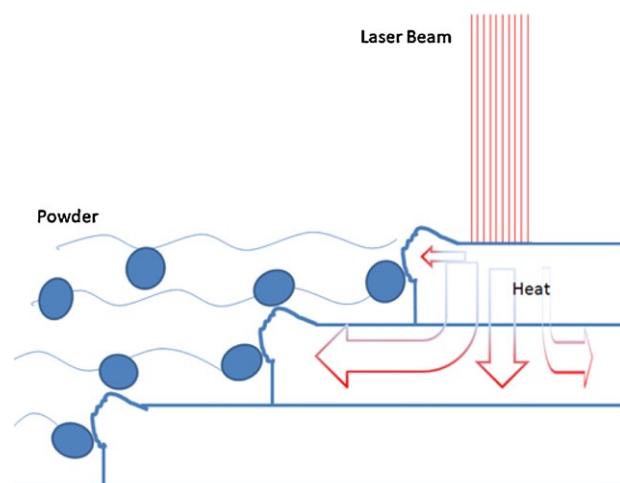


Figure 2-20 Schematic of heat diffusion during laser melting process. [17]

varying the laser hatch spacing, which can re-melt the previous ripple-affected track. As the surface inclination angle increases, re-melting of adjacent track becomes less effective as overlapping become difficult to achieve, thus the staircase effect takes over on effecting the surface roughness.

As the inclination increases, especially beyond 55° as seen in Figure 2-19, the staircase effect levels off due to the balling effect, where insufficient laser energy imposes incomplete bonding of melted powder to the substrate. Spherical particles were formed due to surface tension, thus produces voids inside the part, and increases roughness on the surface of the parts. At higher inclination angle, surface roughness is also affected by the partial bonding of satellite particles. This is coupled with the staircase as seen in the Figure 2-20.

Based purely on the geometry of the staircase profile as seen in Figure 2-21, a simple trigonometry equation (Eq. 5 and 6) can be used to calculate the distance between consecutive ridges on the surface. Empirical measurement validated the accuracy of this model (Figure 2-22).

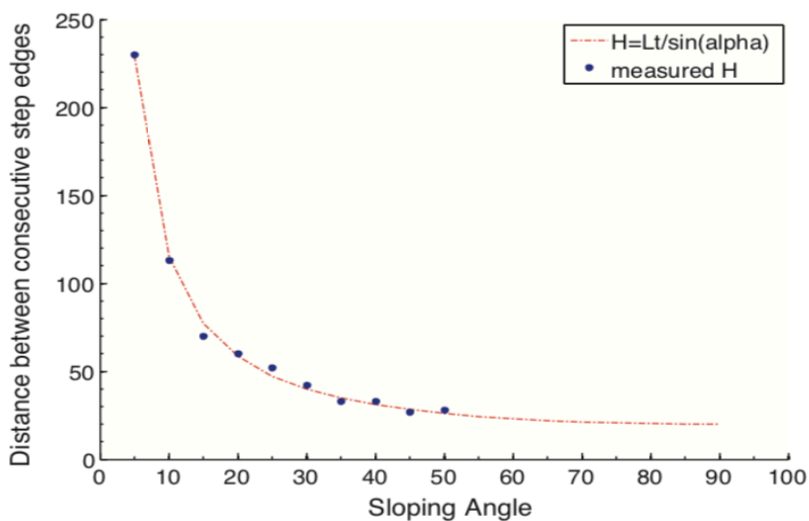


Figure 2-22 Measured and predicted distance between consecutive step edges. [17]

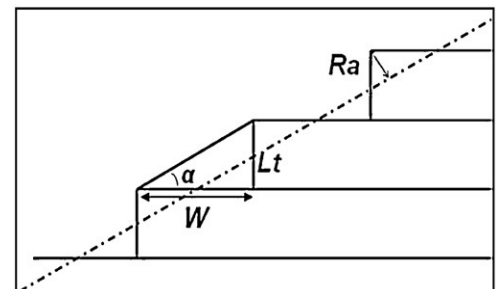


Figure 2-21 The sliced profile schematic. [17]

$$h = \frac{L_t}{\sin(\alpha)} \quad [5]$$

$$R_a = \frac{1}{L} \int_0^L |y(x)| dx = \frac{1}{4} L_t \cos(\alpha) \quad [6]$$

However, this equation does a poor job at predicting surface roughness on the highly inclined surfaces, as it does not take into account the partially bonded particles. It can also be

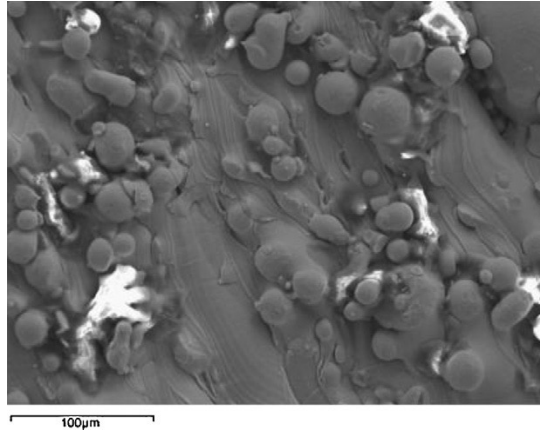


Figure 2-23 Presence of particles on highly sloped surface. [17]

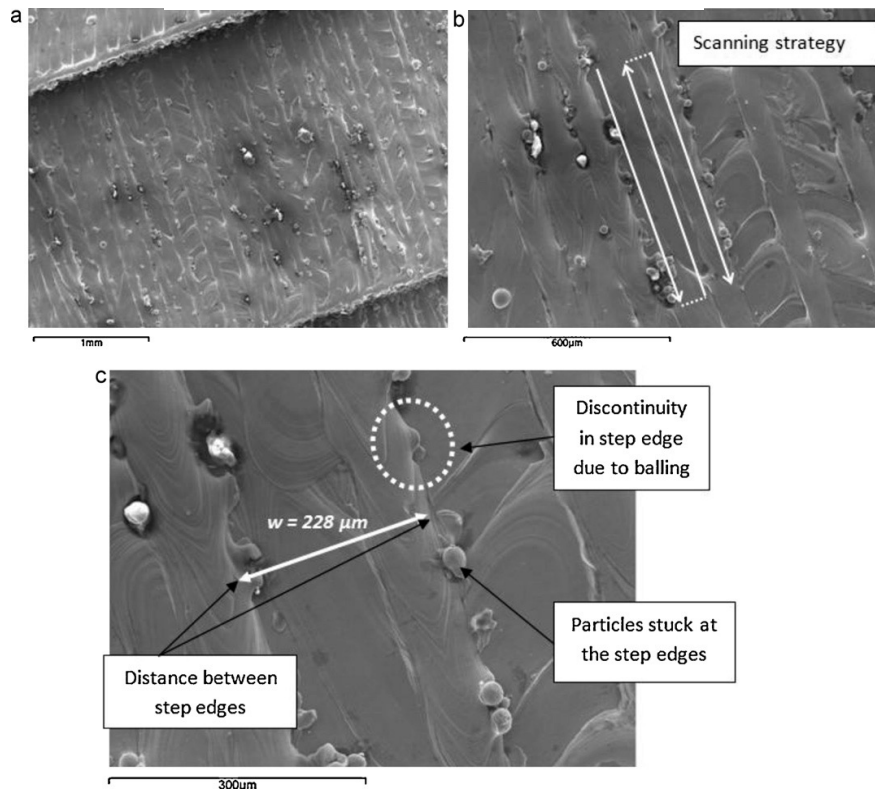


Figure 2-24 SEM picture of slightly inclined surface (sloping angle 5°) (a) at low magnification, (b) at high magnifications, (c) detail of slightly inclined surface. [17]

said that the staircase effect diminishes at very high inclination angle due to complete layer overlap, and the surface roughness at very high angles are mainly from particle bonding and the limited repeatability on the layer overlap, as seen in Figure 2-24 and Figure 2-23.

A novel model was created to take into account the presence of bonded particles to the staircase profile. As seen in the 3-D representation in Figure 2-25, and in the schematic in Figure 2-26, the staircase profile was simplified to three prismatic sections, base layer surface S_1 , base layer surface with partial particle bond S_2 , and the bonded particle S_3 . The integral for each of the sections was taken and combined with the function for calculation of the arithmetic mean of surface height, R_a (Eq. 7, Eq. 8, and Eq. 9).

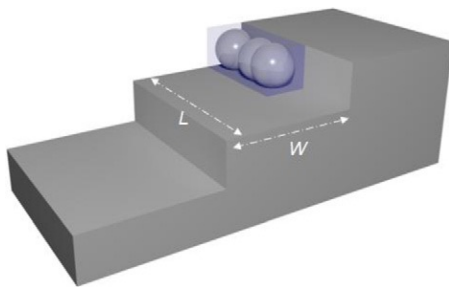


Figure 2-25 Representation in 3D of the proposed model. [17]

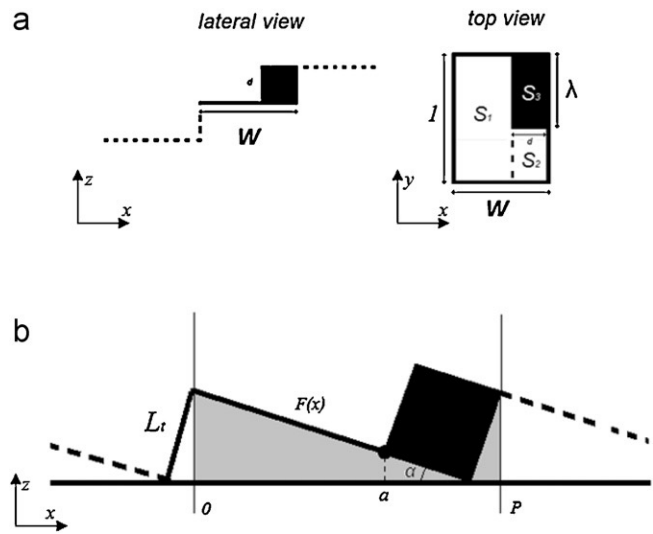


Figure 2-26 Schematic representation: (a) lateral and top view of λ fraction of partially bonded particles; (b) cross section of the modelled surface. [17]

$$R(\alpha, \lambda) \Leftrightarrow \int_S \int |F(x, y) - \bar{F}| dx dy. \quad [7]$$

$$\begin{aligned} R(\alpha, \lambda) &= \int_S \int |F(x, y) - \bar{F}| dx dy \\ &= \int_{S_1} \int |F(x, y) - F| dx dy + \int_{S_2} \int |F(x, y) - F| dx dy + \int_{S_3} \int |F(x, y) - F| dx dy \\ &= \frac{1}{P} \int_0^a |F(x) - \bar{F}| dx + \frac{1-\lambda}{P} \int_a^P |F(x) - \bar{F}| dx + \frac{\lambda}{P} \int_a^P |F'(x) - \bar{F}| dx \end{aligned} \quad [8]$$

$$\bar{F} = \frac{1}{P} \int_0^a F(x) dx + \frac{1-\lambda}{P} \int_a^P F(x) dx + \frac{\lambda}{P} \int_a^P F(x) dx \quad [9]$$

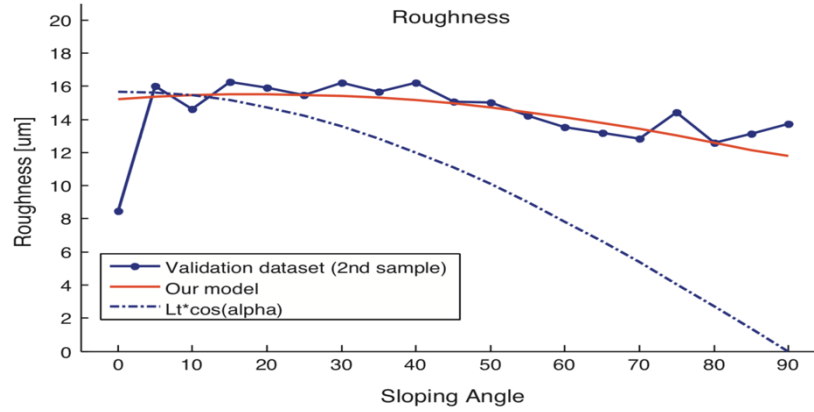


Figure 2-27 Comparison between measured roughness on validation dataset (second sample) and roughness predicted through newly developed model. [17]

$$\min E(\lambda, c) = \sum_{n=1}^N |R_a(\alpha_n) - c \cdot R(\alpha_n, \lambda)| ; 0 \leq \lambda \leq 1 \quad [10]$$

By adjusting λ in Eq. 10, the particle fraction, the novel model was able to fit the validation data from experiment measurement accurately (Figure 2-27).

Another very popular AM technology on the market is the fused deposition modeling (FDM). FDM is commonly used in fabrication of thermal plastic materials, as it extrudes heated, semi-molten thermoplastic through a thin nozzle, sometimes in a temperature-controlled environment, to build the parts layer by layer. Layers are built by the tracing of contours in the x-y axis, where height z is controlled by the layer thickness. since this process does not involve volatile materials and high energy input, like in of SLM, therefore the part quality is more tolerant to the process parameters.

Due to the large size of the extruded filament, as well as the staircase effect from the slicing and layer wise building process, larger surface roughness can be observed with FDM

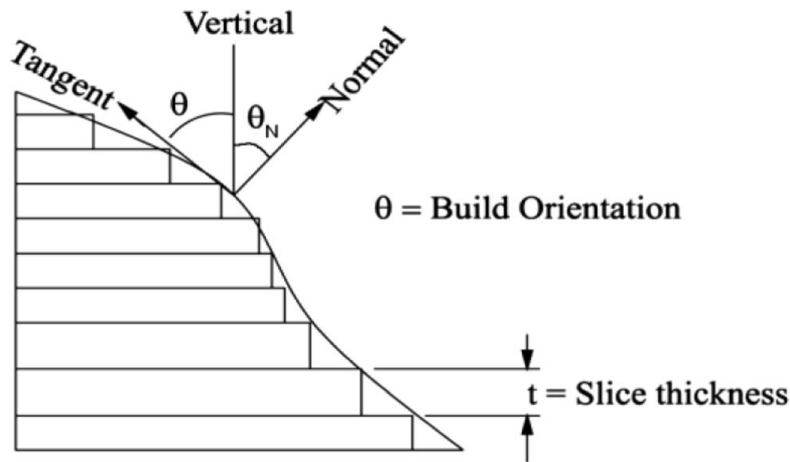


Figure 2-28 Schematic of surface roughness model. [20]

technique when comparing to SLM. However, since this rough surface is mostly caused by the geometry of the filament and build orientation, relatively accurate theoretical models for surface can be created for the FDM technology.

In their research, Rahmati and Vahabli [20] compared the performance of five of the well-known surface roughness models presented in literature. In earlier literature, cusp height

was identified to have significant relation with surface roughness (Figure 2-28). Using this finding, Eq.11[21], Eq.12[22], and Eq.13[23], present the mathematical model for surface roughness prediction, which take account of the layer thickness t in mm, the build angle θ in degrees, and in Ahn model, for the surface profile angle ϕ in degrees.

$$R_a = 1000t \sin\left(\frac{90 - \theta}{4}\right) \tan(90 - \theta) \quad [11]$$

$$R_a = \frac{1000t}{2} \cos(90 - \theta) \quad [12]$$

$$R_a = \frac{1000t}{2} \left| \frac{\cos((90 - \theta) - \phi)}{\cos(\phi)} \right| \quad [13]$$

Pandey et al.[24] identified that layer thickness and build orientation had significant effect on surface roughness and had developed a semi-empirical model Eq.14, where w is a dimensionless adjustment parameter for supported surface.

$$R_a = \begin{cases} (69.28 \sim 72.36) t / \cos\theta, & 0 \ll \theta \ll 70 \\ \frac{1}{20} (90R_{a70} - 70R_{a90} + \theta(R_{a90} - R_{a70})), & 70 < \theta < 90 \\ 117.6 \times t, & \theta = 90 \\ R_{a(\theta-90)}(1 + w), & 90 < \theta \leq 180 \end{cases} \quad [14]$$

Finally, in the model created by Byun et al. Eq.15, further parameters were added. R_1 and R_2 represents the radius of fillet in mm, and radius of corner in mm, respectively.

$$R_a = \begin{cases} 0, & \theta = 0, \frac{\pi}{2}, \pi \\ \frac{1000t}{4} \cos(90 - \theta) - \frac{(R_1^2 + R_2^2) \left(1 - \frac{\pi}{4}\right) \sin(90 - \theta)}{1000t} + \frac{\left((R_1^2 + R_2^2) \left(1 - \frac{\pi}{4}\right)\right)^2}{(1000t)^3} \tan(90 - \theta) \sin(90 - \theta), & 0/w \end{cases} \quad [15]$$

To evaluate the models, a truncheon sample of 220 x 30 x 30 mm³, with 36 cuboids of 5° rotation increment relative to each other, was fabricated using layer thickness of 0.254mm (Figure 2-30).



Figure 2-30 The truncheon test part. [20]

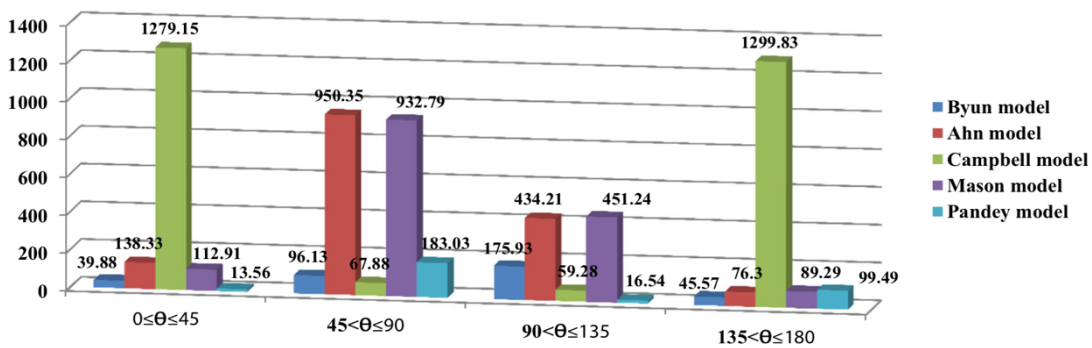


Figure 2-29 Mean absolute percentage error values (%) for different analytical models. [20]

The measured Ra was compared with each of the model predictions (Figure 2-31), and the Pandey model was found to have the least error across range of build angles (Figure 2-29). This conclusion further suggests the superiority of empirical elements when creating models that involves complex interaction between variables.

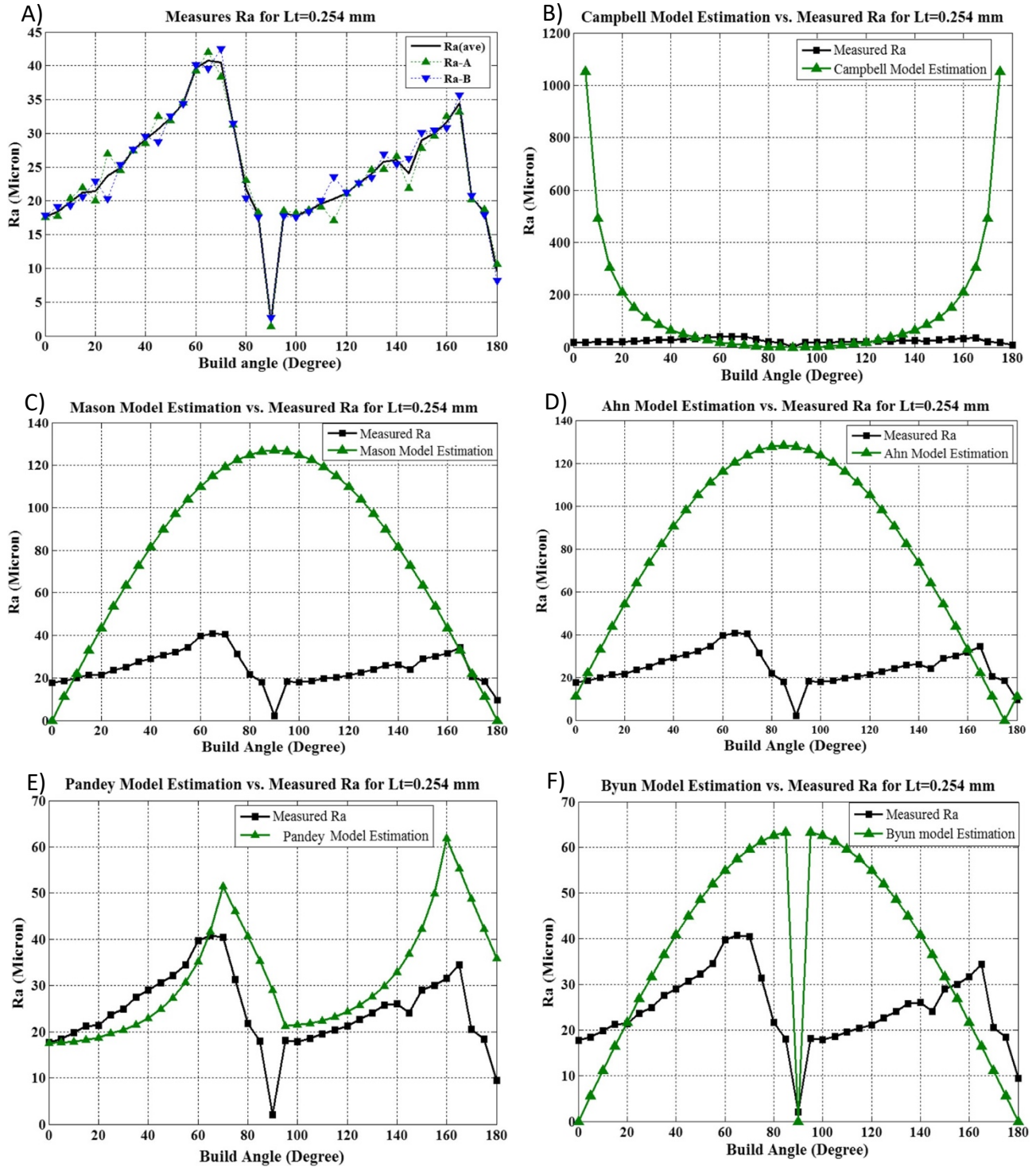


Figure 2-31 Comparison of A) measured Ra on the test part and: B) Campbell model, C) Mason model, D) Ahn model, E) Pandey model, and F) Byun model. [20]

3. Experimental work

3.1. Introduction

As discussed in Chapter 2, the quality of an additively manufactured component needs to satisfy not only the superficial and cosmetic qualities, but also mechanical and internal qualities. The high strength to weight ratio of high strength aluminum (Al) alloys are ideal for light-weighting applications. High strength Al alloys are commonly used in transportation industries (aerospace, automotive, and space), as well as biomedical applications [25].

During the selective laser melting (SLM) process, the fabrication material undergoes cycles of rapid heating, solidification, and cooling, which imposes limitations on the selection of materials. One of the major challenges is the coefficient of thermal expansion (CTE) of the material, as well as the reflectivity, both of which are high for high strength Al alloys. This in turn narrows the window to find the optimal SLM process parameters to manufacture high strength Al alloy parts. Galy et al. [26] identified the major defects for Al alloys to be porosity, hot tearing, anisotropic mechanical properties, and surface quality. The primary cause of porosity and hot tearing was identified to be from the high reflectivity of Al alloy, causing the loss of absorbed laser beam energy.

Quality of part can be improved by controlled mixing of Al alloy powder with specialty powders [27, 28]. Martin et al. [6] used zirconium nano-particles as additives to the Al6061 and Al7075 base alloy powder and were able to achieve crack-free solidification. However, this approach not only imposes additional cost to production, but also lowers the mechanical properties compared to the original alloy. Certain SLM process parameters can be adjusted and customized without the modification to powder feed stock to achieved desirable part quality.

Prior works found in literature had studied the effect of SLM process parameters on Al alloy qualities [29 - 35] in addition to the works presented in Chapter 2. The effect of layer thickness was studied by Sufiiarov et al. [36] who found that for Inconel 718, 30 μ m layer thickness produces superior strength and lower elongation than 50 μ m layer thickness. Nguyen et al. [37] observed that as the layer thickness decrease from 50 μ m to 20 μ m, improvement in dimensional accuracy and part density are achieved. Cheng et al. [38] observed that at 45 $^{\circ}$ and 67 $^{\circ}$ layer orientation scan strategy produced parts with minimum stress and deformation.

Design of experiments (DOE) can be found in literature when studying the effects of SLM process parameters on AlSi10Mg alloy [6, 39 – 42]. Using response surface method (RSM), Read et al. [40] were able to obtain the optimal energy density, 60J/mm³, for AlSi10Mg alloy for minimum porosity. Abouelkhair et al. [43] used one-factor-at a-time (OFAT) method to achieved 99.77% dense part with the combination laser power, scan speed, and hatch spacing. Surface roughness was studied by Hitzler et al. [44], where part location on build plate had a significant effect on the surface quality. The Tauguchi method was used to study the effect of laser power, scan speed, and hatch spacing on the surface roughness by Calignano et al. [45]. They found that low surface roughness can be obtained with scan speed of 900 mm/s, laser power of 120 W, and hatch spacing of 0.1 mm. They also concluded that laser power had significant effect on the surface roughness. Han et al. [46] observed increasing laser scan speed results in improvement in dimensional accuracy.

It is worthwhile to note that the studies above and the majority of studies found in literature currently are limited with SLM laser power of 200W. With the development in SLM technology, majority of the SLM machine currently on in service can reach 400W and above,

which widens the window of process parameters, and could change the part quality significantly.

Flucher et al. [39] reported that the process map for SLM should be updated regularly as to keep up with the development in both the material and the machine. Due to the limitation of the SLM laser power, Al6061 was rarely used for SLM. The high reflectivity, high CTE, coupled with low Mg and Si content of Al6061 and Al7075 impose challenges such as insufficient melting, oxidation formation [47], and hot tearing [48]. However, with the update in the SLM capability, fabrication with high strength Al alloys may be improved, which is the aim of this current study.

The SLM process is of high complexity in terms of microstructure formation, thermal evolution, and solidification process even with only few major process variables eg., laser power, scan speed, hatch spacing, and layer thickness. This is due to the complex interaction between the variables, the chemical compositions of the powder material, and the uncertainty and variability of melt as induced by the rapid cycles of localized melt and re-melt of substrate. As observed in Chapter 2, even with process of relative simplicity such that of the fuse deposition modeling (FDM), high level of uncertainty still existed. Thus, as observed by Rahmati and Vahabli [20], out of the five well known models for predicting surface roughness for FMD, highest accuracy was achieved based on empirical model. Therefore, to best suit the scope and expertise of the author, in the current study, works were accomplished to develop process maps for Al6061 and AlSi10Mg alloy empirically using regression models.

3.2. Design of Experiment

3.2.1. Method

3.2.1.1. Parameters

Response variables were selected for comprehensive evaluation of the parts quality, they range from cosmetic quality to mechanical properties:

- Surface Roughness (Ra).
- Microhardness (Hv).
- Relative Density (%).
- Dimensional Accuracy (mm).
- Ultimate Tensile Strength (MPa)
- Yield Strength (MPa)

As discussed in chapter 2, many variables exist for the SLM process, but few have significant contribution to affect the quality of the fabrication due to the sparsity effect [8]. It was understood that the input energy density from the laser that melts the powder/substrate is the most influential process parameter on the parts' quality. The energy density (J/mm^3) is described in Eq.16

$$\rho_E = \frac{P}{h \times v \times t} \quad [16]$$

where P is power output (W) of the laser, v is the scan speed (mm/s) of the laser, t is the thickness (mm) of metal powder for each layer worth of exposure, and h is the hatch spacing (mm) between each pass of the laser.

Since each batch of print requires a fixed layer thickness, thus to vary layer thickness would require multiple batch of prints, which will be costly due to machine setup as well as longer run time.

The three factors that were chosen:

- Laser Power (W)
- Scan Speed (mm/s)
- Hatch spacing (mm)

Since energy density is of importance, therefore the settings of the levels of the three input factors were carefully chosen to ensure uniformity in variability of the of the energy densities, while maintaining uniformity in variability in the levels of the factors. This ensures the design of the DOE will be unbiased.

Layer thickness kept at 0.03mm, which is the default as suggested by the SLM machine manufacturer, EOS GmbH Electro Optical Systems, Krailling, Germany.

The levels of the factors were chosen from the calculated energy density. AlSi10Mg is a relatively popular aluminum alloy, compared to Al6061, used in additive manufacturing. From literatures, AlSi10Mg can be printed at energy density ranging from 20J/mm³ to 90J/mm³ with no major failures. Therefore, the energy density for Al6061 were set to be from 40J/mm³ to 110J/mm³, slightly higher than that of AlSi10Mg as Al6061 contains less silicon (~97% by weight aluminum compared to ~90% by weight from AlSi10Mg), which lowers the alloy's emissivity, thereby more energy requiring for melting.

With the energy density range chosen, the levels for the three factors can then be calculated. Four levels Laser power, Hatch spacing, and Scan speed were conceptualized. Each

with equal variability, while containing the default machine parameter at the same time. They are:

- Power: 200W, 300W, 350W, **370W**
- Hatch Spacing: 0.1mm, 0.15mm, **0.19mm**, 0.25mm
- Scan Speed: 800mm/s, 1000mm/s, **1300mm/s**, 1500mm/s

There are six possible different selections of two-level settings per factor, and there are three different factors, therefore 6^3 yields 216 different combinations of these factors to make two level full factorial experiments. All 216 combinations were generated with Excel, and evaluated based on the following four metrics to determine which set of combinations can be suited for the experiment:

- **Standard deviation:** SD of calculated energy densities in each set of 8 runs. This is parameter to evaluate the uniformity of variability of the energy densities, therefore smaller SD is desired.
- **Minimum and Maximum:** each possible set should have a minimum and maximum calculated energy density that falls between 40J/mm^3 and 110J/mm^3 .
- **Range:** Calculated from minimum and maximum calculated energy density for each set of runs. This parameter combine with SD will evaluates the amount of variability in the energy densities, where larger range is desirable. Ideally range of 70J/mm^3 .

3.2.1.2. *Parameter selection*

Combinations	Power (W)	Hatch Spacing (mm)			Scan Speed (mm/s)	
1	200	300	800	1000	0.1	0.15
2	200	350	800	1300	0.1	0.19
3	200	370	800	1500	0.1	0.25
4	300	350	1000	1300	0.15	0.19
5	300	370	1000	1500	0.15	0.25
6	350	370	1300	1500	0.19	0.25

Table 3-1 The six possible combinations of Power, Hatch spacing, and scan speed.

Table 3-1 aids in the creation of all possible combinations of full factorials. Table 3-1 assigns a number for each range of power, scan speed, and hatch spacing. Table 3-2 was then created using the numbers.

Power (W)	Hatch Spacing (mm)	Scan Speed (mm/s)
1	1	1
2	1	1
3	1	1
4	1	1
5	1	1
6	1	1
1	2	1
2	2	1
3	2	1
4	2	1
5	2	1
...
6	6	6

Table 3-2 All possible 2³ full factorial DOE represented at code.

By matching the numbers in Table 3-2 to the settings in the reference table, Table 3-1, the full set of 216 different full factorial design can then be generated in Table 3-3.

Power (W)		Hatch Spacing (mm)		Scan Speed (mm/s)	
200	300	0.1	0.15	800	1000
200	350	0.1	0.15	800	1000
200	370	0.1	0.15	800	1000
300	350	0.1	0.15	800	1000
300	370	0.1	0.15	800	1000
350	370	0.1	0.15	800	1000
200	300	0.1	0.15	800	1300
200	350	0.1	0.15	800	1300
200	370	0.1	0.15	800	1300
300	350	0.1	0.15	800	1300
300	370	0.1	0.15	800	1300
...
350	370	0.19	0.25	1300	1500

Table 3-3 Full set of 216 different 2³ full factorial design.

Since the size of each of the 2³ designed experiment is eight, thus eight different resultant energy densities per DOE, therefore a brute-force calculation can be carried out to find out all eight possible energy densities. Using the standard deviation function, Eq.17, where n is the total number of energy density per DOE, i is the iteration, ρ_E is the energy density, and $\bar{\rho}_E$ is the average energy density of the DOE.

$$SD = \sqrt{\frac{\sum_{i=1}^n (\rho_{Ei} - \bar{\rho}_E)^2}{n - 1}} \quad [17]$$

Functions were then created in Excel to create the auto-populated table (Table 3-4) that contains the four characteristics which the fitness of the DOE will be determined.

SD	Min	Max	Range
25.73	44.44	125.00	80.55
33.27	44.44	145.83	101.38
36.44	44.44	154.16	109.72
26.38	66.66	145.83	79.16
28.38	66.66	154.16	87.50
27.85	77.77	154.16	76.38
30.04	35.08	125.00	89.91
36.90	35.08	145.83	110.74
39.82	35.08	154.16	119.07
33.92	52.63	145.83	93.20
35.79	52.63	154.16	101.53
36.64	61.40	154.16	92.76
...
6.68	31.11	49.93	18.82

Table 3-4 The standard deviation, minimum, maximum, and range of the calculated energies for each of 216 possible full factorial design.

The limit for SD was chosen to be below 25, the minimum energy density to be greater than 20, the maximum energy density to be less than 100, and range to be greater than 60. These criteria were then used to set the rules for conditional formatting, where the cells that falls within the rules are highlighted. Through a visual inspection, suitable DOE combinations were identified when all four cells in that row was highlighted green. Thus, from the 216 possible combinations, 17 DOEs were identified as potential candidate for experiment as in Table 3-5.

comments	options	Power (W)		Scan Speed (mm/s)		Hatch Spacing (mm)		Energy Density (J/mm ³)				
								SD	min	max	range	
best range	1	200	350	0.15	0.25	800	1300	23.96	20.51	97.22	76.70	
	2	200	300	0.1	0.19	1000	1500	24.41	23.39	100.00	76.60	
	3	200	350	0.15	0.19	800	1500	24.42	23.39	97.22	73.83	
Best variety	4	200	300	0.1	0.19	1000	1300	24.02	26.99	100.00	73.00	
	5	200	370	0.1	0.19	1300	1500	24.88	23.39	94.87	71.47	
	6	200	350	0.15	0.25	800	1000	23.19	26.66	97.22	70.55	
	7	300	350	0.15	0.25	800	1500	24.24	26.66	97.22	70.55	
	8	200	300	0.1	0.15	1000	1500	21.86	29.62	100.00	70.37	
	9	200	350	0.15	0.19	800	1300	22.93	26.99	97.22	70.23	
	10	300	350	0.15	0.25	800	1300	22.43	30.76	97.22	66.45	
	11	200	350	0.1	0.19	1300	1500	23.02	23.39	89.74	66.35	
	12	200	300	0.1	0.15	1000	1300	20.76	34.18	100.00	65.81	
	13	200	350	0.15	0.19	800	1000	21.07	35.08	97.22	62.13	
	14	300	350	0.15	0.19	800	1500	22.38	35.08	97.22	62.13	
	15	200	370	0.15	0.25	1000	1300	20.14	20.51	82.22	61.70	
	Best Standard deviation	16	200	370	0.19	0.25	800	1300	19.70	20.51	81.14	60.62
		17	200	350	0.1	0.15	1300	1500	20.56	29.62	89.74	60.11

Table 3-5 Potential full factorial designs that are suited based on the fitness requirements.

3.2.1.3. *Background variables*

Two main source of background variables can be identified as:

- Powder:
 - Morphology: the size and shape of the particle will determine how well the powder spreads at the beginning of each layer that is being built. To keep the change in powder quality from affecting the result, the powder feed stock was all bought from one supplier (LPW) under the same production batch.
 - In depth x-ray diffraction analysis were performed on the powder samples to account for anomalies in the surface roughness and dimension accuracy data.
- Machine:
 - Environment: At an elevated temperature, metals/alloys become more sensitive to oxidation. Similar to TIG and MIG welding, SLM operates at the melting point of the metal, thus inert gas is used to purge the build chamber of oxygen. Since the chamber is not under vacuum, therefore the oxygen content can never be zero, it varies around 0.2%, depending on the ambient temperature, pressure, and inert gas (Argon) tank pressure. To minimize the effect of this, all sample prints were made in one built run, thus subjecting them under the same machine atmosphere condition.

3.2.2. Experiment

One of the major strengths of Full factorial DOE is that it can provide information on the interactions between the input factors. Because of this, the major application for full factorial DOE is to filter out ineffective input factors, and to find out optimal input factors set by the outputs, through gradual refinement of experiments. However, gradual refinement of experiments can be costly in time and money as it requires multiples experiment trials. When the objective is to model and map out the behaviour of the outputs, a cost-effective method can be employed.

There is always the trade-off between resolution and cost. A 3^3 full factorial will provide high quality polynomial models for the main effects, as well as all of their interactions with each other. However, running 27 samples, each measuring 15mm x 15mm x 15mm, with three replications, will take up the entire build plate, leaving no room for tensile coupons. Thus, to save real-estate and cost of experiment, two 2^3 full factorial DOE was conducted, with parameters selected from Table 3-5, each overlap at the default process parameters. With three replicants, 48 total cube samples were placed on the build plate, thus freed up real estate for tensile coupons. The total experiment dropped from 27 as from a 3^3 full factorial to 16 from the combined 2^3 full factorial, with the compromise on resolution and lack of 3-level interactions. This issue however is justified by the pareto principle, which describes the Sparsity-of-effects, [8] that majority of the effects were caused by few factors. In terms of DOE, the sparsity-of-effects also applies that the significance of the effect on outputs are inverse exponentially related to the order of the effect, ie. higher order interactions generally have much lower effect on the outputs than lower level factor interactions. Thus, losing the 3-level

interaction between Power, Scan speed, and Hatch spacing to gain resource to print tensile samples was justified.

The build plate was divided in half to accommodate for the two sets of DOEs as seen in Figure 3-2. The location on the build plate at where the samples were printed can have potential effect on the final printed part due to the inert gas flow from the south end of the build plate to the north end. burnt particles from the laser melting process will be carried by the gas current, therefore generally parts at the north end of the build plate will experience poorer quality from the accumulation of burnt particles.

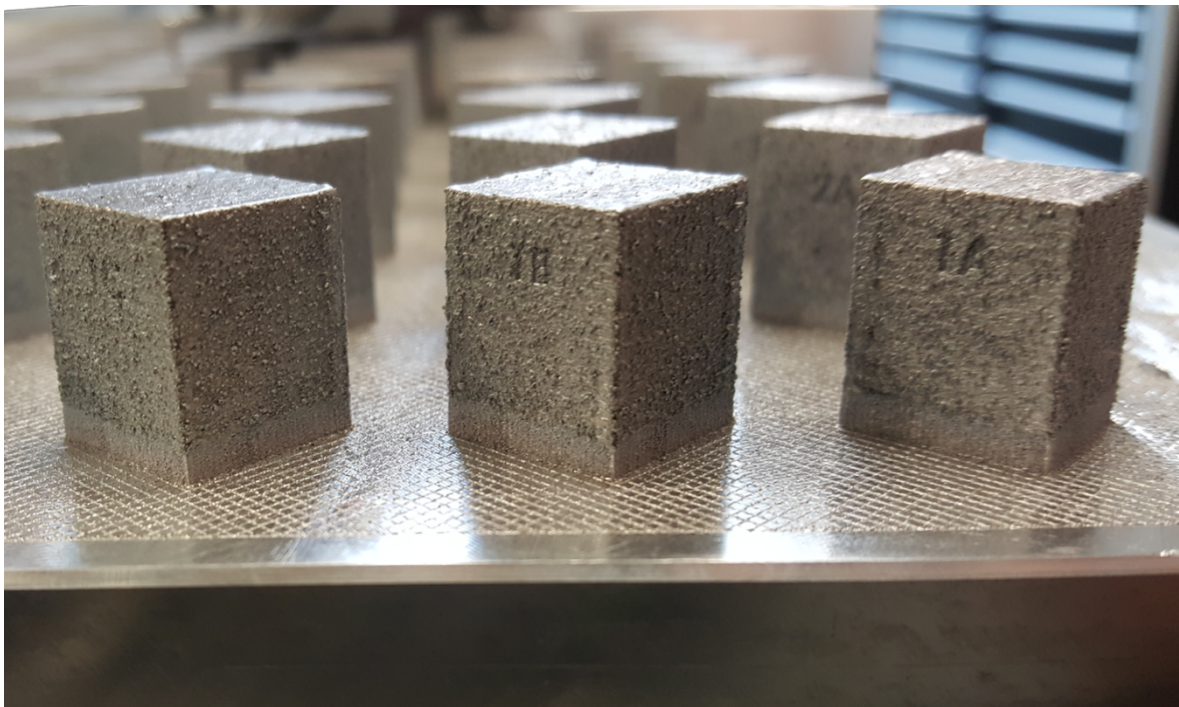


Figure 3-1 The cubic samples.

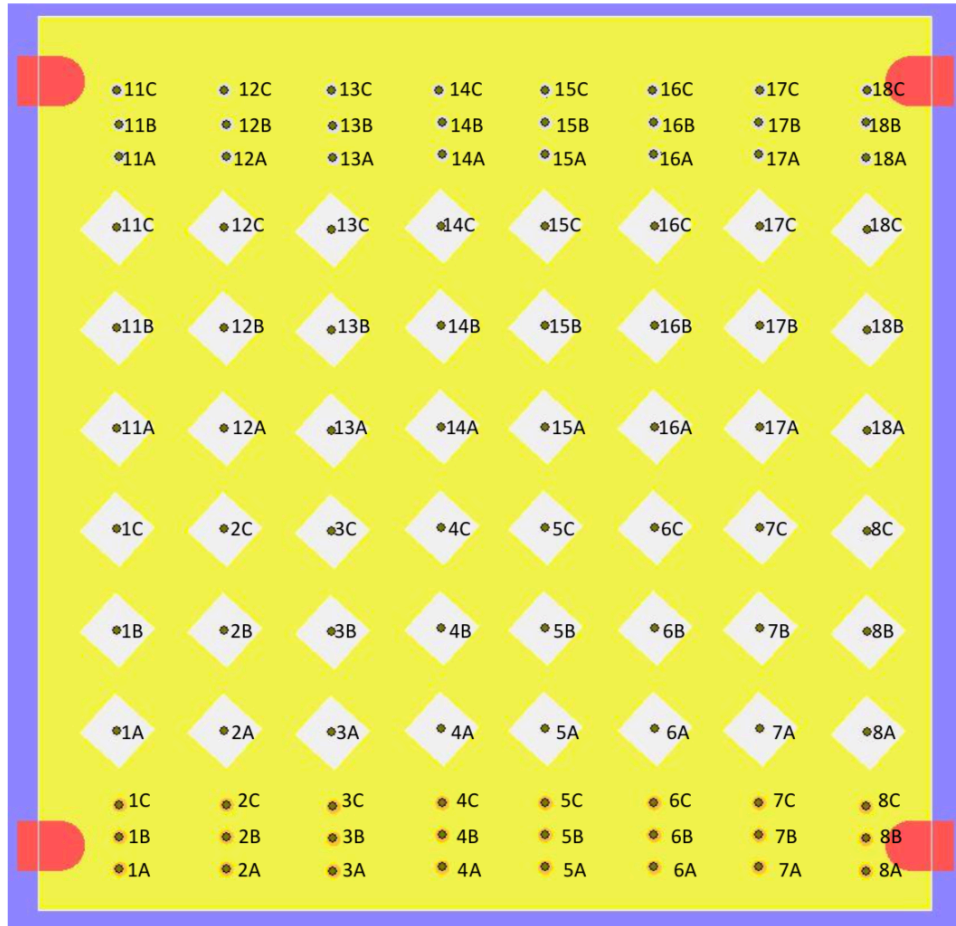


Figure 3-2 Schematic of sample placement on the build plate. The cubic sample occupies the enter of the build plate, while tensile coupons were place towards the edge of the build plate.

Random placement of samples could eliminate this background disturbance. However, doing so significantly increase the manual work required to keep track on the location of each sample. Moreover, EOS M290 is a commercial SLM unit, where failure of prints due to location contamination were accounted for when the machine was designed and built. Therefore, samples were not placed on the build file randomly.

Sample#	Power (W)	Scan Speed (mm/s)	Hatch Spacing (mm)	Energy Density (J/mm³)
AS1	370	1000	0.19	65
AS2	370	1300	0.15	63.2
AS3	370	1300	0.19	50
AS4	350	1300	0.19	47.2
AS5	370	1500	0.19	43.3
AS6	300	1300	0.19	40.5
AS7	370	1300	0.25	38
AS8	200	1300	0.19	27

Table 3-6 The SLM process parameters applied for producing the AlSi10Mg_200C samples.

Sample#	Power (W)	Scan Speed (mm/s)	Hatch Spacing (mm)	Energy Density (J/mm³)	Sample#	Power (W)	Scan Speed (mm/s)	Hatch Spacing (mm)	Energy Density (J/mm³)
1A	370	1000	0.1	123.3	11A	370	800	0.15	102.8
2A	300	1000	0.1	100	12A	350	800	0.15	97.2
3A	370	1300	0.1	95	13A	370	800	0.19	81.1
4A	300	1300	0.1	76.9	14A	350	800	0.19	76.8
5A	370	1000	0.19	65	15A	370	1300	0.15	63.2
6A	300	1000	0.19	52.6	16A	350	1300	0.15	59.8
7A	370	1300	0.19	50	17A	370	1300	0.19	50
8A	300	1300	0.19	40.5	18A	350	1300	0.19	47.2

Table 3-7 The SLM process parameters used for building the Al6061_200C samples.

The build parameters for both AlSi10Mg and Al6061 are listed in Table 3-6 and Table 3-7 along with their sample names in short form, which are used in the description in the following sections.

3.3. Microstructure and mechanical properties

3.3.1. Microstructure

Three techniques were used for the characterization of microstructure for both Al6061 and AlSi10Mg. The Nikon LV100 optical microscope was used to evaluate microstructure of the sample surfaces. The TESCAN VP SEM was used to further evaluate the microstructure of the etched parts by investigating the grain size and structure. Burker D8 DISCOVERY XRD was used to determine the phase pattern of the samples from both Al6061 and AlSi10Mg along different orientations.

The polishing and etching procedure were performed under the method suggested by Maamoun et al. [49].

3.3.2. Mechanical properties

3.3.2.1. *Microhardness*

The Clemex CMT automatic hardness tester was used for the microhardness measurements. The microhardness measurements were performed in accordance to ASTM E384-17 standard. The hardness of the samples was measured both in the Z (build) direction, as well as the XY plane. Five indentations were performed on the XY plane, and 10 indentations for the Z direction, using 200gf load with 10s dwell time.

3.3.2.2. Tensile properties

The tensile test samples were fabricated with the dimension in accordance with ASTM E8/E8M-16a standard. The small tensile samples have a gauge length of 25mm and a gauge diameter of 2.5mm.

Basic polishing with 250 grit sand paper was performed on the samples for comparison of the effect of surface roughness on tensile strength.

The tensile test was performed on MTS Criterion 43 with 50kN applied load and done in accordance with ASTM E8 standard.

3.4. Density, Surface roughness, and Dimensional accuracy

3.4.1. Density

Archimedes method was used for the density measurement. MD-200S electronic densimeter was used under the ASTM B962-17 standard. Samples were tested before and after surface polishing with 300grid sand paper for the evaluation of surface porosity on the overall part density.

3.4.2. Surface roughness

A Mitutoyo SJ-410 surface tester was used to measure the surface roughness. This type of tester uses a stylus with a fine tip that is attached to a motorized track and an angle sensor. The motor will drag the stylus providing linear motion, any bumps on the tested surface will induce vertical motion on the stylus, which are picked up by the sensor.

ASTM D7127-17 standard was followed for the measurements.

Five measurements were taken for the surface roughness, each at 4.5mm interval on the top surface of the samples. The melt track creates grooves that can affect the overall surface roughness. To evaluate the entirety of the surface, the average of five surface measurements of various directions were taken. Surface texture of some selected samples were taken with A light microscope (Alicona Infinite Focus G5) at 10mm x 10mm test area using 10x magnification. This also served to validate the surface roughness results from the mechanical stylus [41].

The results from the Mitutoyo SJ-410 were saved onto a SD card, which were then imported to Excel for formatting, then populated into the design worksheet in Minitab.

3.4.3. Dimensional accuracy

Mitutoyo CRYSTA-Apex S544 Coordinate Measurement Machine (CMM), with 0.1um resolution and 500mm x 400mm x 400mm work area, was used for the measurement of the dimension of the cubic samples. Geometric dimensions and tolerance (GD&T) were evaluated with the SP25M stylus attachment. 10 measurement points were probed for each surface (except for the bottom face), and flatness, perpendicularity, parallelism, and part lengths were recorded and evaluated.

4. Results and Discussion

4.1. Powder characterization

Powder characterization is the first step to ensure and to control the quality of fabrication. As reported by Sutton et al. [36], the method by which the powder feed stock was produced, i.e., gas, water, or plasma atomization, produces different powder morphology, microstructure, and chemical composition.

Gas-atomized AlSi10Mg and Al6061 powders were used in throughout the study, and are supplied by LPW Technologies, Imperial, USA. The powders characterizations were performed in accordance to ASTM F3049-14. All powders were sieved through 75 μ m mesh as to reflect same process before loading the powder to the SLM machine. TESCAN VP Scanning Electron Microscope (SEM) was used for the observation of the morphology of the powder particles, Figure 4-1.

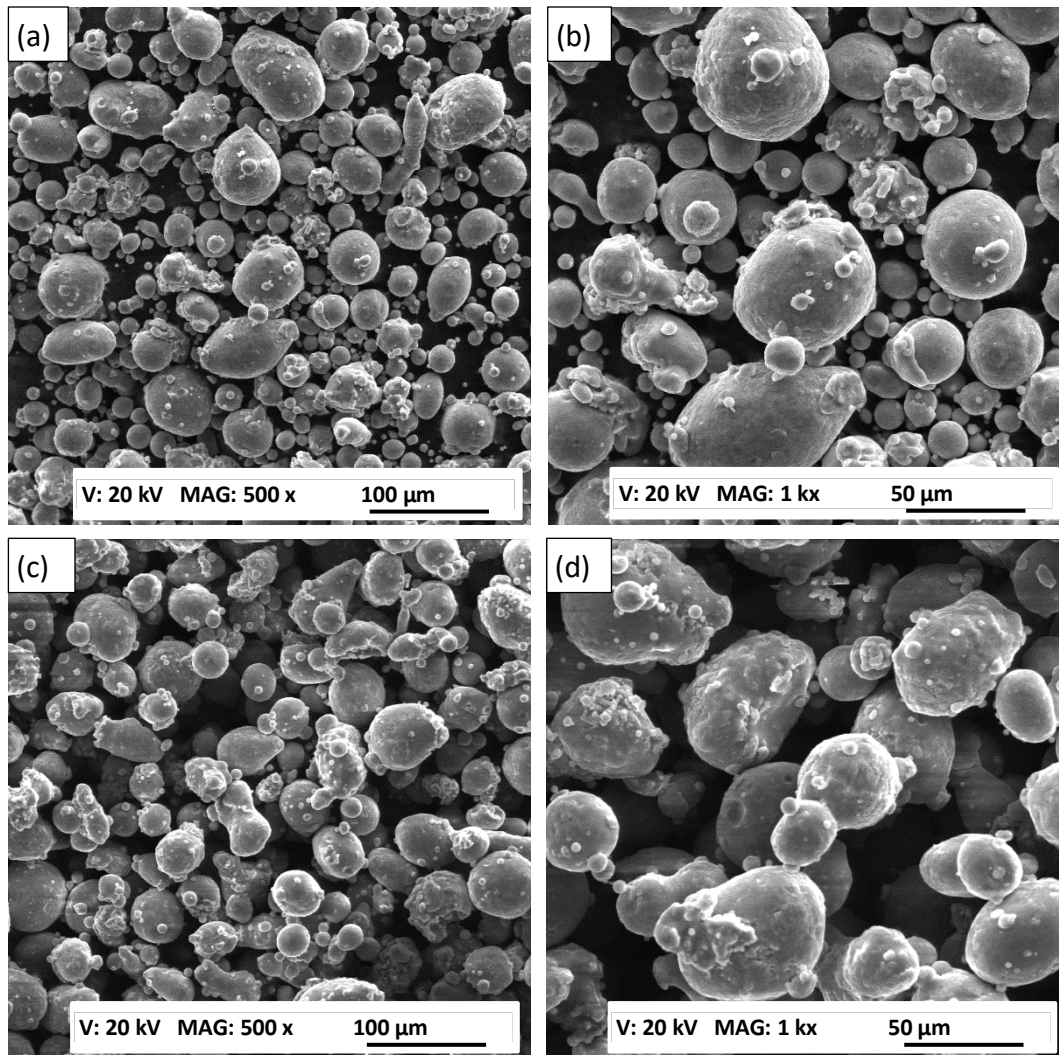


Figure 4-1 SEM images of powder morphology: (a,b) Al6061, (c,d) AlSi10Mg

High irregularity in powder morphology was observed, with the presence of both elongated and irregular-shaped particles in both powder samples. Flowability and powder layer homogeneity can be reduced due to this morphological irregularity, thus negatively affecting the quality of the parts fabricated [42]. As observed in Figure 4-2, a wide range of size for the powder particles were found in both materials. This increases the bulk density of the powder feed stock, because when packing the powders, small particles will fill the voids between larger particles. However, this increase in bulk density further reduces the flowability from the powder cohesion and inter-particle force [42].

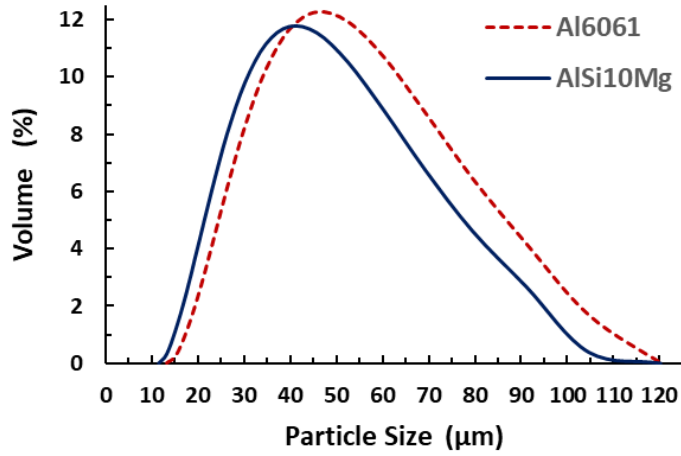


Figure 4-2 Particle size distribution of the Al6061 and AlSi10Mg powders.

Table 4-1 lists the chemical compositions of the elements present in both powder samples as detected via Energy X-ray Dispersive Spectroscopy (EDS), along with the X-ray Diffraction (XRD) analysis (Figure 4-3), comprehensive powder characterization was performed.

Element	Si	Mg	Cu	Fe	Al
Al6061 wt%	1.2	0.77	0.32	0.90	Balance
AlSi10Mg wt%	11.34	0.28	0.08	0.32	Balance

Table 4-1 EDS analysis of the Al6061 and AlSi10Mg powders chemical composition.

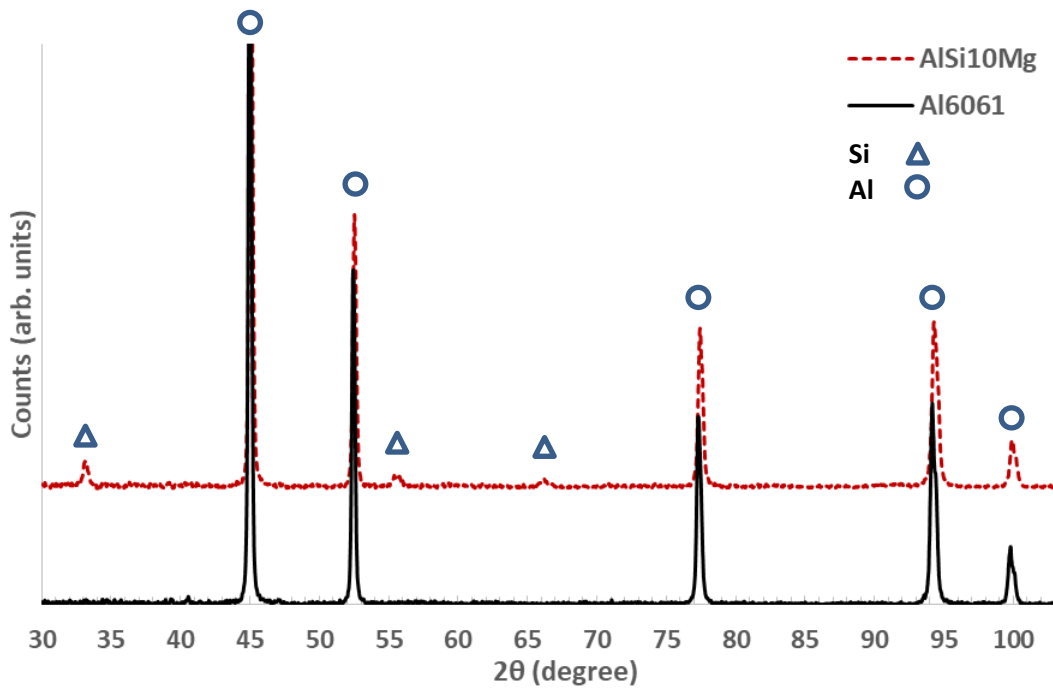


Figure 4-3 XRD phase patterns of the Al6061 and AlSi10Mg powders.

Particle size distribution (PSD) was performed using laser diffraction by water dispersion of the powders. A positive skewed profile for the particle size distribution (PSD) can be observed in Figure 4-2. Compared to a profile of a negatively skewed or a Gaussian distribution, the positive skewed PSD profile can yield better surface quality due to increased laser energy absorption [42], [50]. Presence of large particles (120 μm) was observed in and confirmed in Figure 4-2, which is due the elongated particles passing through the mesh with their smaller cross section. Table 4-2 shows that 90% of the particle size are within the range of 75 μm .

Sample Name		D(0.1)	D(0.5)	D(0.9)
Al6061 Powder	Diameter (μm)	22.83	41.27	71.92
AlSi10Mg Powder		23.16	39.62	66.55

Table 4-2 The values measured for the particle size distribution of the Al6061 and AlSi10Mg powders.

From the XRD phase pattern in Figure 4-3, lower intensity of Si peaks were observed for Al6061 due to the lower alloying content. Si peaks was high for AlSi10Mg, and shift of Al peak can be observed, indicating a lower solubility of Si in AlSi10Mg [51].

4.2. Microstructure

4.2.1. AlSi10Mg

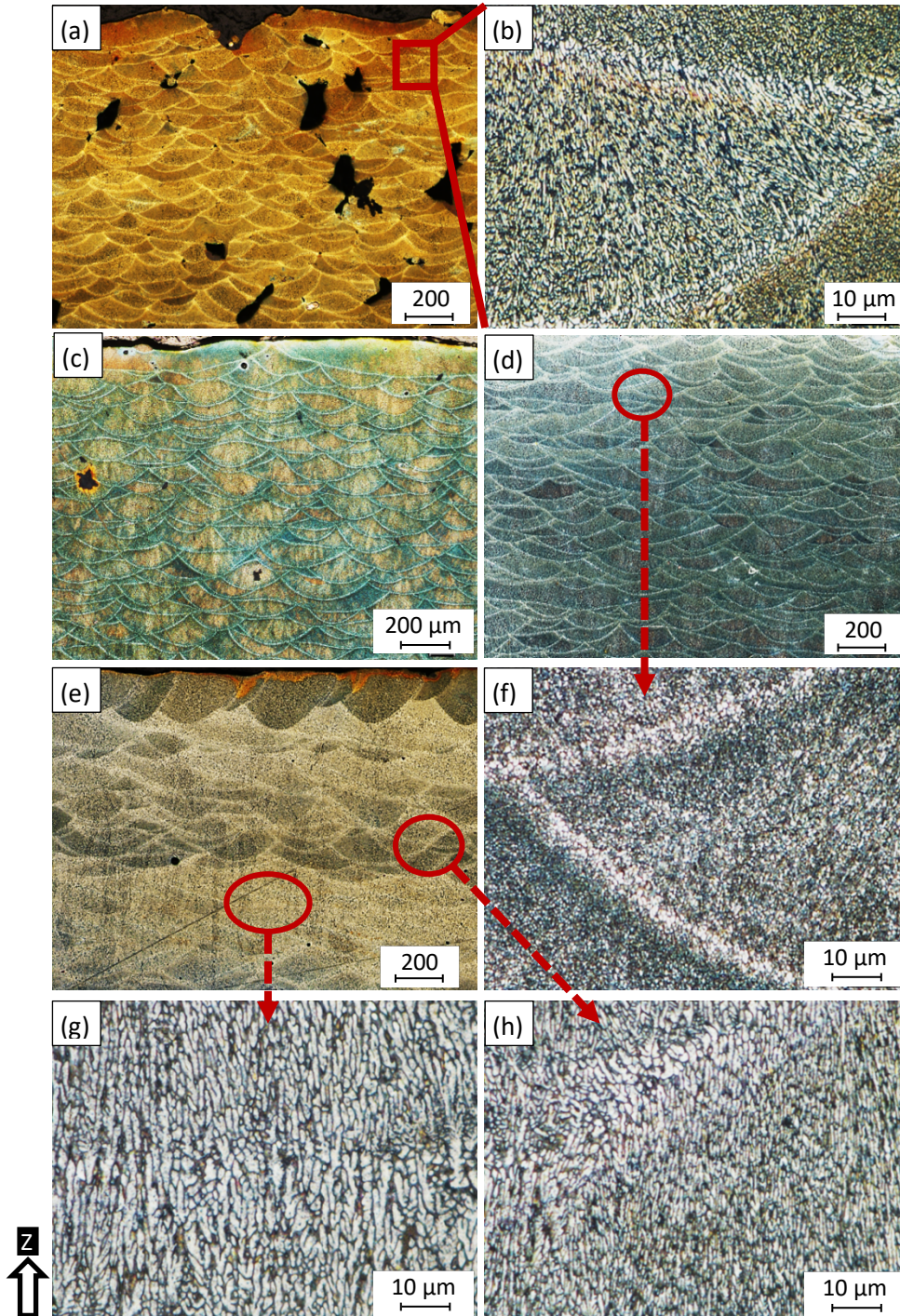


Figure 4-4 Microstructure of the as-built AlSi10Mg_200C samples processed under different SLM process parameters; a, c) AS8, b) AS7, d, f) AS3, e, g, h) AS1.

Selected optical microscope images of etched Al6061 and AlSi10Mg samples were presented in Figure 4-4. Process-induced porosity, or keyholes were observed for sample AS8 in Figure 4-4a, with the size range of 100-250 μm and of irregular shape. AS8 was fabricated with the low energy density of 27J/mm³, thus lack of fusion can be attributed to be the cause. Unmelted powder particles can also be observed within the pores. The elliptical melt pool shape, which was caused by the Gaussian distribution of laser beam power [49] was also evident in Figure 4-4a. From the magnified view (Figure 4-4b), distinctive fine and coarse grains can be observed. Due to the sharp thermal gradient from the melt pool overlaps, fine grains are formed around the borders of the melt pool. Towards the center of the melt pool the thermal gradient is not as sharp, thus larger grains were formed. As the energy density increases to 38J/mm³ (AS7 Figure 4-4c), the severity of the keyhole pores decreases. With further increase in energy density to 50J/mm³ (AS3 Figure 4-4d), keyhole pores diminished. High magnification of the AS3 sample shows that the coarse grain can be found inside the melt pool borders due to an increase in energy density. Further increase in energy density to 65J/mm³ (AS1 Figure 4-4e) results in the melt pool borders dissolving for several layers, as well as the formation of hydrogen pores due to material vaporization from high energy density. This is the result of the reduction in the scan speed and hatch spacing.

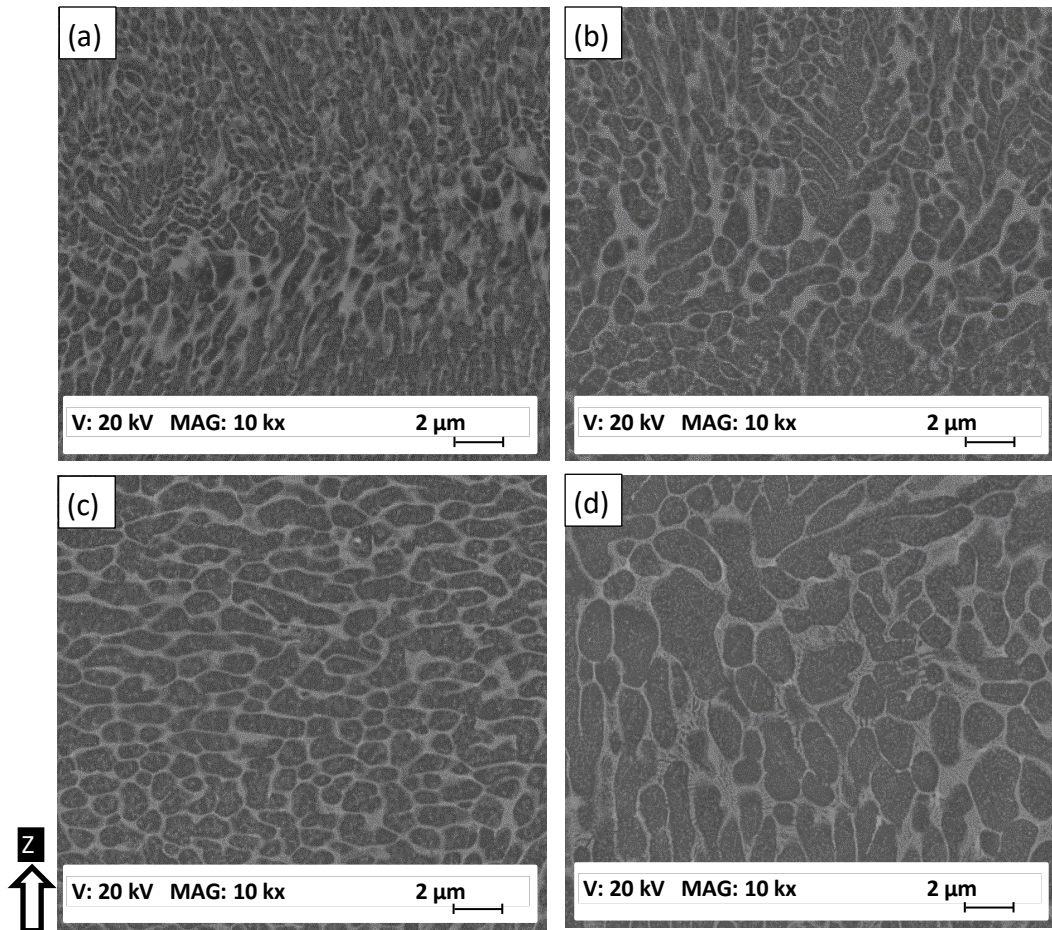


Figure 4-5 The SEM observations of the as-built AlSi10Mg microstructure along Z- direction; a) AS8, b) AS3, c) AS1 near top surface, d) AS1 near the center.

Figure 4-5 shows the SEM images of microstructure change and Al matrix evolution of AlSi10Mg across the range of energy density and SLM process parameters in the Z direction. According to the particle accumulated structure (PAS) mechanism [52], at high cooling rate of 1060 – 1080 C/s, Si is rejected from the Al matrix, thus forming a fibrous Si network around the Al matrix borders. At low energy density of 27J/mm³, ultra-fine elongated grains were observed, with Al matrix of size 0.2μm to 2μm distributed unevenly. Increasing the energy density to 50J/mm³ results in the growth of grain size (0.5μm to 3μm). Further increasing the energy density to 65J/mm³, the Al matrix grain size increases to 3 - 4μm, with a more

homogeneous distribution of microstructure as compare to that of the lower energy densities. All three cases show a finer grain formation around the border of melt pool, and larger grains towards the center of the melt pool. This is due to the thermal gradient and solidification rate differences between the center and the borders of the melt pool.

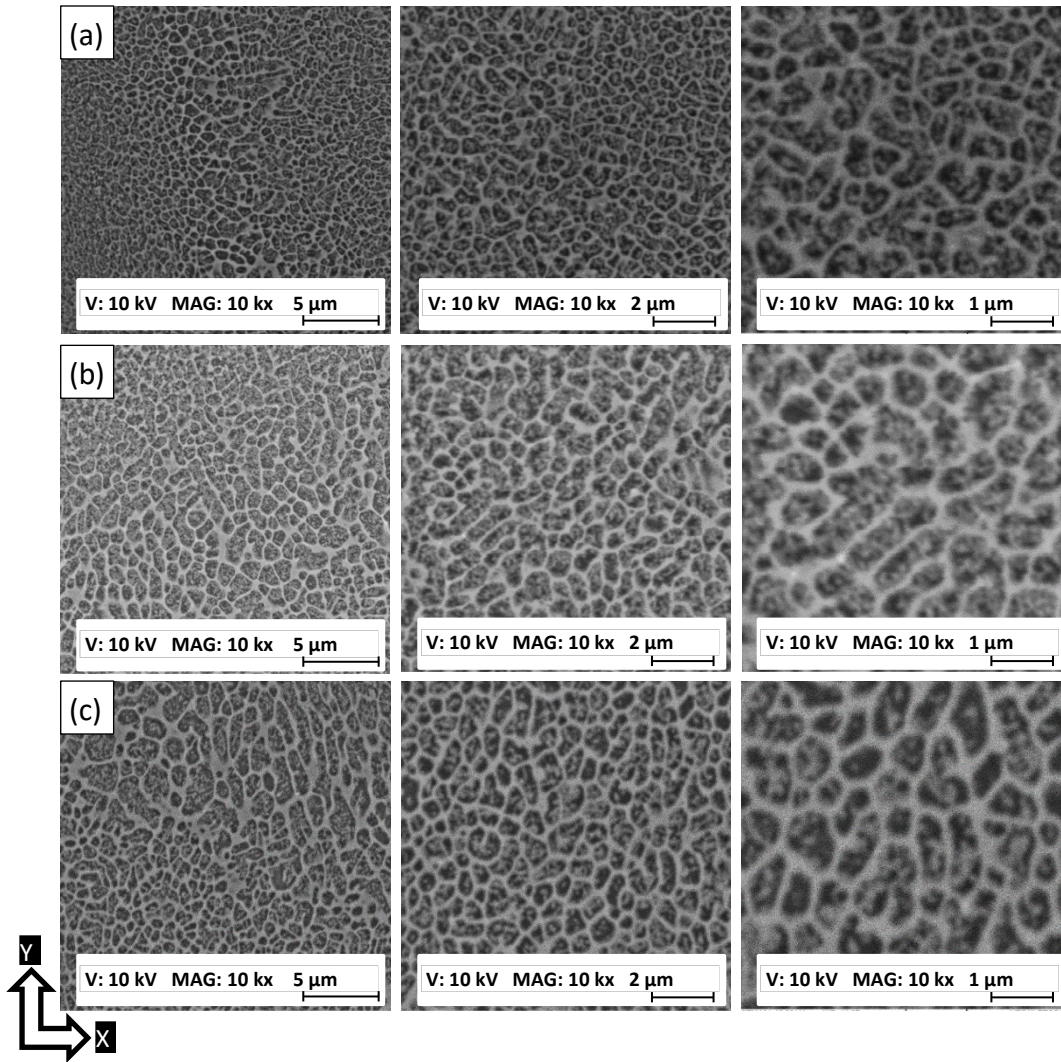


Figure 4-6 SEM observation of AlSi10Mg microstructure along XY plane; a) AS8, b) AS3, and c) AS1.

Figure 4-6 shows the AlSi10Mg microstructure change and Al matrix evolution in the XY plane. The same grain size distribution from Figure 4-5 can be found, where coarser grains are distributed within the melt pool and finer grains towards the border of the melt pool. This along with the observations in Figure 4-5 confirms the PAS formation. Similar observations from

Figure 4-5 on the size of the grains can be made as energy changes. The evolution of the Al matrix grain can then be attributed to the reduction in solidification rate from the increase in the energy density.

To confirm the findings made with Figure 4-5 and Figure 4-6 quantitatively, XRD phase

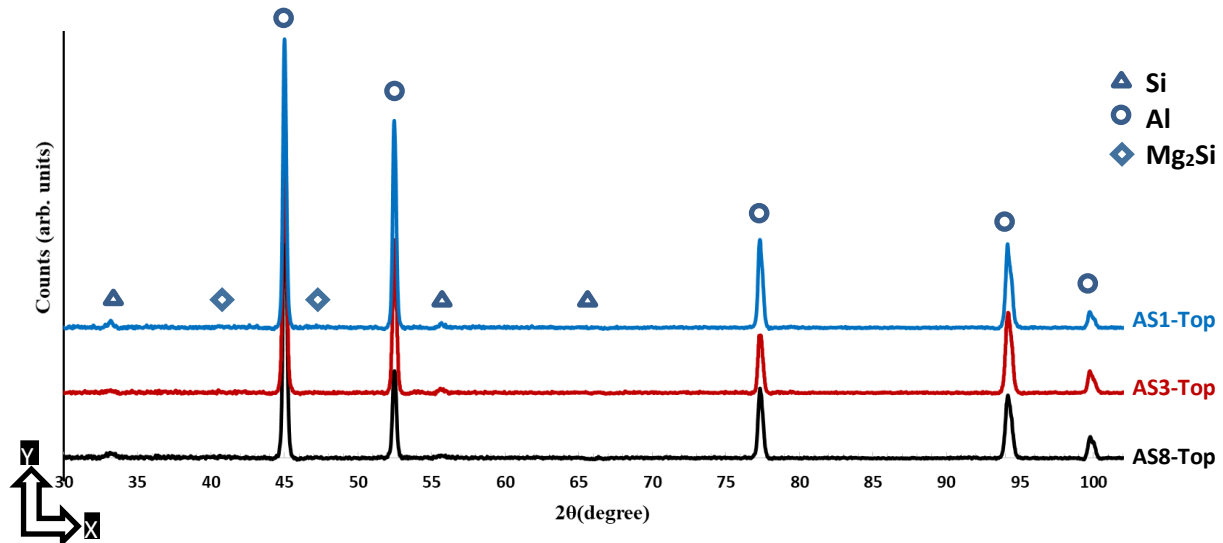


Figure 4-7 XRD phase pattern measured on the top surface (along the XY plane) of different as-built AlSi10Mg samples.

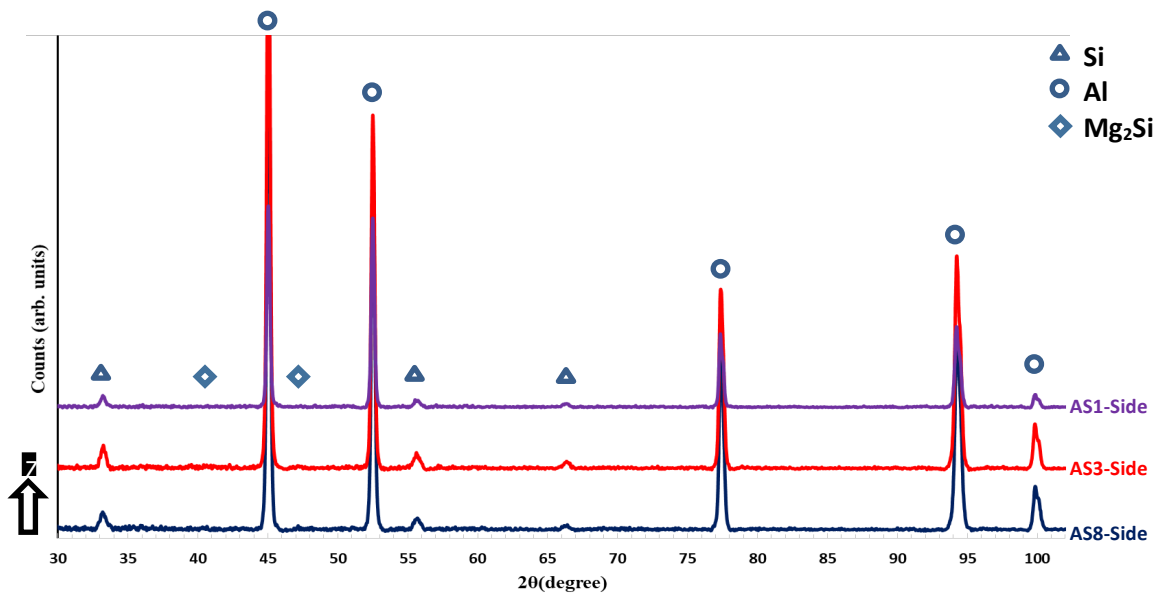


Figure 4-8 XRD phase pattern measured on the side surface (along the Z-direction) of different as-built AlSi10Mg samples.

pattern analysis was conducted, and the phase patterns are presented in Figure 4-7 and Figure 4-8. Al and Si peak were identified using Joint Committee on Powder Diffraction Standards

(JCPDS) patterns of 01-089-2837, 01-089-5012. Mg₂Si peak was identified using the JCPDS pattern 00-001-1192. Crystal size change under difference SLM parameters can be observed as the Al and Si peaks broaden with the change in energy density. The increase in the grain size from energy density increase was confirmed with Figure 4-7 with peak width broadening. Significant peak broadening can be observed in the Z direction, due to the change in crystal shape and size, and potentially macrostrain [53, 54]. This corresponds to the observation from Figure 4-5.

4.2.2. Al6061

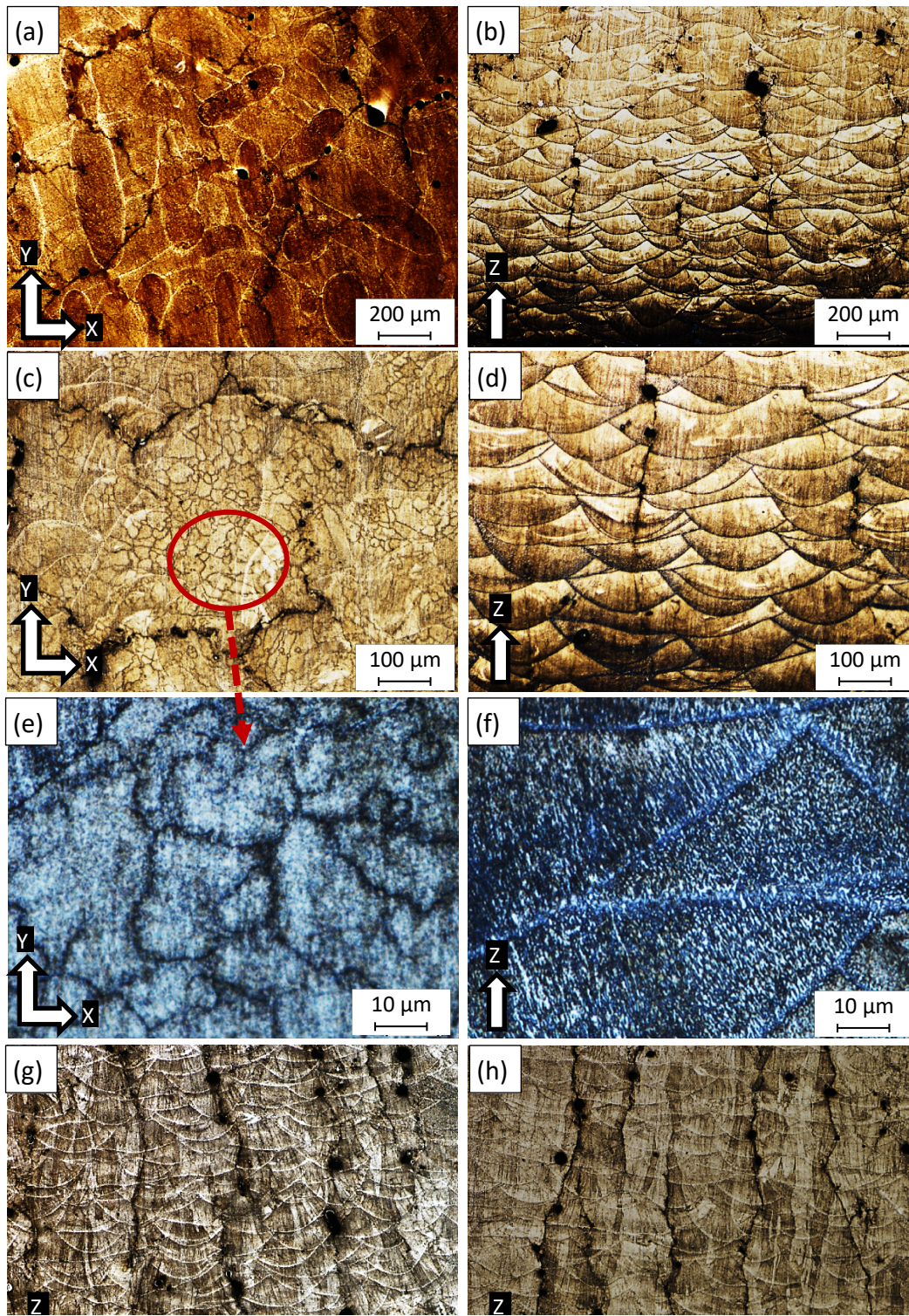


Figure 4-9 Microstructure of the as-built Al6061 samples processed under different SLM process parameters; a,c,e) 6A along the Z-direction , b,d,f) 6A along the XY plane, g) 14A, h) 15A.

Al6061 is well known for hot tearing when undergoing solidification. As seen in Figure 4-9, both the XY plane and the Z direction displayed the formation of hot tearing formed during the solidification cycles. This is due to the chemical composition of the high strength Al alloy, where low amount of alloying element is present, making the alloy hypoeutectic. Hypoeutectic Al alloys go through a range of temperature where mixture between solid and liquid phase are present. During the solidification process, dendritic structures form into elongate grains, and due to the high CTE of Al6061 and the high viscosity of the cooling liquid, voids in between the dendrite arms forms and cannot be filled, resulting hot tearing occurs [29, 39, 55].

The severity of the hot tearing increases with the increase in energy density as comparing the microstructure between Figure 4-9b and Figure 4-9h. This is due to two things: (1) At higher energy density, the likelihood of material vaporization increases, thus more hydrogen pores will be formed, as evident in Figure 4-9g and f. The small pores serve as nucleation sites for crack prorogation. (2) As the laser power increases and the scan speed decreases, an imbalance is created between the melting rate and the solidification rate, where the material experiences faster and frequent melting than solidification, which increases the thermal stress, thus increase the formation of hot tearing.

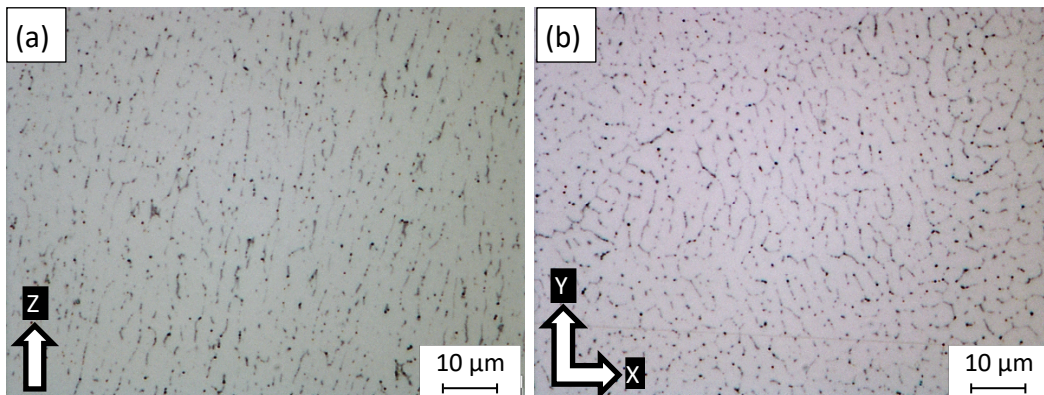


Figure 4-10 Microstructure grains of the as-built Al6061 sample at a higher magnification.

As seen in Figure 4-10, nano-sized Si particles around the Al matrix grains are present, which is in agreement with the PAS formation [56]. Due to the low Si content in Al6061, no fibrous Si network was formed. Comparing the grain morphology between Figure 4-10a and Figure 4-10b, elongated grains of size 3-5 μm were observed along the Z direction, whereas for the XY plane,

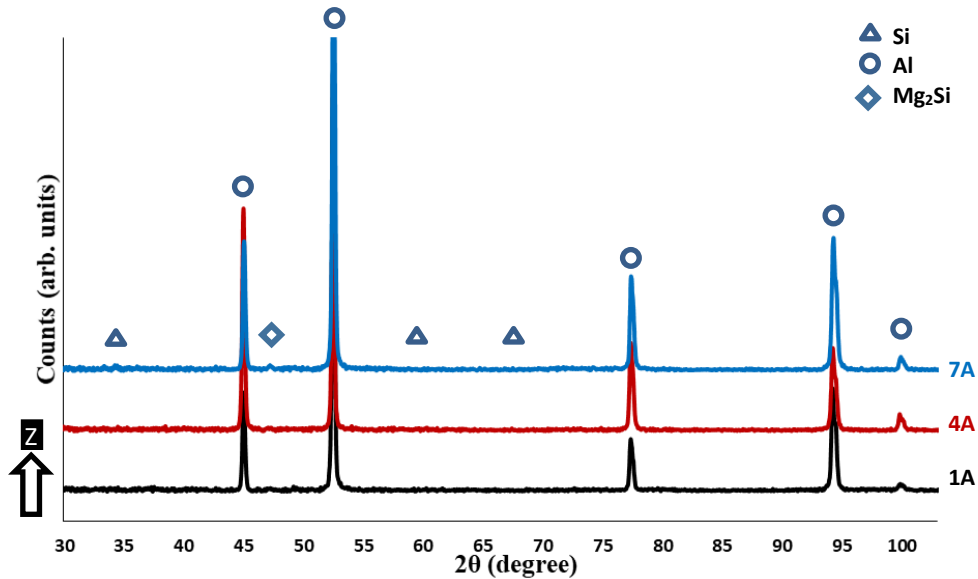


Figure 4-11 XRD phase pattern measured on the side surface (along the Z-direction) of different as-built Al6061 samples.

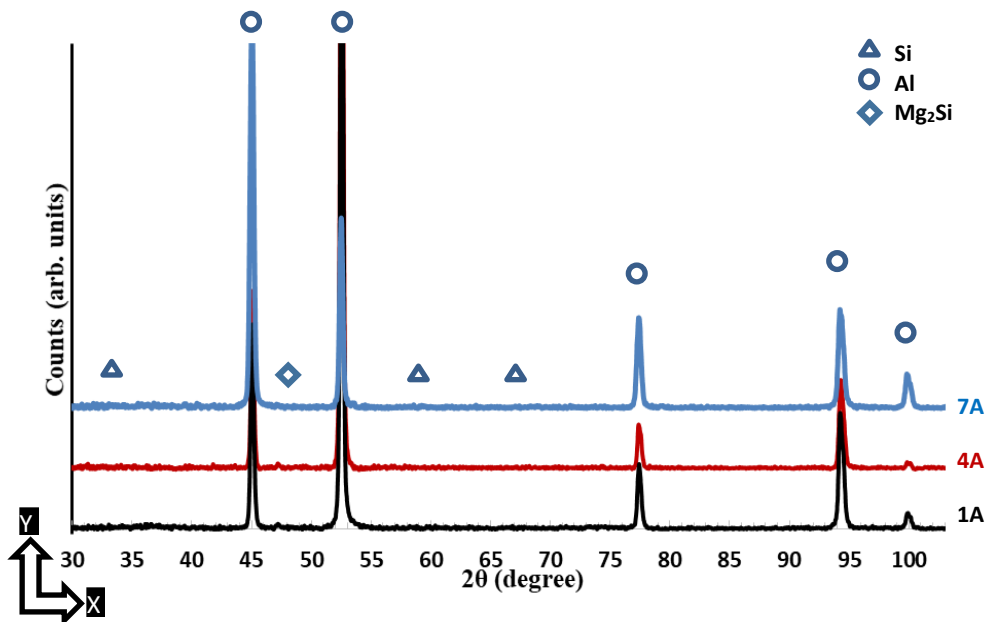


Figure 4-12 XRD phase pattern measured on the top surface (along the XY plane) of different as-built AlSi10Mg samples.

equiaxed grains of 2-4 μm were found. This reveals the inhomogeneity between build directions, which could result in anisotropy.

To confirm the observation made from Figure 4-9 and Figure 4-10, XRD phase pattern analysis as made, Figure 4-11 and Figure 4-12. JCPDS pattern 01-089-2837 was used to identify the Al peaks, and JCPDS pattern 01-089-5012 was used for the Si peaks. Due to the presence of the nano-size Si particles, the Si peaks are hardly detectable. A change in Al peak broadening was detected when comparing between the XY plane (Figure 4-12) and Z direction (Figure 4-11), an indication of Al crystal size change. This change is also present amongst the samples, which confirms the visual observation of grain coarsening with increased energy density as well as change in build direction. This broadening however, is not as severe as that of the AlSi10Mg, which means the microstructure of Al6061 produced via SLM is more homogeneous.

4.3. Mechanical Properties

4.3.1. Microhardness

4.3.1.1. *AlSi10Mg*

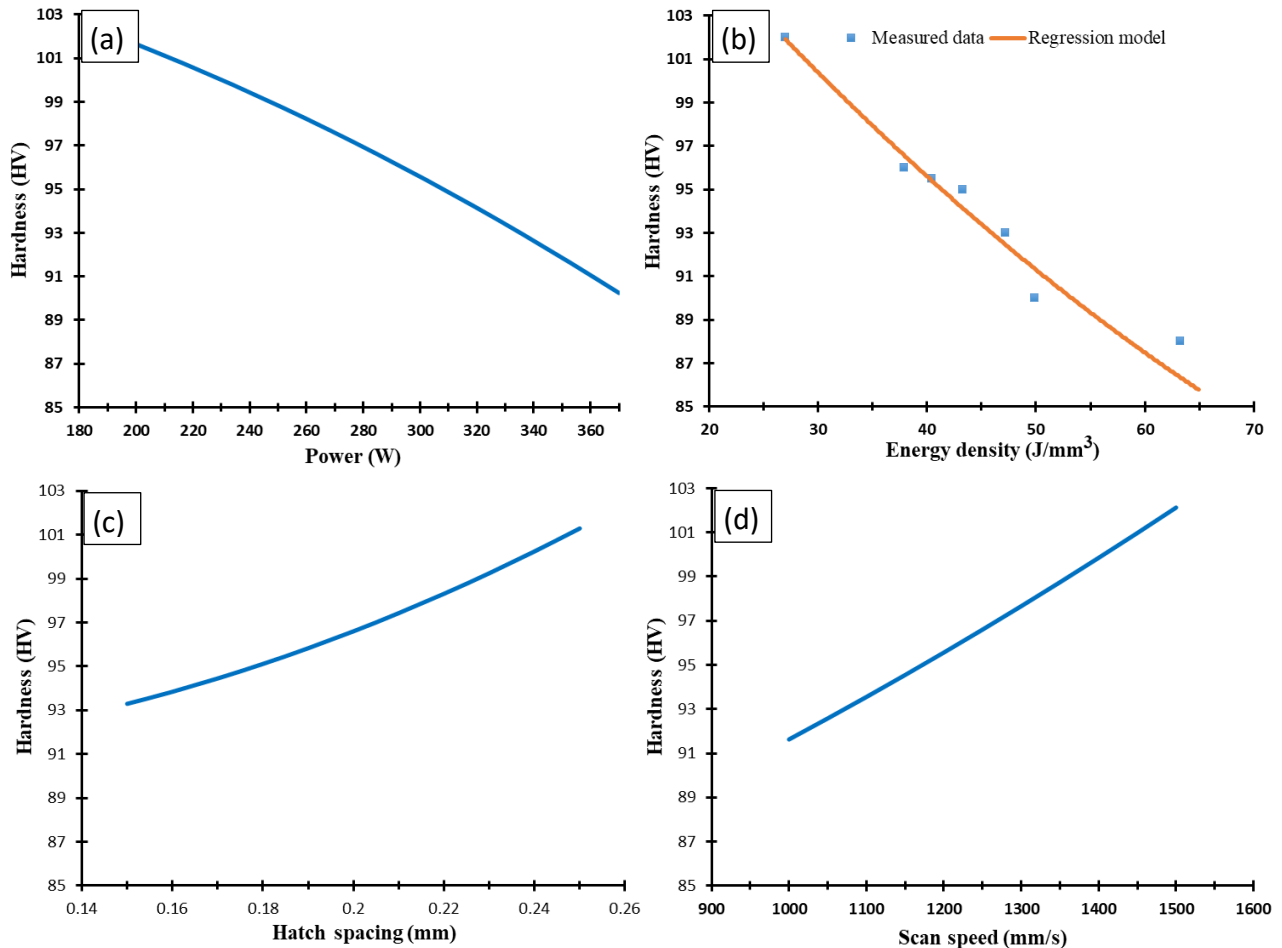


Figure 4-13 Effect of the SLM process parameters on microhardness of the as-built *AlSi10Mg* samples along the Z-direction.

The microhardness for *AlSi10Mg* is displayed in Figure 4-13 for the Z direction build orientation. As observed in Figure 4-4, at lower energy density (27J/mm^3), smaller grain structures were formed, thus increases the hardness. Maximum hardness was observed to be 103Hv at 27J/mm^3 , however, as the process parameter varies across range, the hardness drops to 86Hv . As seen in Figure 4-13b, the decrease in hardness follows linearly to the increase in energy density. And from Figure 4-13c and d, the increase in laser path overlap and the low

solidification rate from low hatch spacing and low scan speed, results in the decrease in the hardness [29], [47].

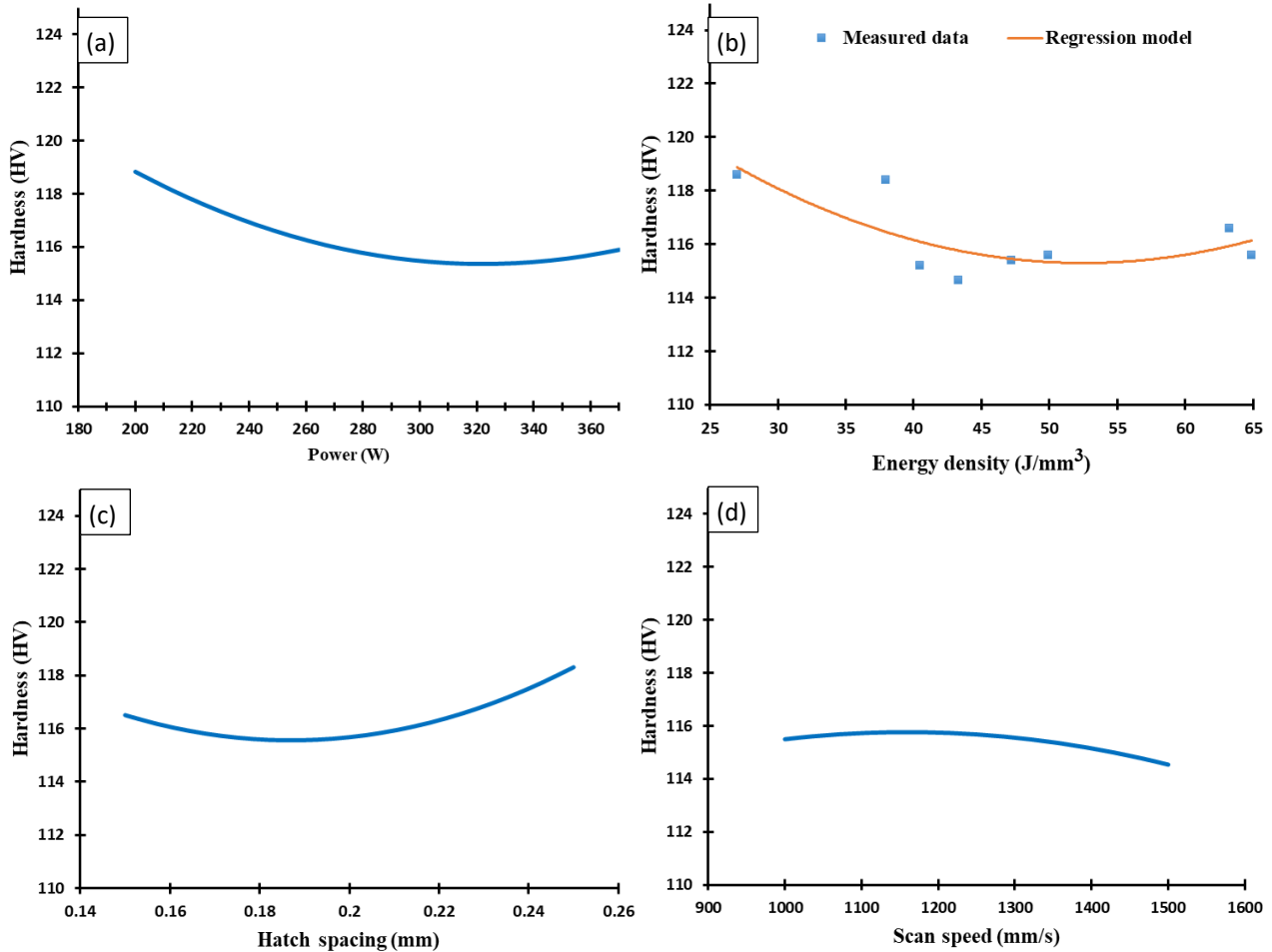


Figure 4-14 Effect of the SLM process parameters on microhardness of the as-built AlSi10Mg samples along the XY plane.

As seen previously in Figure 4-5, the microstructure on the XY plane of AlSi10Mg exhibits a more homogenous and stable grain structure compared to that of the Z direction orientation. As seen in Figure 4-14, 115 to 118Hv was observed in the XY plane, which is higher than that of the Z directions, further indication of anisotropy. The range of hardness value is lower in the XY plane, which indicates better homogeneity, and is in agreement with literature [49], [52], [48].

4.3.1.2. Al6061

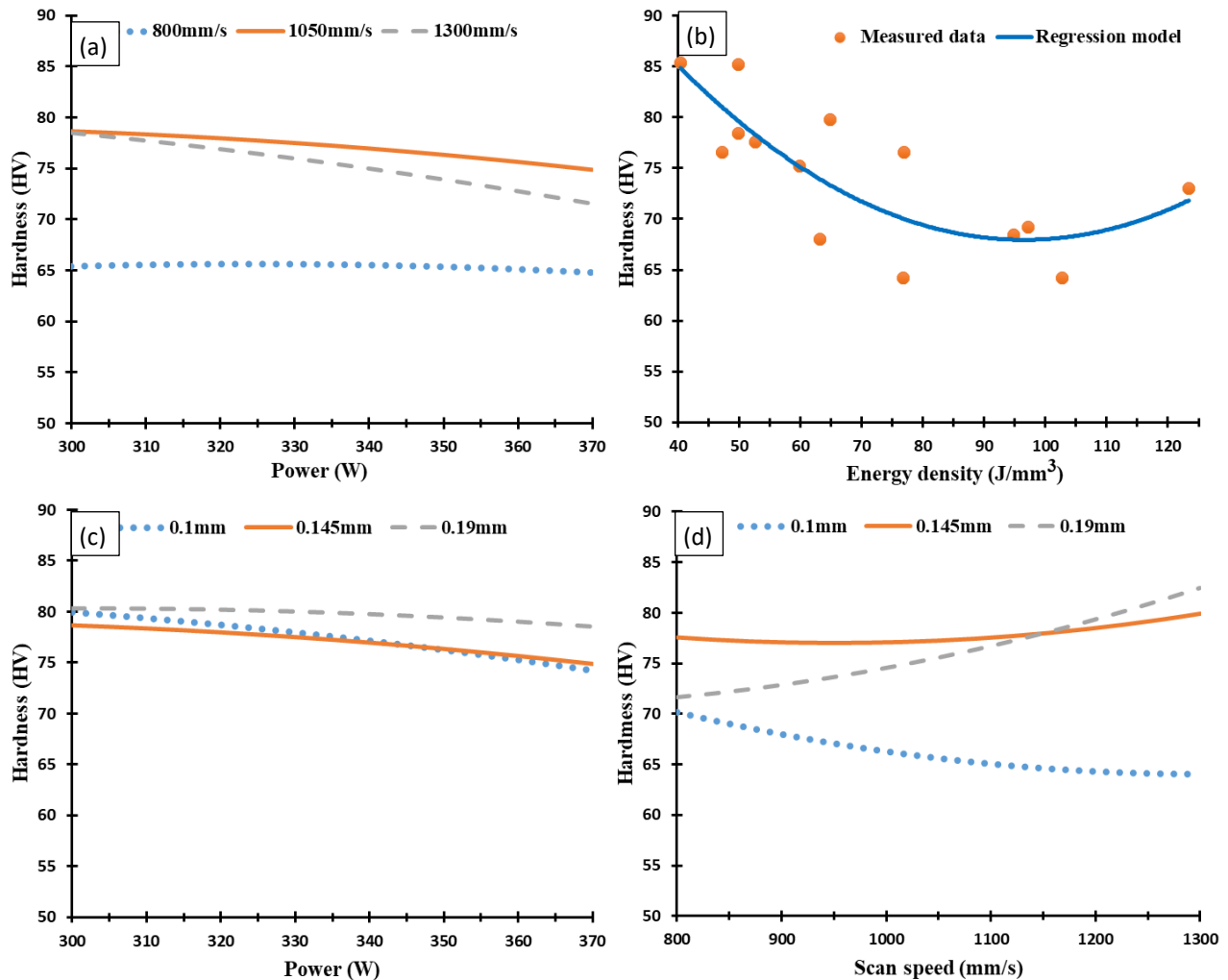


Figure 4-15 Effect of the SLM process parameters on microhardness of the as-built Al6061 samples along the building direction.

The microhardness along the build direction for Al6061 was presented in Figure 4-15. The microhardness for Al6061 can be seen a more robust to the change in SLM process parameters when comparing to the AlSi10Mg. The hardness follows a parabolic curve in relation with energy density, with the maximum hardness of 85Hv at low energy density of 40.5J/mm³ and minimum of 72Hv at 97.2J/mm³. The higher solidification rate associated with the increase in scan speed showed an increase in microhardness. From the intersection of the curves on each graph, significant interaction can be observed between laser power and scan

speed. Interaction between scan speed and hatch spacing can also be observed. Further indication of solidification rate and melting rate to be the mechanism effecting the hardness.

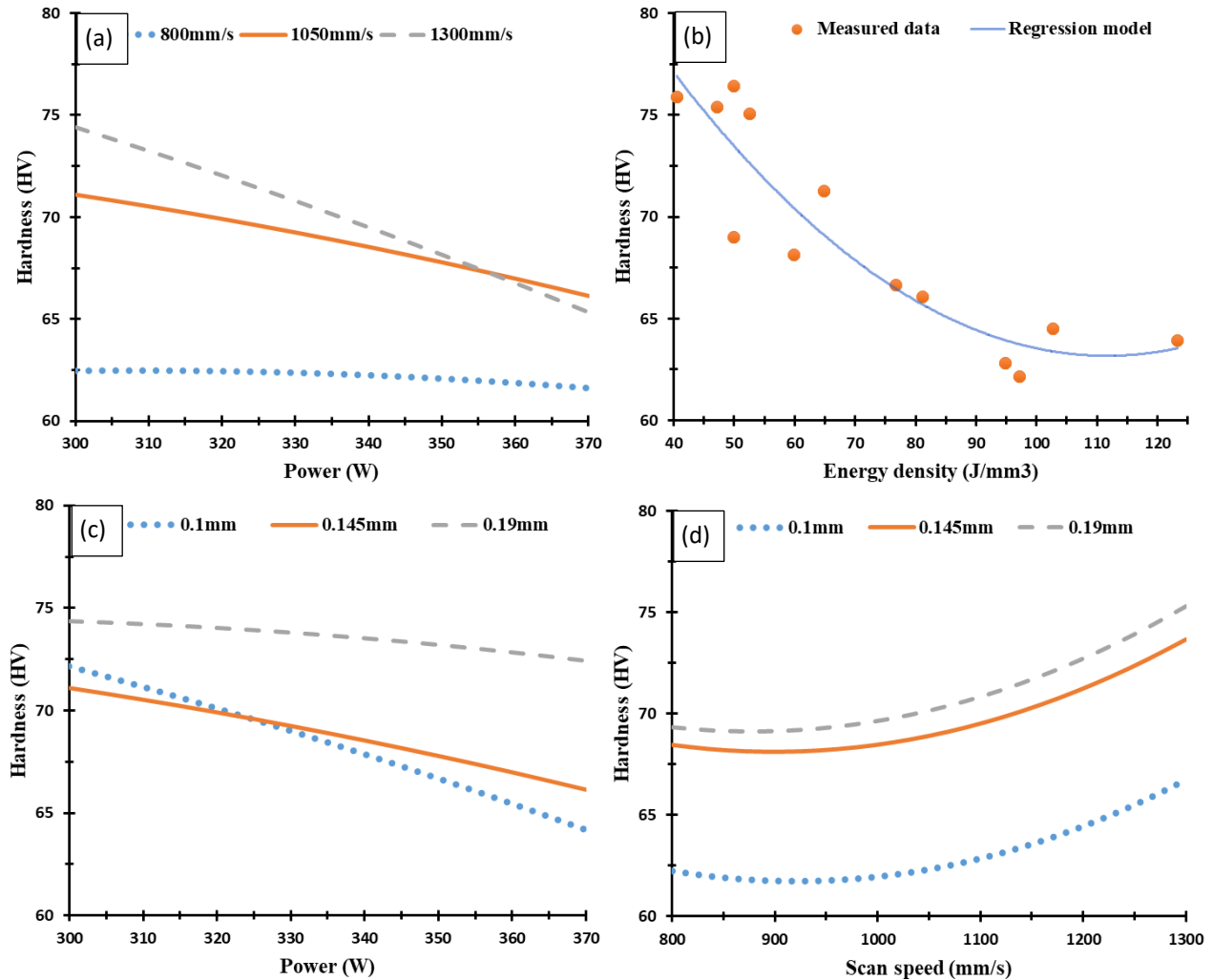


Figure 4-16 Effect of the SLM process parameters on microhardness of the as-built Al6061 samples along the XY plane.

The microhardness for Al6061 in the XY plane is presented in Figure 4-16. Similar observation previously can be made here, as the increase in laser power reduces the hardness due to increasing the solidification rate, which results in grain coarsening [52]. The microhardness decreases gradually with an increase of energy density due to the gradient in microstructure formation, which is in agreement with the results found in literature [57], [52].

In general, AlSi10Mg displayed a significantly higher hardness than Al6061 due to the higher precipitate of Si particles.

4.3.2. Tensile behaviour

4.3.2.1. *AlSi10Mg*

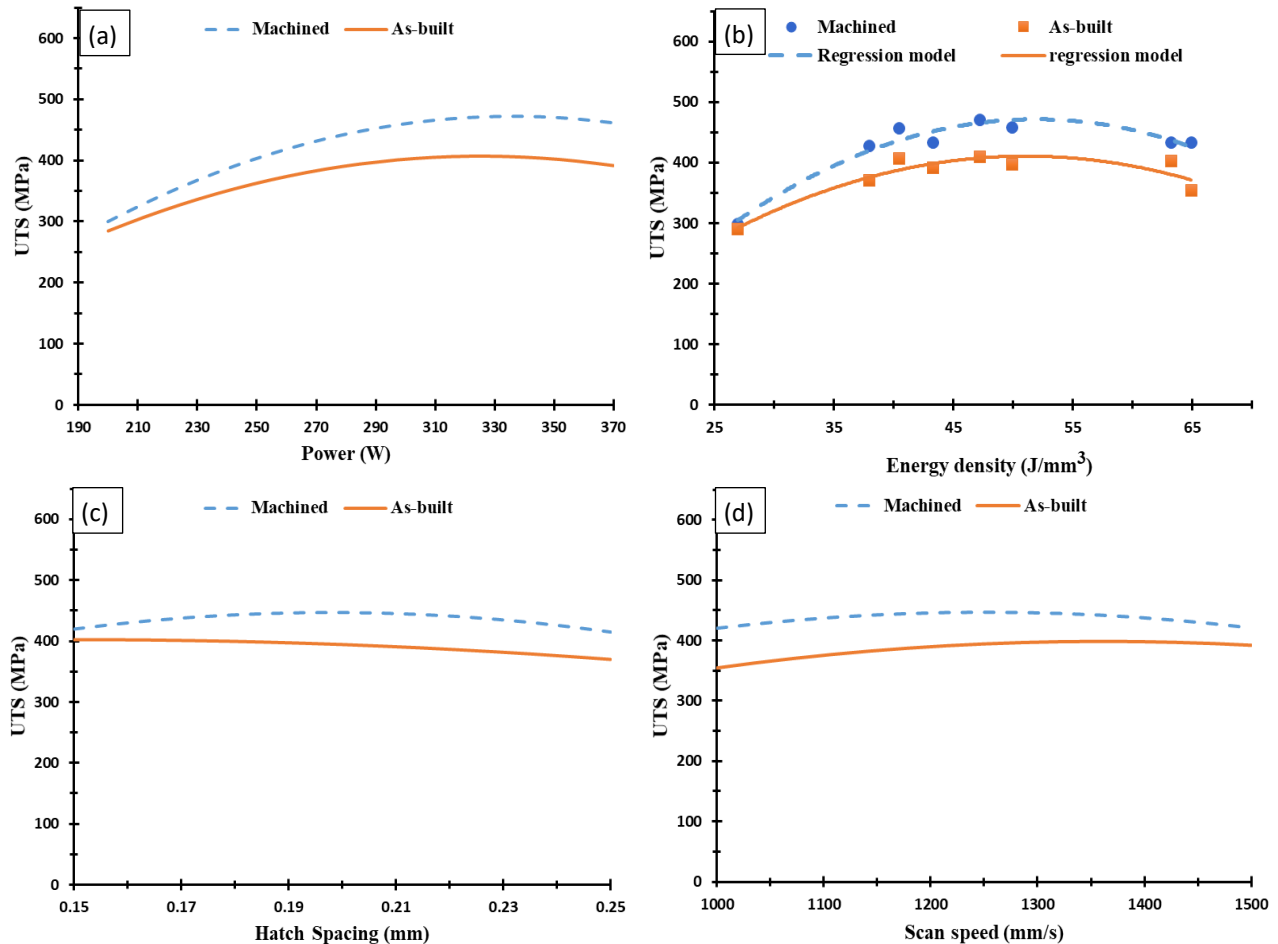


Figure 4-17 Effect of the SLM process parameters on ultimate tensile strength of the as-built AlSi10Mg samples along the building direction.

Ultimate tensile strength (UTS) of the as-build and machined AlSi10Mg samples are presented in Figure 4-17. Same profile of curve can be observed in all four relationships for the as-build and machined samples, however higher UTS was obtained with the samples that had gone through surface polish (450MPa vs. 400MPa of as-build sample). This indicates the surface roughness effect on the mechanical properties of parts as discussed in chapter 2.3. The effect of laser power on UTS is also more significant comparing to scan speed and Hatch spacing. At

50J/mm³, maximum UTS for as-build samples were obtained, which corresponds to the fine microstructure and minimal internal defects observation made in Figure 4-4.

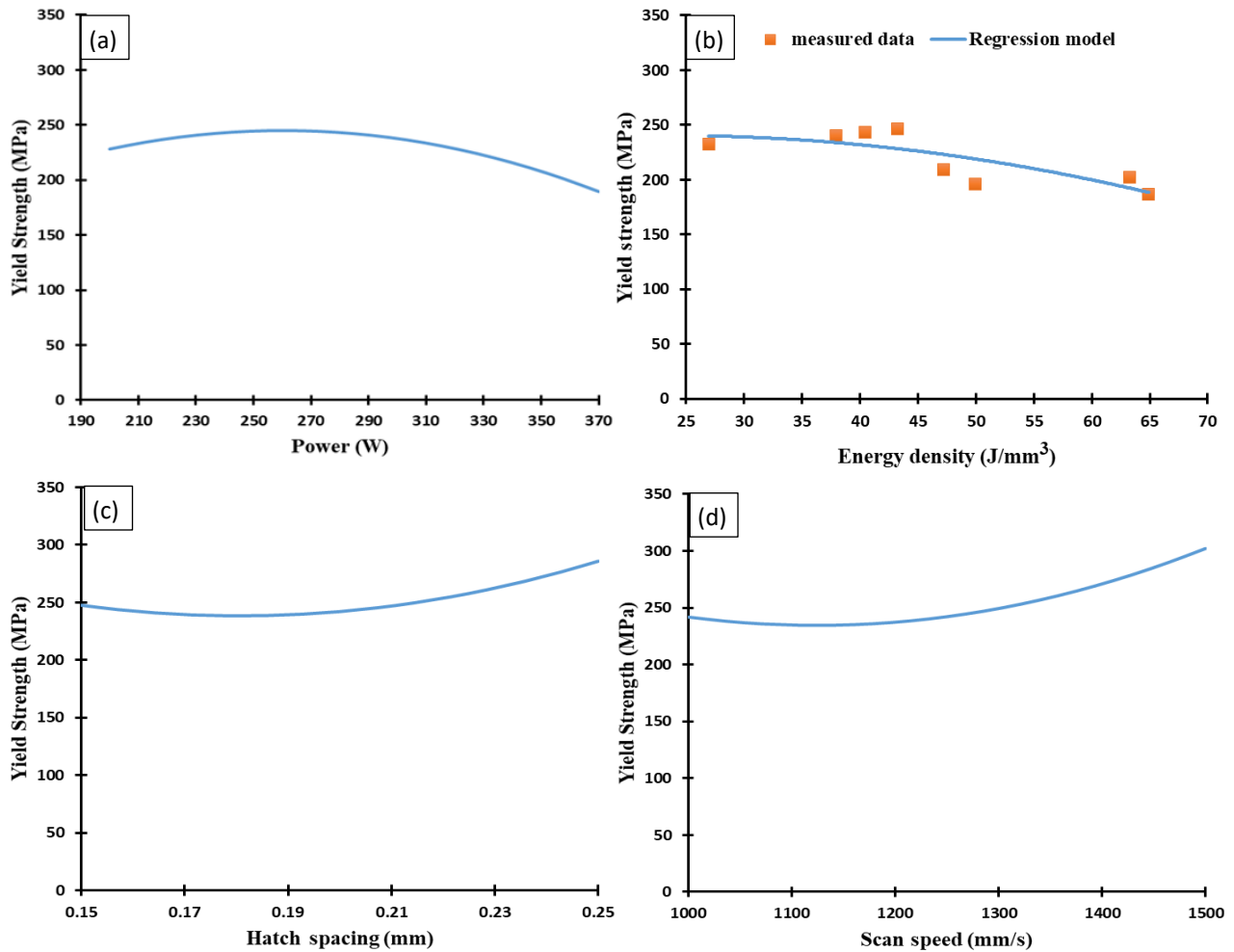


Figure 4-18 Effect of the SLM process parameters on yield strength of the as-built AISi10Mg samples.

The yield strength of as-build AISi10Mg increases with the decrease of energy density, 190MPa to 240MPa as seen in Figure 4-18. Range of variability in yield strength lowers comparing to that of the UTS, indicating that SLM process parameters had greater impact on UTS. The effect of microstructure coarsening due to increasing in energy density, as observed in Figure 4-5, can be observed in the decrease of UTS and yield strength.

4.3.2.2. Al6061

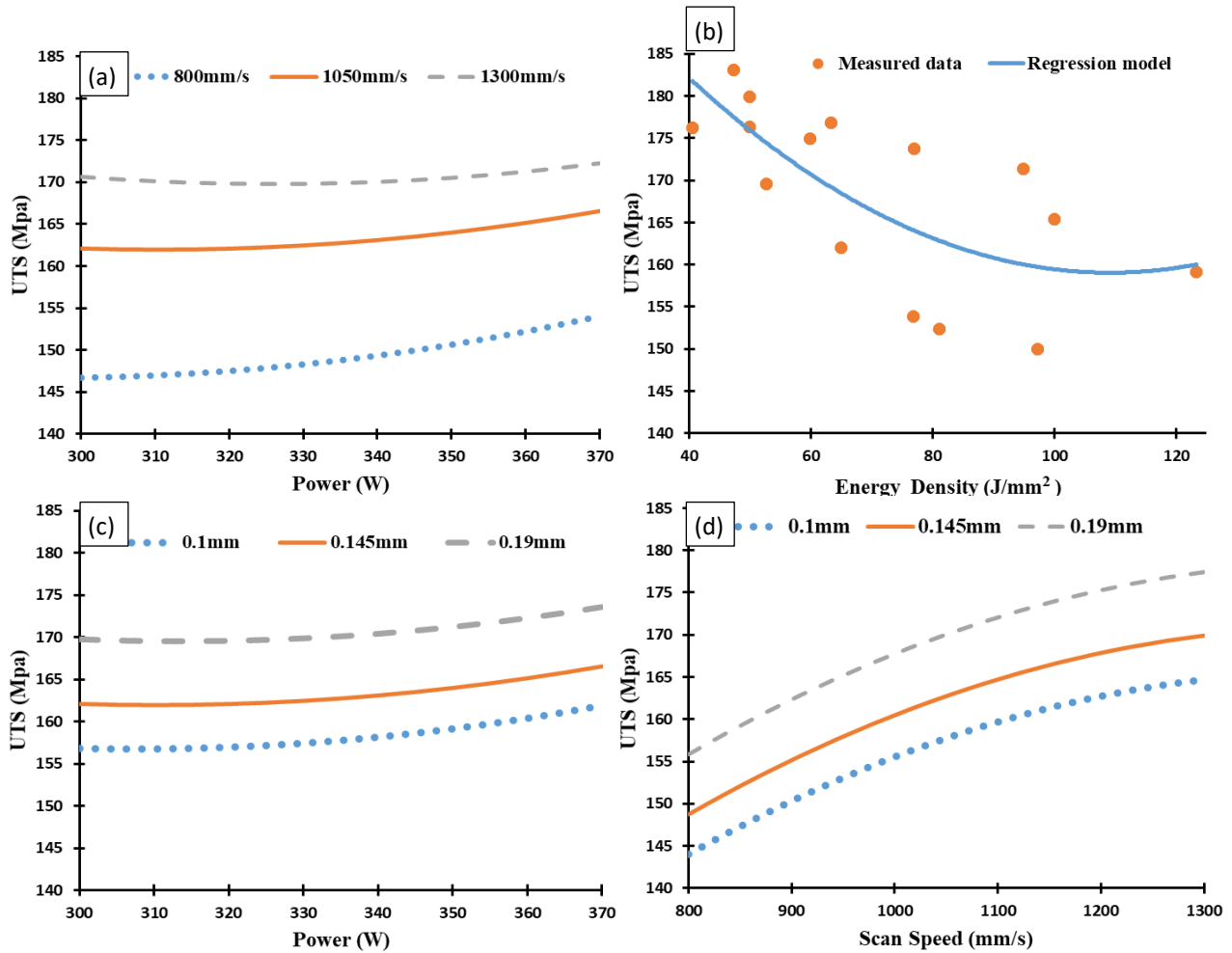


Figure 4-19 Effect of the SLM process parameters on ultimate tensile strength of the as-built Al6061 samples along the building direction.

The as-build UTS for Al6061 is presented in Figure 4-19. Inhomogeneity of mechanical due to the formation of cracks can be observed when comparing UTS to energy density, with high scattering of data. Lower UTS was obtained with Al6061 when comparing to AlSi10Mg (184MPa vs. 400MPa), due to the combination of lower percentage of Si content as well as the presence of internal cracks. With all curves on all three interaction plots showing near parallel pattern, thus indicating that there are minimal interaction effects between the process parameter for the UTS behaviour of Al6061.

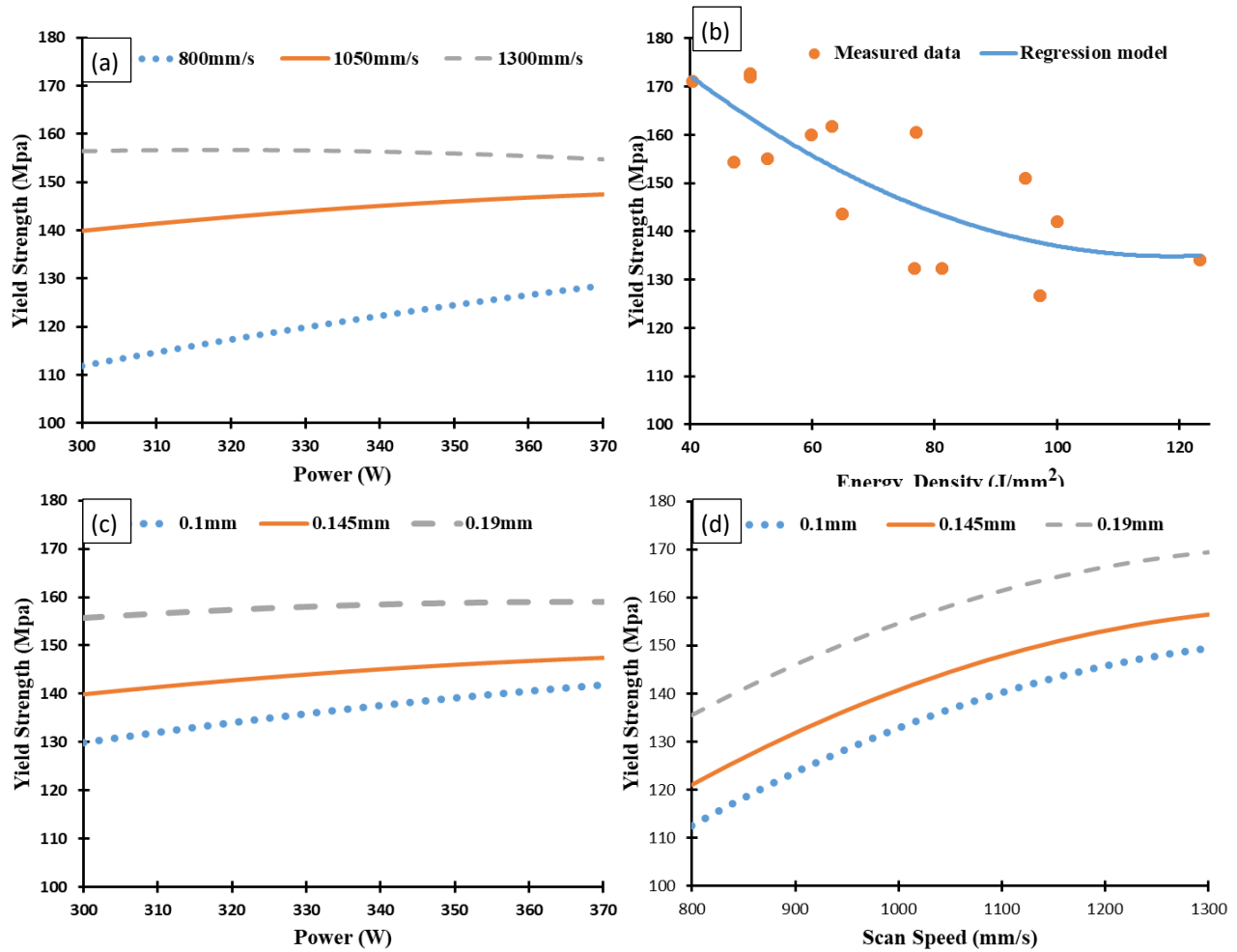


Figure 4-20 Effect of the SLM process parameters on yield strength of the as-built Al6061 samples.

Yield strength for the as-built Al6061, as displayed in Figure 4-20, showed interaction between laser power with scan speed, and laser power with hatch spacing. The combination of decreasing laser power and increasing scan speed increases the yield strength to the maximum of 172MPa. Comparing to the UTS in Figure 4-19, no significant difference can be made between the UTS and the yield strength of Al6061, indicating it had a lower ductility comparing to AlSi10Mg.

4.4. Physical Properties

4.4.1. Density

4.4.1.1. *AlSi10Mg*

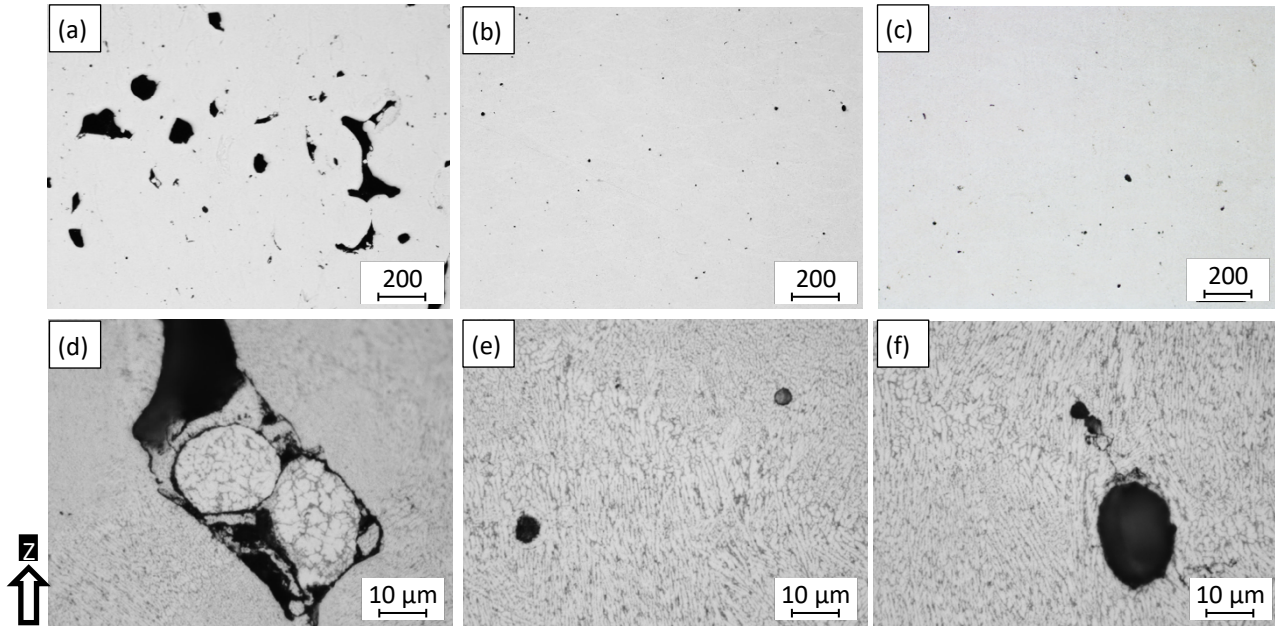


Figure 4-21 Pores observed inside the as-built *AlSi10Mg* sample fabricated at different SLM parameters; a, d) AS8, b, e) AS3, c) AS1.

Energy density have a significant effect on the relative density of the as-build *AlSi10Mg* part, as seen in Figure 4-21 and Figure 4-4. At low energy density, insufficient melting occurs, forming keyhole pores within the layer boundaries up to the size of $200\mu\text{m}$. The pores improve at $50\text{J}/\text{mm}^3$ energy density but worsens as energy density kept increasing to $65\text{J}/\text{mm}^3$ due to the formation of hydrogen pores.

This observation of the porosity is validated by the measurement in the relative density of the as-build and polished *AlSi10Mg* parts in Figure 4-22. High relative density of 99.7% can be achieved with energy density of 50 to $60\text{J}/\text{mm}^3$. The polished samples are observed to have a higher relative density (0.1% - 1%) compared to the as-build samples, indicating that significant

amount of porosity existed just below the surface of the parts. Laser power is seen to have the most significant effect on the part density.

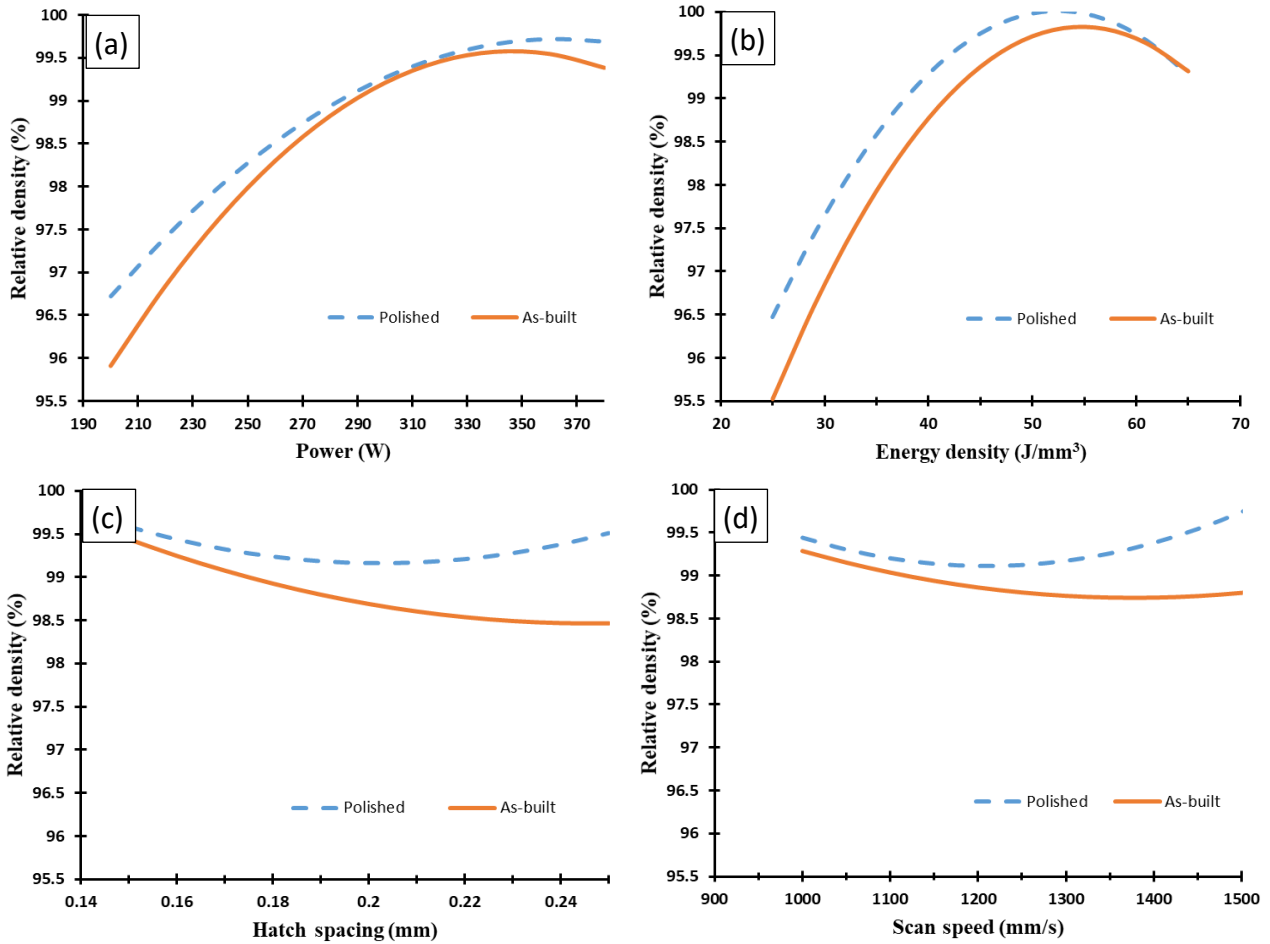


Figure 4-22 Influence of the SLM process parameters on relative density of the as-built AISi10Mg samples.

4.4.1.2. Al6061

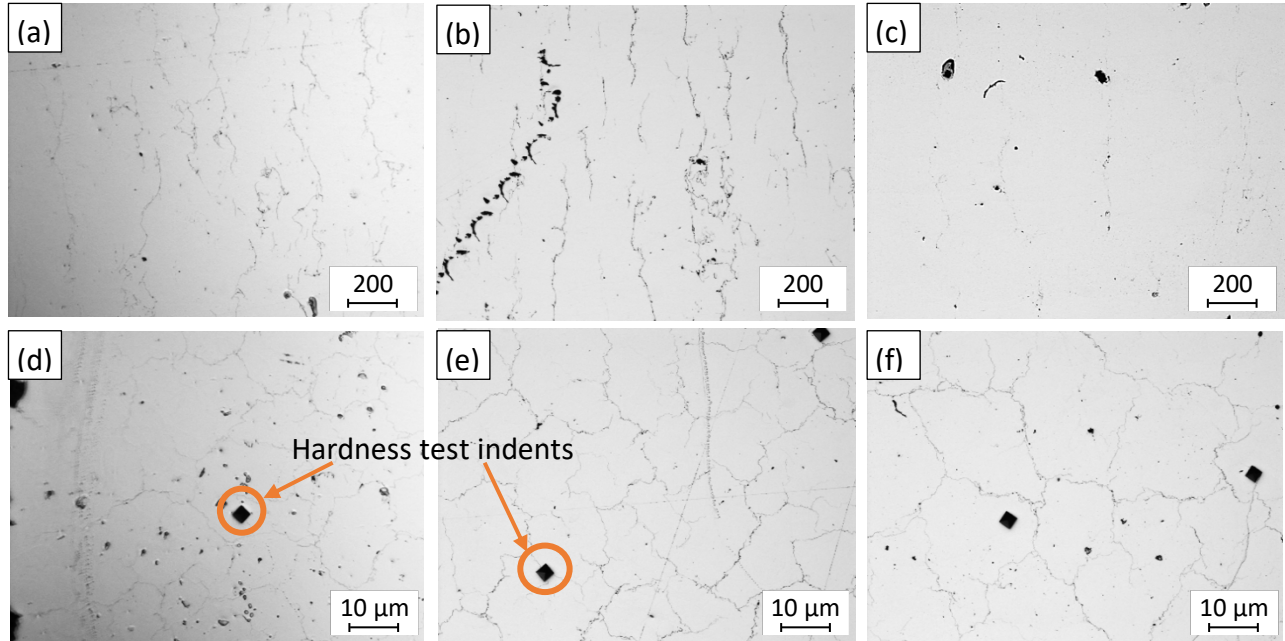


Figure 4-23 Pores observed inside the as-built Al6061 samples processed through different SLM parameters; a, d) 8A, b, e) 4A, c) 1A.

In Figure 4-23, the micro crack formation on the polished Al6061 samples can be observed. Lower porosity and lower number of keyholes are present compared to AlSi10Mg samples. However, due to hot cracking, Al6061 samples exhibit a lower relative density compared to AlSi10Mg. The severity of the cracks is relatively the same across range of the SLM energy density, which is in agreement with the finding from Debroy et al. [6]. The formation of the cracks is observed to be related to the scan speed with a low scan speed of 800mm/s producing the least amount of crack comparing to 1300mm/s. The scan speed is in direct relation with the solidification rate, and this effect is further confirmed with the relative density curves in Figure 4-24. Significant interaction can be observed between laser power and scan speed.

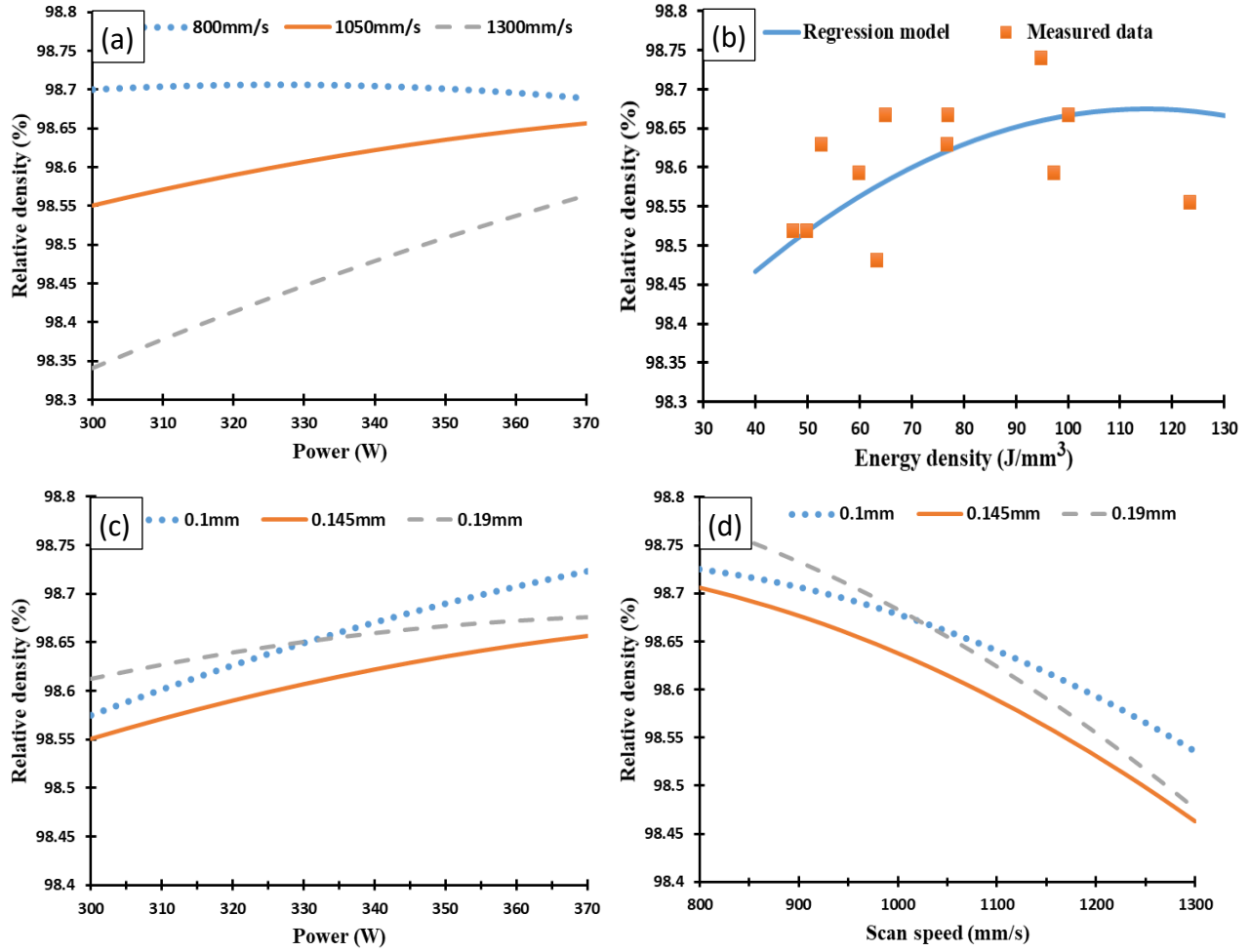


Figure 4-24 The SLM process parameters effect on relative density of the as-built Al6061 samples.

4.4.2. Surface roughness

4.4.2.1. *AlSi10Mg*

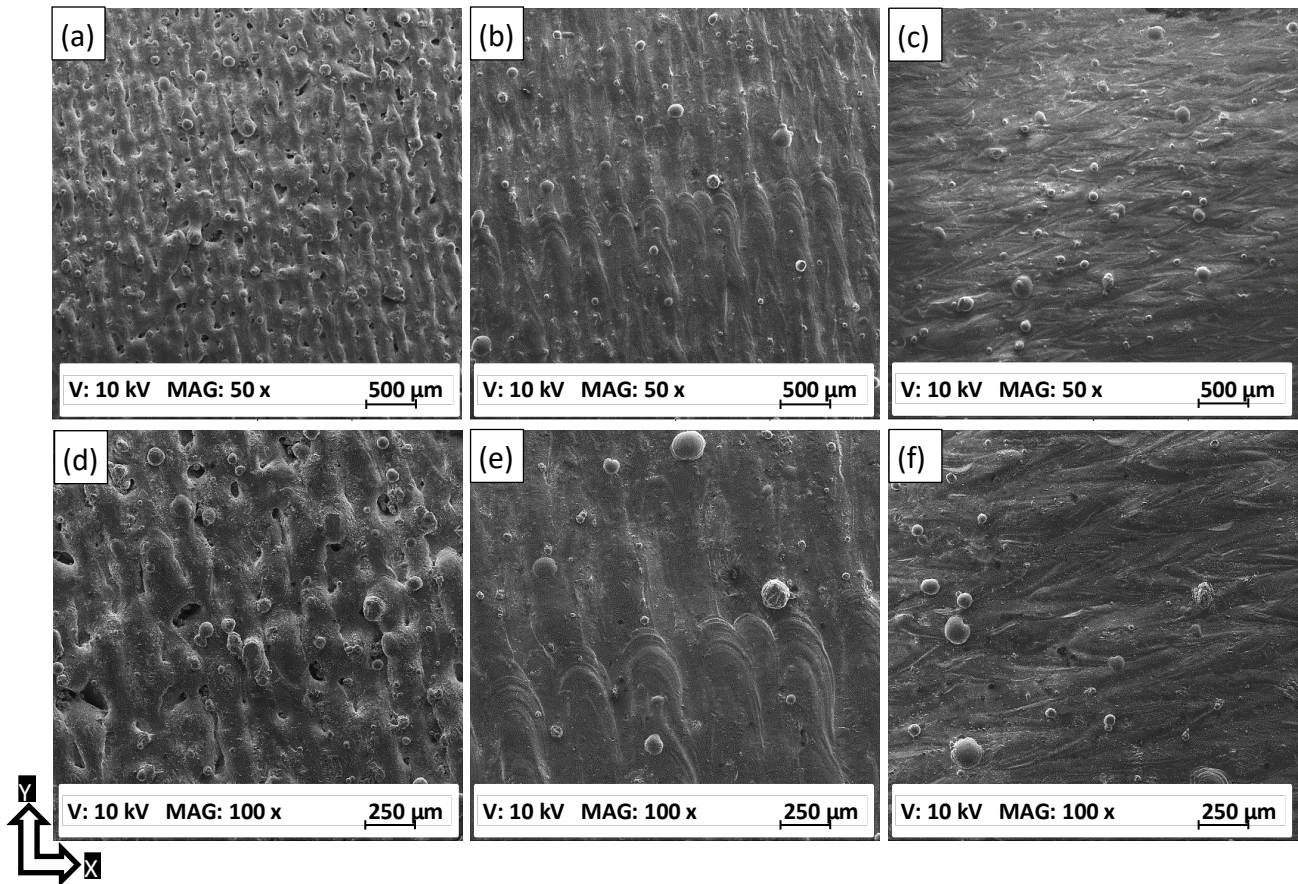


Figure 4-25 The SEM observations on the as-built surface of *AlSi10Mg* samples; a) AS8, b) AS3, c) AS1.

Surface defects for *AlSi10Mg* samples can be observed in Figure 4-25. Rough surface can be seen with low energy density due to large hatch spacing and insufficient melting power, which results in the noticeable melt pool track, as well as porosities from balling effect. Similar to the observations made with relative densities, the surface roughness decreases as the energy density increases until the formation of hydrogen pores due to excessive laser energy.

As seen in Figure 4-26, 3D surface texture revealed the same observation made above, where surface roughness of 15μm was obtained at low energy density, 27J/mm³. Surface roughness reaches optimal at 65J/mm³ of 4.5μm. This trend can be best described in Figure

4-27, where laser power is shown to have significant effect on the surface roughness. Increasing hatch spacing and scan speed, both reduce the surface roughness due to the decrease in melt track overlap, thus the melt pool tracks are more distinguishable, making the surface rougher [58].

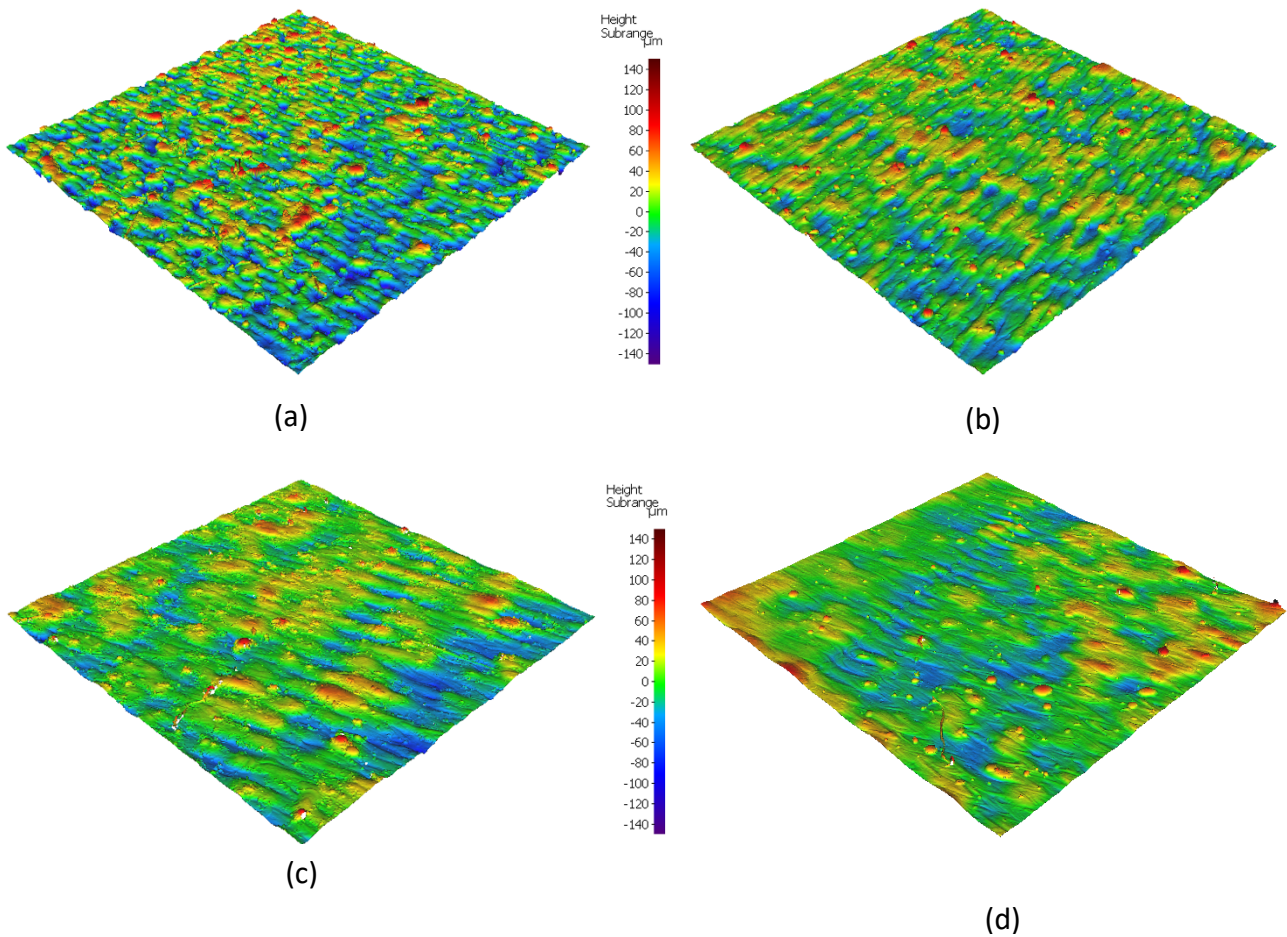


Figure 4-26 The 3D surface texture of the as-built AlSi10Mg samples; a) AS8, b) AS6, c) AS3, d) AS1.

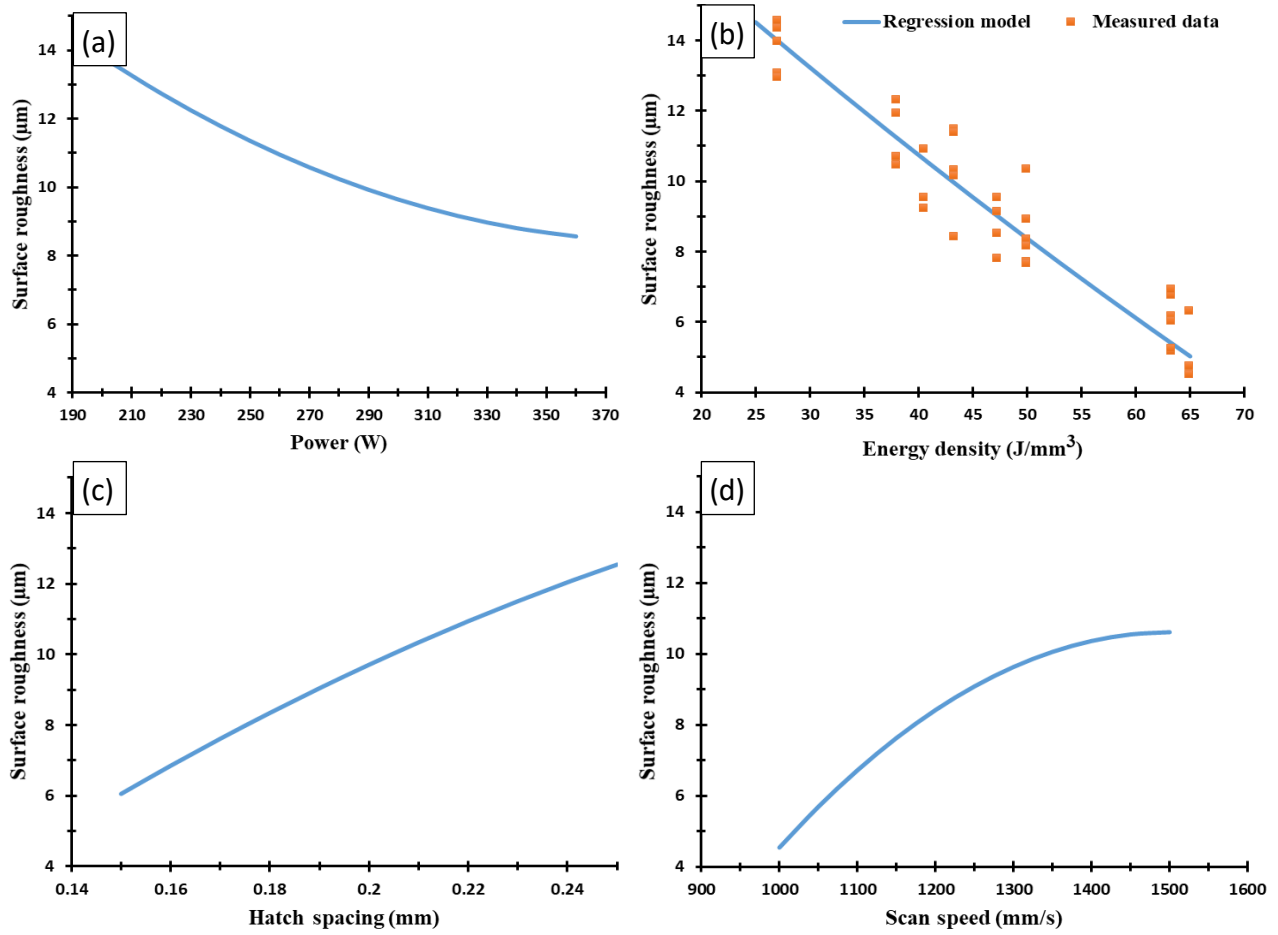


Figure 4-27 Effect of the SLM process parameters on surface roughness of the as-built AlSi10Mg samples.

4.4.2.2. Al6061

The as-built surface of Al6061, as seen in Figure 4-28 and Figure 4-29, exhibit significantly more defects compare to that of the AlSi10Mg. With more satellite powder adhesion to the surface, surface porosities, and coarse melt pool tracks. Similar to AlSi10Mg, the surface roughness of Al6061 improves with increase in energy density, which was confirmed with the 3D surface texture in Figure 4-29. However hot tearing occurs regardless of the energy density. It can also be observed in Figure 4-28, that the cracks formations are generally concentrated at the end of the melt track, where high thermal gradients occur.

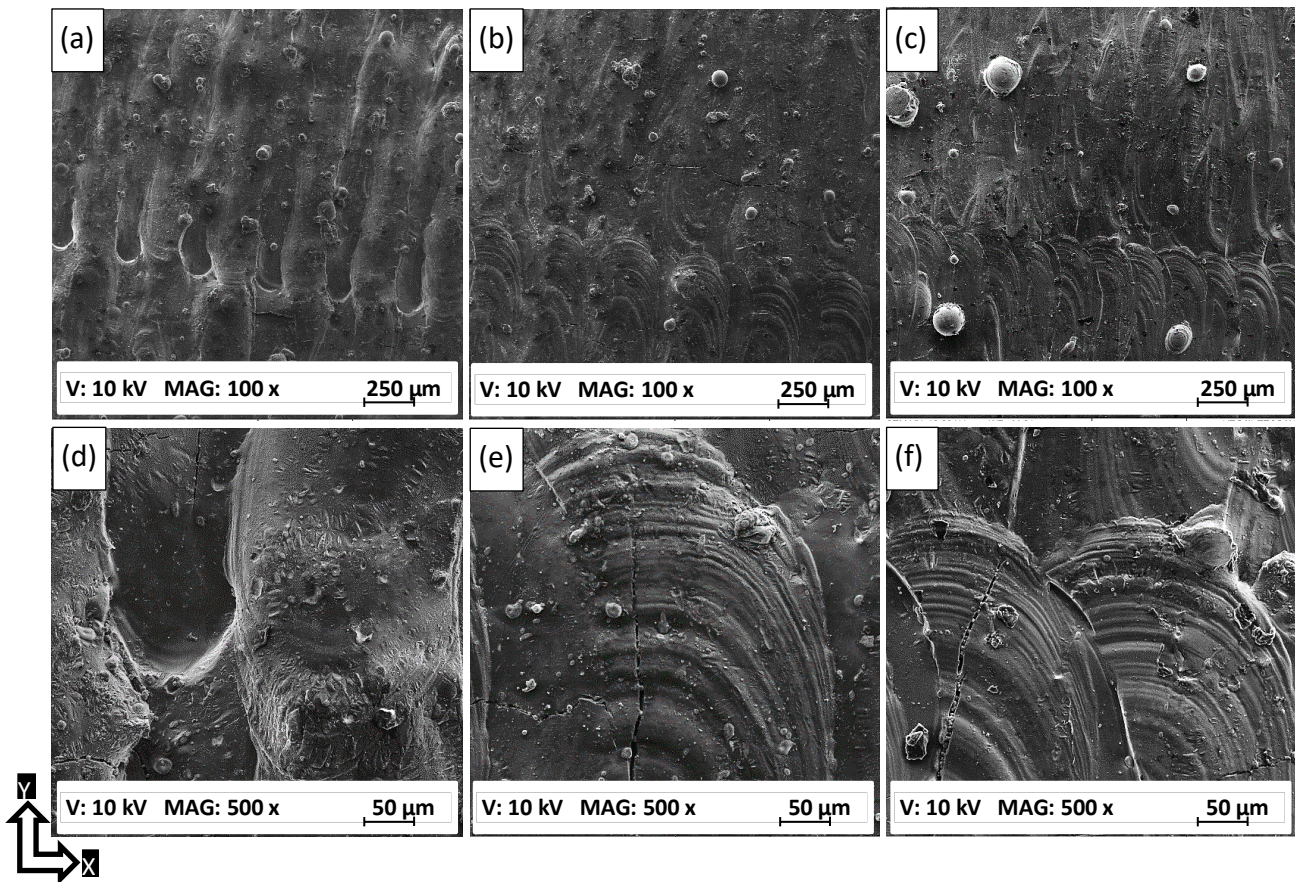


Figure 4-28 The SEM observations on the as-built surface of Al6061 samples; a, d) 7A, b, e) 14A, c, f) 1A.

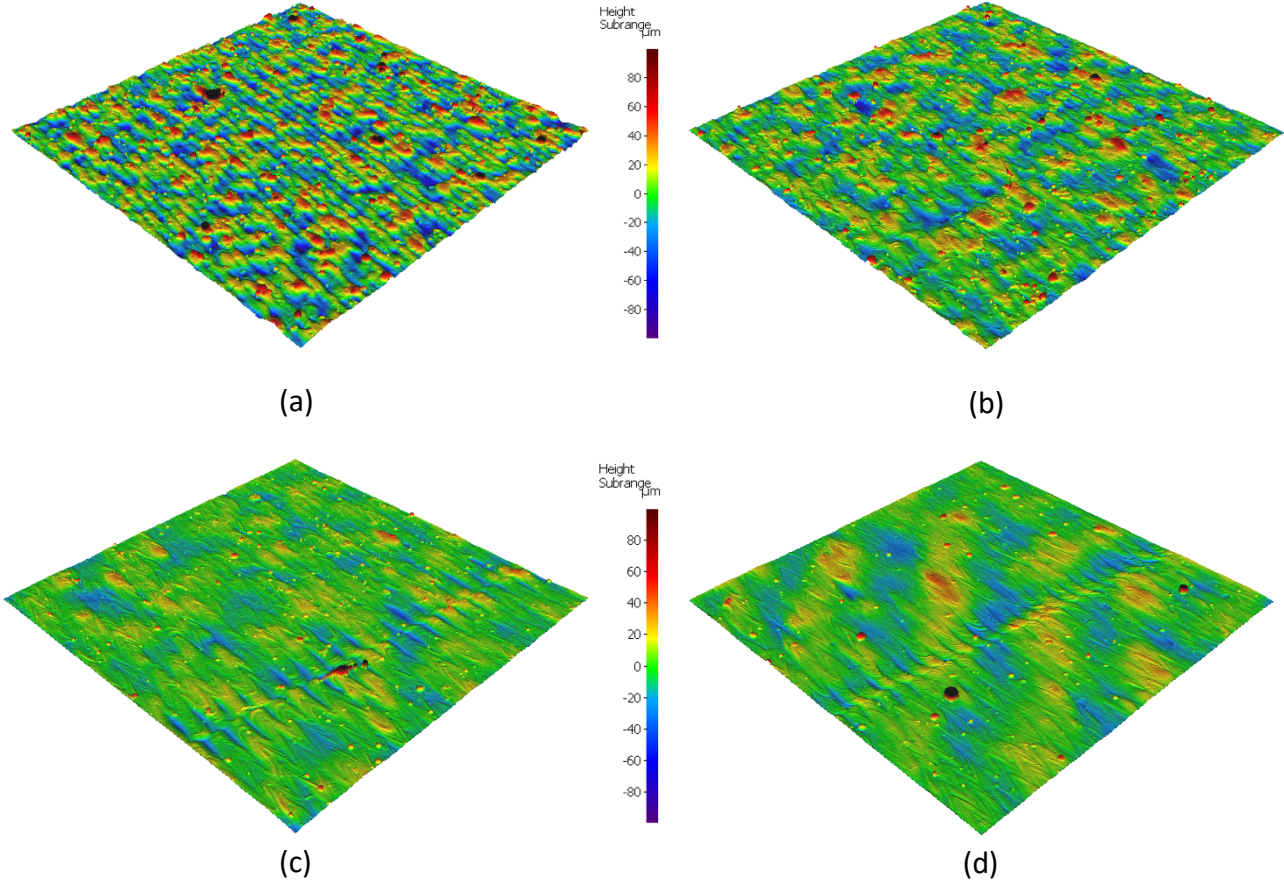


Figure 4-29 The 3D surface texture of the as-built Al6061 samples; a) 8A, b) 6A, c) 14A, d) 11A.

Interaction can be observed between scan speed and hatch spacing on the effect of surface roughness is shown in Figure 4-30. This further validates that the main mechanism effecting the surface roughness is the melt pool overlap.

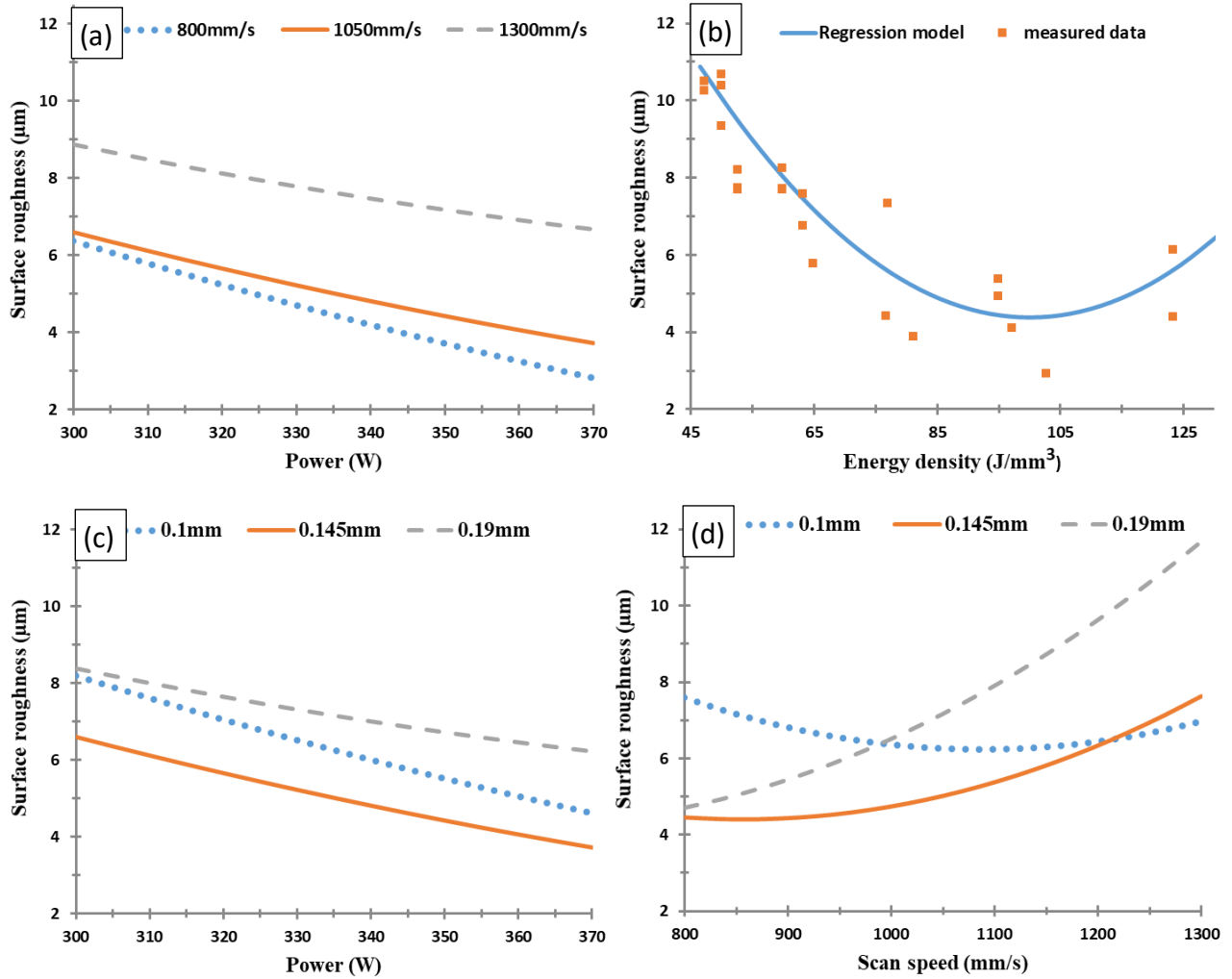


Figure 4-30 Effect of the SLM process parameters on surface roughness of the as-built Al6061 samples.

4.4.3. Dimensional accuracy

4.4.3.1. *AlSi10Mg*

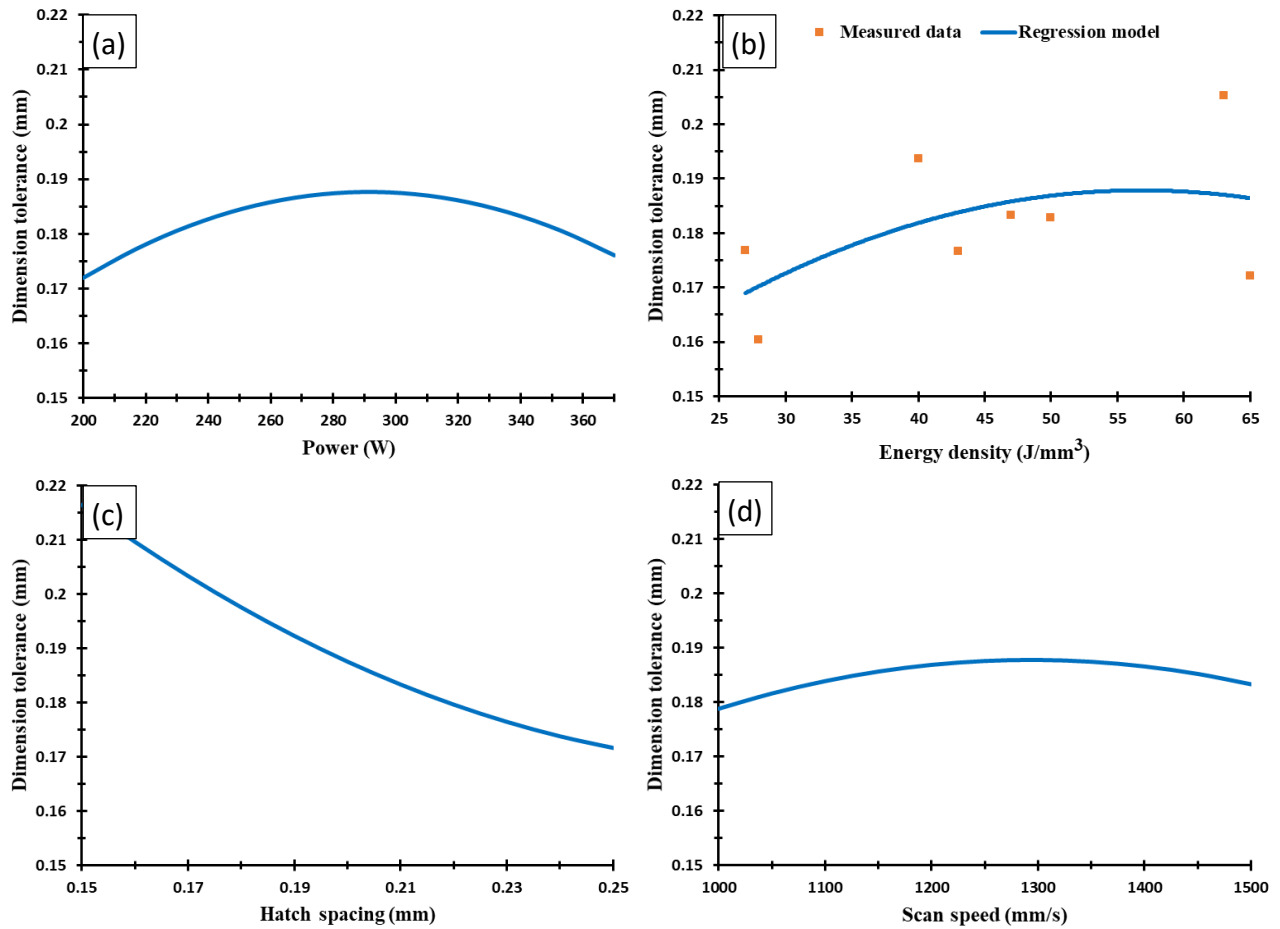


Figure 4-31 Effect of the SLM process parameters on dimension tolerance of the as-built AlSi10Mg samples.

From the CMM data, XY dimensional lengths and top surface flatness was evaluated for the as-build samples of AlSi10Mg and Al6061. As seen in Figure 4-31, AlSi10Mg samples showed dimension oversize in reference to the original design, showing no contracting upon completion of fabrication. With the observation of surface topology made in section 3.4.2, the oversize is mainly due the bonding of powder particles to the surface, which affects the stairstep profile [46]. The dimensional tolerance is measured to be 0.15mm to 0.195mm, where the main effect is shown to be hatch spacing.

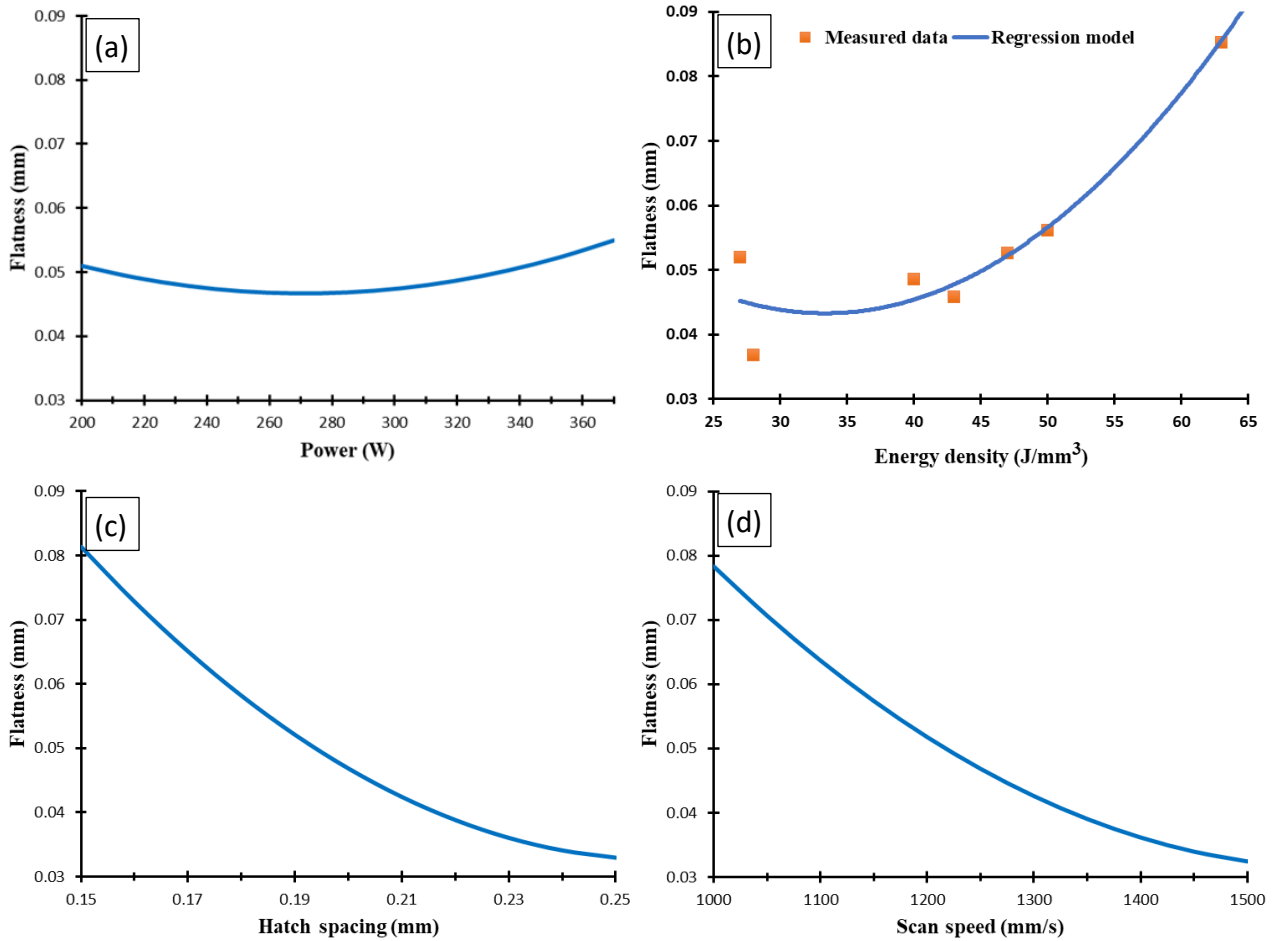


Figure 4-32 Effect of the SLM process parameters on surface flatness of the as-built AISi10Mg samples.

The flatness of the AISi10Mg samples are affected the most with scan speed and hatch spacing, as seen in Figure 4-32. Energy density also have good fit with flatness data.

4.4.3.2. Al6061

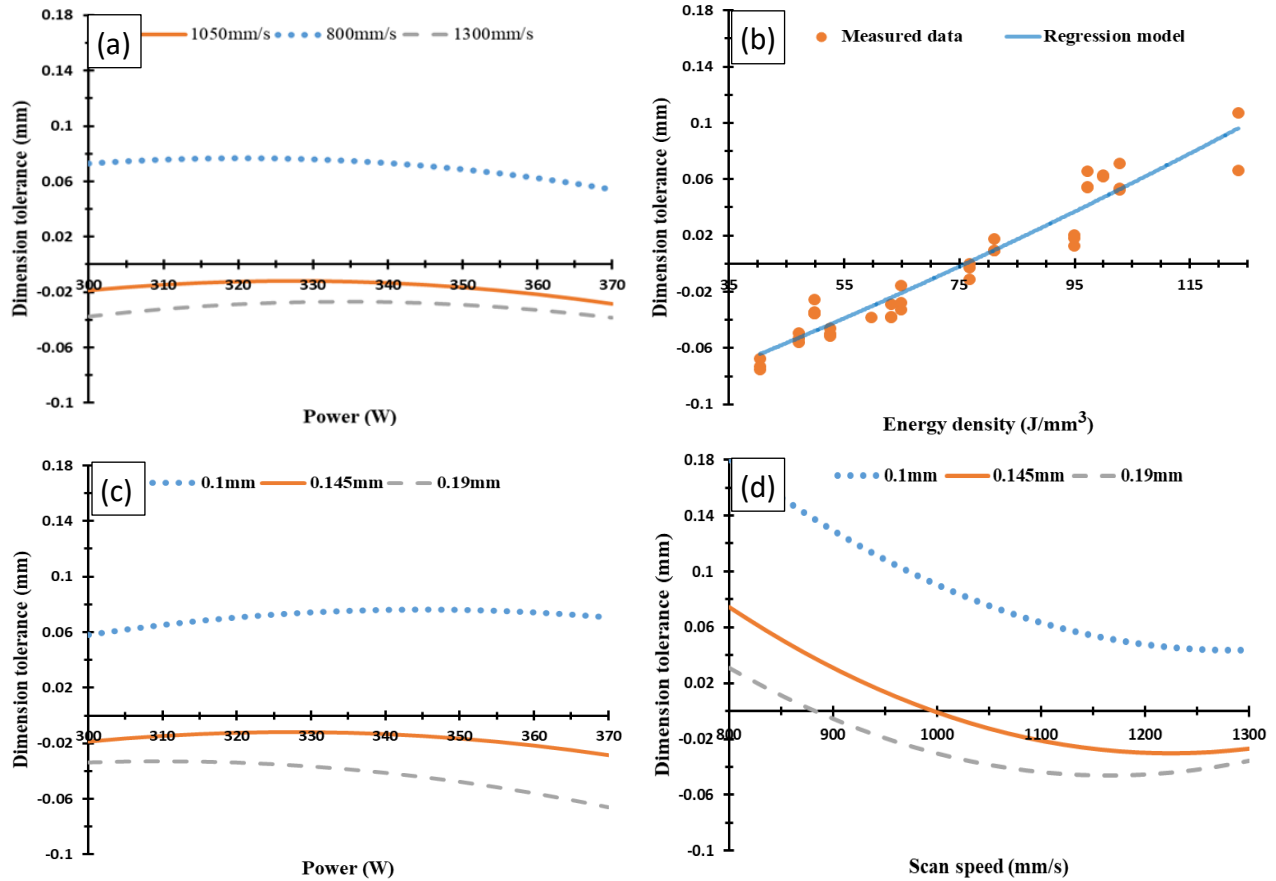


Figure 4-33 Effect of the SLM process parameters on dimension tolerance of the as-built Al6061 samples.

The as-built samples of Al6061 exhibits a different behaviour in dimensional accuracy comparing to that of AlSi10Mg. In Figure 4-33b, the XY lengths of the cube spans zero, indicating that the Al6061 samples goes through both expansion and contraction depending on the SLM process parameters. This is likely due to the change in melt pool dimension at different energy densities [46] as well as the high CTE of Al6061.

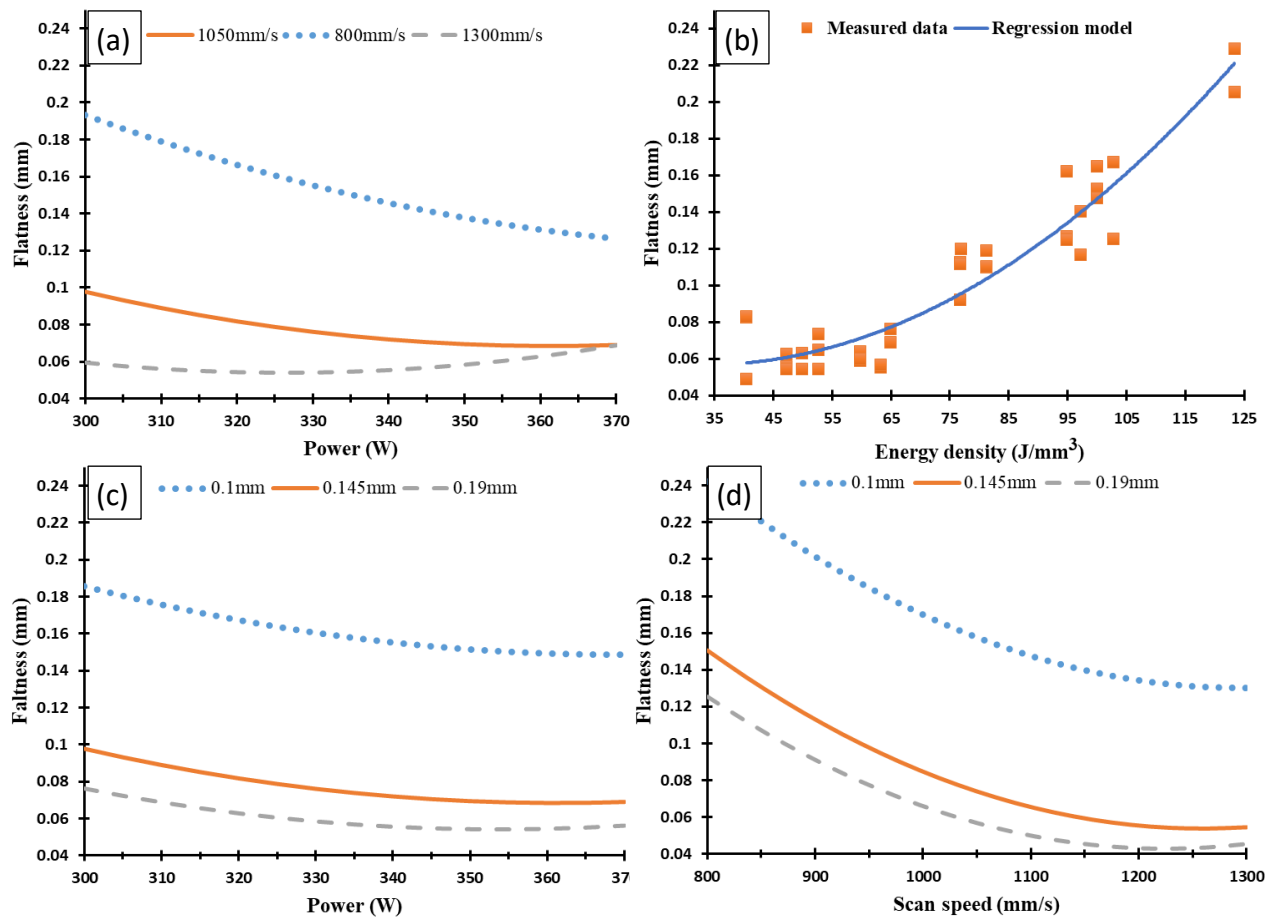


Figure 4-34 Effect of the SLM process parameters on surface flatness of the as-built Al6061 samples.

Surface flatness for Al6061 was found to be from 0.05mm – 0.24mm, which is significantly higher than the 0.035mm to 0.09mm of AlSi10Mg, Figure 4-34. This again is attributed to the high CTE of Al6061, which reduces the heat accumulated inside the part, thus creating higher thermal gradient across the part, increasing the thermal stress that manifests in the form of surface defects. Hot tearing on both the surface level as well as inside the part increases the surface waviness.

4.5. Optimal processing window

Part relative density, XY length tolerance, and surface roughness results were decided to be used for the development of an operating process parameter window for AlSi10Mg and Al6061.

The reasons for the choice of these three qualities are: (1) Mechanical properties such as the tensile strength, are closely affected by the internal defects of the part. Voids, pores, and internal cracks serves as nucleation sites for part's integrity failure to occur. By evaluating the part density, the tensile strength of the part can be reasonably predicted. This is further supported by the observation of the pattern of the curves reported in section 4.3 and section 4.4.1. (2) For the most part, mechanical properties such as hardness, tensile strength, and certainly microstructures, can be modified and improved during post process through heat treatment. Whereas physical defects such internal voids, pores, cracks, surface defects such as uneven melt, particle bonding, pits, cracks, and GD&T related error, are much more difficult to resolve.

In chapter 3, it was mentioned that response surface method was used to analyse the data coming from the DOE. The major benefit of RSM is the ability to relate the factors and response in a polynomial function, whereas traditional full factorial analysis would only give segmented linear relations. Using Minitab, contour maps were generated using analysis from RMS. From section 4.4, power and scan speed were found to be two fundamental process parameters with the most influence. Although hatch spacing was observed to have significant effect on surface roughness, majority of the interactive effect happened between power and scan speed. Since the final map for processing window will be created in 2-dimensional, therefore, in order

for the map to be robust and information clearly conveyed, two major process parameters will be chosen, in this case power and speed.

The contour maps of power and speed for length tolerance, relative density, and surface roughness, were overlapped at values for each quality to ensure a good combined quality for the process operating window.

Figure 4.5-1 showcase the optimal processing window along with the contour maps for AISi10Mg. Effective overlap for insurance of overall quality was chosen to be 5.5 μ m to 9 μ m surface roughness, 99.3% to 99.8% relative density, and +0.18mm to +0.2mm length tolerance. Hatch spacing was kept constant at 0.19mm for maximum overlap.

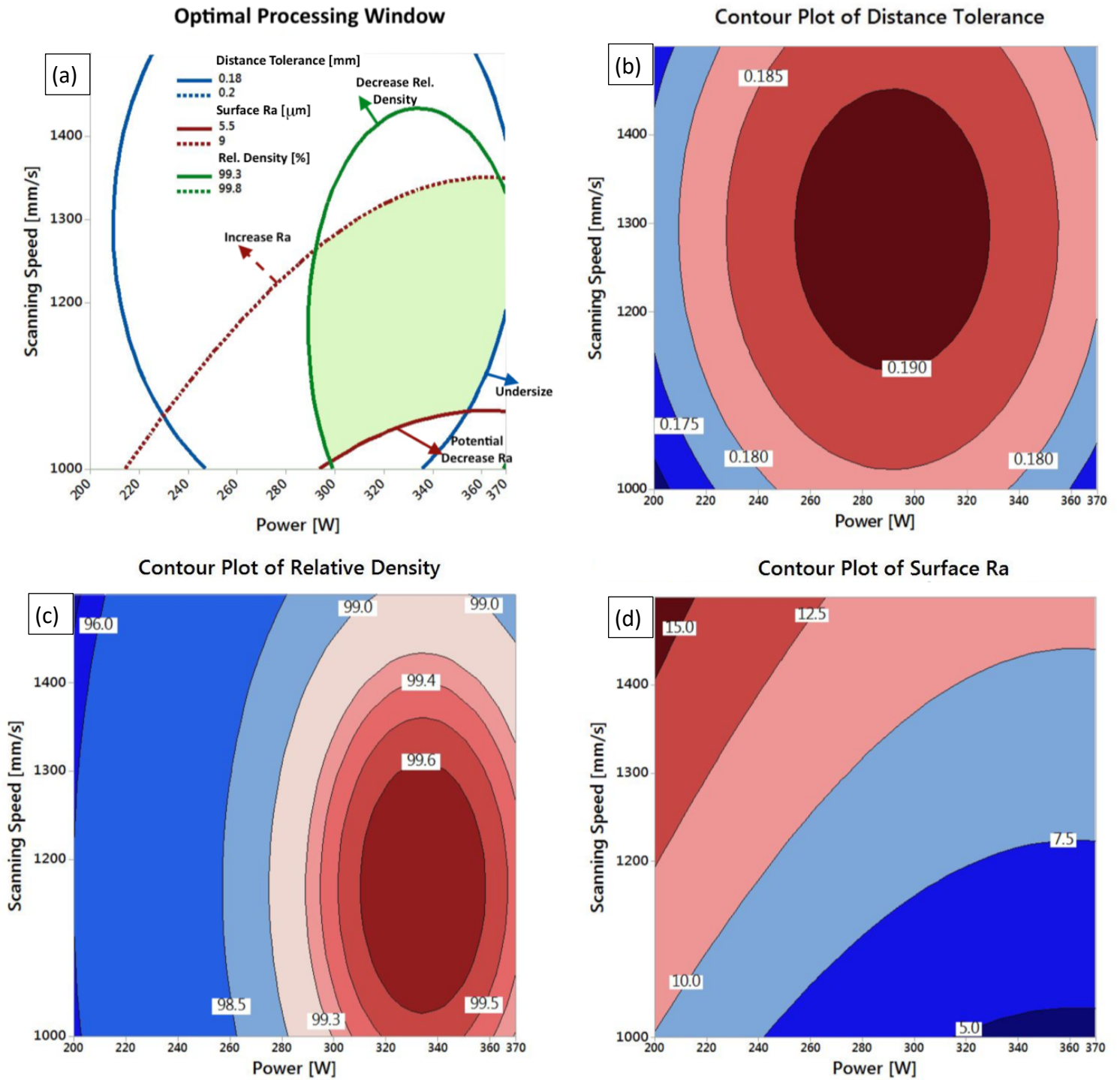


Figure 4.5-1 The optimal processing window generated for AISi10Mg at the hatch spacing value of 0.19 mm.

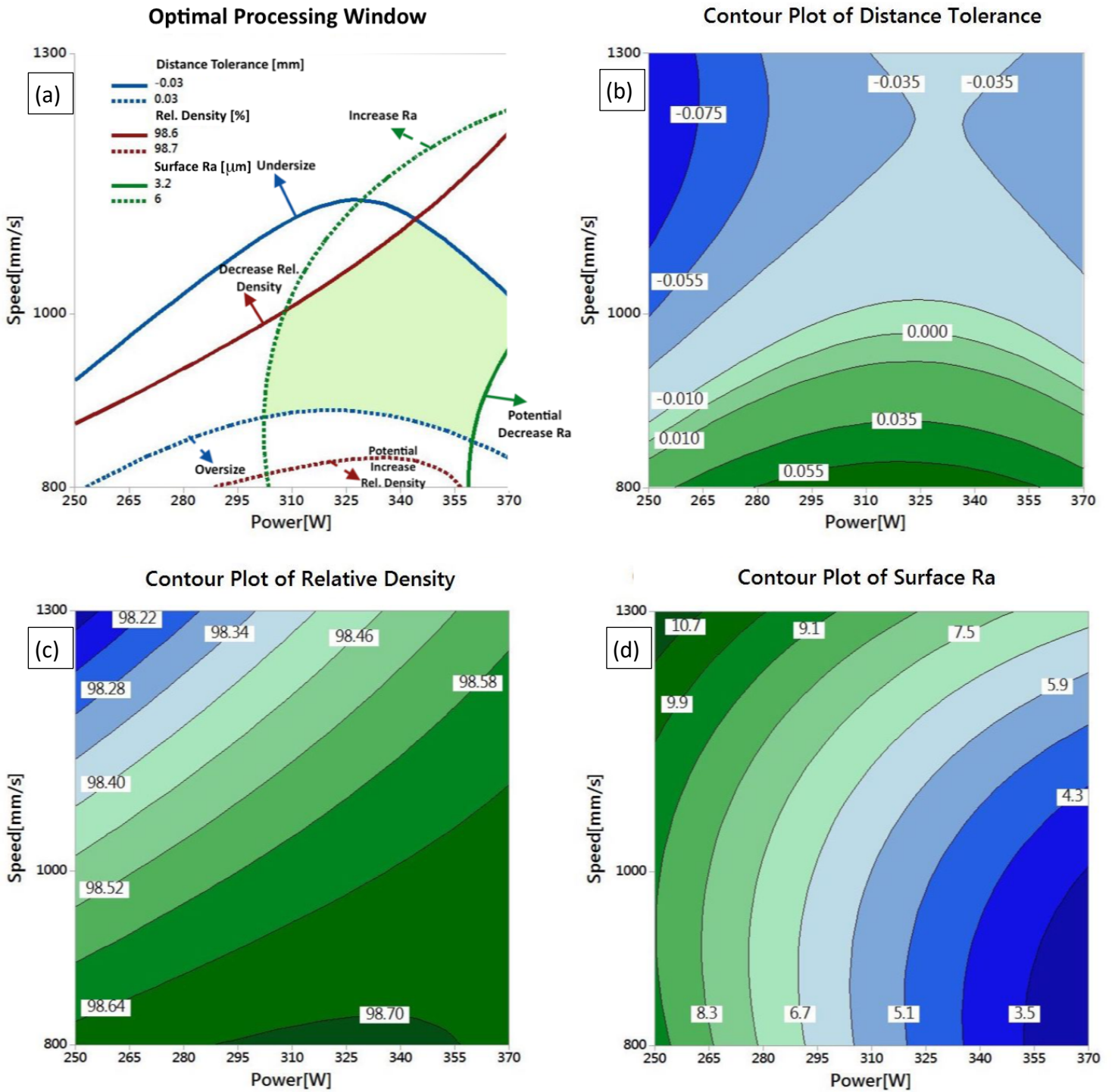


Figure 4.5-2 The optimal processing window generated for Al6061 at the hatch spacing value of 0.15 mm.

Similarly, the optimal processing window for Al6061, along with its contour maps are shown in Figure 4.5-2. Hatch spacing kept at 0.19mm, surface roughness between 3.2 μ m to 6 μ m, relative density between 98.6% to 98.7%. Since observed in Figure 4-33, the length tolerance for Al6061 spans zero, which means that with the correct combinations of process parameters, minimal dimensional errors can be obtained. Therefore, the contour map overlap was sure to include the length error range to span zero, of -0.03mm to 0.03mm.

5. Conclusion

A comprehensive study on the quality of parts fabricated from AlSi10Mg and Al6061 using SLM was conducted. The SLM process parameters and their relationship with parts' physical and mechanical properties were evaluated. The qualitative properties include: microstructures observation, microhardness, tensile strengths, relative density, surface roughness, and dimensional accuracy. Due to the differences in reflectivity of AlSi10Mg and Al6061, different optimal energy density was observed for each material for maximum relative density. $50\text{J}/\text{mm}^3$ – $60\text{J}/\text{mm}^3$ for AlSi10Mg for 99.7% relative density, and $102.8\text{J}/\text{mm}^3$ for Al6061 for 98.72% relative density. The energy density was further seen to be influential in producing optimal microstructures for AlSi10Mg, where relatively homogeneous equiaxed grains were formed with no balling effect and minimal hydrogen pores. Al6061 is comparatively more robust in its operational energy density range, as a larger SLM process parameter range settings were explored with no major incidents of inter porosities. However, due to the low Si content, no combinations of SLM process parameters were found to create parts from Al6061 without the formation of hot tearing. The mechanical tensile strength for the as-build Al6061 samples however, is comparable to that of the wrought metal, which prompts the conclusion that given applications of lesser requirements on fatigue life, the as-build Al6061 can be a good option. AlSi10Mg exhibits low CTE, with parts fabricated all being oversized by 0.15mm to 0.195mm due to particle bonding to the surface as well as the staircase effect inherent from the layer-wise production process. Al6061, in contrast, has a much higher CTE due to the low Si content, thus the range of dimension error was observed to be from -0.08mm to +0.1mm.

Regression models for the part qualities were generated from empirical work, and contour maps were made for the parts relative density, dimensional tolerance, and surface roughness. An optimal process window was created for AlSi10Mg and Al6061 from the overlaps of the contour maps for each material.

5.1. Future research suggestions

This work focused on the pursue and study of empirical modeling due to its accuracy to reflect the real-world system of high complexity, which is the case of SLM. However, empirical models are limited by the situations. For SLM, it is limited to each material being fabricated, as well as the SLM machines. Each material has different properties that dictates its behaviour during melting, solidification and ultimately its mechanical properties. SLM machines are all similar in principle, but fabrication results may differ from machine to machine due to background and unforeseen variables.

Pure numerical modeling can have difficulties in achieving accuracy when put into real-world applications, especially for modeling SLM as discussed in Chapter 2. However, combination of empirical and numerical modeling can be synergetic. It can be more robust as the numerical methods, as well as retaining accuracy from empirical modeling, as the example of staircase effect models tested in Chapter 2. This work hope to set the foundation for the future development of numerical models in regard to the parts quality for aluminum alloys.

Bibliography

- [1] Y. Huang, M. C. Leu, J. Mazumder, and A. Donmez, “Additive manufacturing: current state, future potential, gaps and needs, and recommendations,” *J. Manuf. Sci. Eng.*, vol. 137, no. 1, p. 14001, 2015.
- [2] K. V Wong and A. Hernandez, “A review of additive manufacturing,” *ISRN Mech. Eng.*, vol. 2012, 2012.
- [3] T. Wohlers and T. Gornet, “History of additive manufacturing,” *Wohlers Rep.*, vol. 24, no. 2014, p. 118, 2014.
- [4] D. D. Gu, W. Meiners, K. Wissenbach, and R. Poprawe, “Laser additive manufacturing of metallic components: materials, processes and mechanisms,” *Int. Mater. Rev.*, vol. 57, no. 3, pp. 133–164, 2012.
- [5] M. L. M. Sistiaga, R. Mertens, B. Vrancken, X. Wang, B. Van Hooreweder, J.-P. Kruth, and J. Van Humbeeck, “Changing the alloy composition of Al7075 for better processability by selective laser melting,” *J. Mater. Process. Technol.*, vol. 238, pp. 437–445, 2016.
- [6] T. . Martin, J.H.; Yahata, B.D.; Hundley, J.M.; Mayer, J.A.; Schaedler, T.A.; Pollock, “3D printing of high-strength aluminium alloys,” *Nature*, vol. 549, pp. 365–369, 2017.
- [7] M. Krol and T. Tański, “Surface quality research for selective laser melting of Ti-6Al-4V alloy,” *Arch. Metall. Mater.*, vol. 61, no. 3, pp. 1291–1296, 2016.
- [8] G. E. P. Box and R. D. Meyer, “An analysis for unreplicated fractional factorials,” *Technometrics*, vol. 28, no. 1, pp. 11–18, 1986.
- [9] J. Delgado, J. Ciurana, and C. A. Rodríguez, “Influence of process parameters on part quality and mechanical properties for DMLS and SLM with iron-based materials,” *Int. J.*

- Adv. Manuf. Technol.*, vol. 60, no. 5–8, pp. 601–610, 2012.
- [10] H. M. Gajera, “an Effect of Process Parameter of Direct Metal Laser Sintering (Dmls) Process on Dimensional Accuracy,” pp. 232–245, 2017.
- [11] C. Kamath, B. El-dasher, G. F. Gallegos, W. E. King, and A. Sisto, “Density of additively-manufactured, 316L SS parts using laser powder-bed fusion at powers up to 400 W,” *Int. J. Adv. Manuf. Technol.*, vol. 74, no. 1–4, pp. 65–78, 2014.
- [12] N. Kaufmann, M. Imran, T. M. Wischeropp, C. Emmelmann, S. Siddique, and F. Walther, “Influence of process parameters on the quality of aluminium alloy EN AW 7075 using selective laser melting (SLM),” *Phys. Procedia*, vol. 83, pp. 918–926, 2016.
- [13] L. Zhou, H. Pan, H. Hyer, S. Park, Y. Bai, B. McWilliams, K. Cho, and Y. Sohn, “Microstructure and tensile property of a novel AlZnMgScZr alloy additively manufactured by gas atomization and laser powder bed fusion,” *Scr. Mater.*, vol. 158, pp. 24–28, 2019.
- [14] D. Buchbinder, W. Meiners, K. Wissenbach, and R. Poprawe, “Selective laser melting of aluminum die-cast alloy—Correlations between process parameters, solidification conditions, and resulting mechanical properties,” *J. Laser Appl.*, vol. 27, no. S2, p. S29205, 2015.
- [15] D. Dai and D. Gu, “Tailoring surface quality through mass and momentum transfer modeling using a volume of fluid method in selective laser melting of TiC/AlSi10Mg powder,” *Int. J. Mach. Tools Manuf.*, vol. 88, pp. 95–107, 2015.
- [16] W. E. Frazier, “Metal additive manufacturing: a review,” *J. Mater. Eng. Perform.*, vol. 23, no. 6, pp. 1917–1928, 2014.

- [17] G. Strano, L. Hao, R. M. Everson, and K. E. Evans, "Surface roughness analysis, modelling and prediction in selective laser melting," *J. Mater. Process. Technol.*, vol. 213, no. 4, pp. 589–597, 2013.
- [18] J.-P. Kruth, M. Badrossamay, E. Yasa, J. Deckers, L. Thijs, and J. Van Humbeeck, "Part and material properties in selective laser melting of metals," in *Proceedings of the 16th international symposium on electromachining*, 2010.
- [19] P. Fischer, V. Romano, H.-P. Weber, N. P. Karapatis, E. Boillat, and R. Glardon, "Sintering of commercially pure titanium powder with a Nd: YAG laser source," *Acta Mater.*, vol. 51, no. 6, pp. 1651–1662, 2003.
- [20] S. Rahmati and E. Vahabli, "Evaluation of analytical modeling for improvement of surface roughness of FDM test part using measurement results," *Int. J. Adv. Manuf. Technol.*, vol. 79, no. 5–8, pp. 823–829, 2015.
- [21] R. I. Campbell, M. Martorelli, and H. S. Lee, "Surface roughness visualisation for rapid prototyping models," *Comput. Des.*, vol. 34, no. 10, pp. 717–725, 2002.
- [22] A. Mason, *Multi-axis hybrid rapid prototyping using fusion deposition modeling*. ProQuest, 2007.
- [23] D.-K. Ahn, S.-M. Kwon, and S.-H. Lee, "Expression for surface roughness distribution of FDM processed parts," in *Smart Manufacturing Application, 2008. ICSMA 2008. International Conference on*, 2008, pp. 490–493.
- [24] P. M. Pandey, K. Thrimurthulu, and N. V. Reddy*, "Optimal part deposition orientation in FDM by using a multicriteria genetic algorithm," *Int. J. Prod. Res.*, vol. 42, no. 19, pp. 4069–4089, 2004.

- [25] D. Manfredi, F. Calignano, M. Krishnan, R. Canali, E. P. Ambrosio, S. Biamino, D. Ugues, M. Pavese, and P. Fino, "Additive manufacturing of Al alloys and aluminium matrix composites (AMCs)," in *Light metal alloys applications*, InTech, 2014.
- [26] C. Galy, E. Le Guen, E. Lacoste, and C. Arvieu, "Main defects observed in aluminum alloy parts produced by SLM: From causes to consequences," *Addit. Manuf.*, 2018.
- [27] K. G. Prashanth, S. Scudino, A. K. Chaubey, L. Löber, P. Wang, H. Attar, F. P. Schimansky, F. Pyczak, and J. Eckert, "Processing of Al–12Si–TNM composites by selective laser melting and evaluation of compressive and wear properties," *J. Mater. Res.*, vol. 31, no. 1, pp. 55–65, 2016.
- [28] K. G. Prashanth, H. S. Shahabi, H. Attar, V. C. Srivastava, N. Ellendt, V. Uhlenwinkel, J. Eckert, and S. Scudino, "Production of high strength Al85Nd8Ni5Co2 alloy by selective laser melting," *Addit. Manuf.*, vol. 6, pp. 1–5, 2015.
- [29] T. DebRoy, H. L. Wei, J. S. Zuback, T. Mukherjee, J. W. Elmer, J. O. Milewski, A. M. Beese, A. Wilson-Heid, A. De, and W. Zhang, "Additive manufacturing of metallic components—process, structure and properties," *Prog. Mater. Sci.*, vol. 92, pp. 112–224, 2018.
- [30] D. Buchbinder, W. Meiners, N. Pirch, K. Wissenbach, and J. Schrage, "Investigation on reducing distortion by preheating during manufacture of aluminum components using selective laser melting," *J. Laser Appl.*, vol. 26, no. 1, p. 12004, 2014.
- [31] U. Tradowsky, J. White, R. M. Ward, N. Read, W. Reimers, and M. M. Attallah, "Selective laser melting of AlSi10Mg: Influence of post-processing on the microstructural and tensile properties development," *Mater. Des.*, vol. 105, pp. 212–222, 2016.
- [32] E. O. t Olakanmi, R. F. Cochrane, and K. W. Dalgarno, "A review on selective laser

- sintering/melting (SLS/SLM) of aluminium alloy powders: Processing, microstructure, and properties,” *Prog. Mater. Sci.*, vol. 74, pp. 401–477, 2015.
- [33] S. Siddique, M. Imran, E. Wycisk, C. Emmelmann, and F. Walther, “Influence of process-induced microstructure and imperfections on mechanical properties of AlSi12 processed by selective laser melting,” *J. Mater. Process. Technol.*, vol. 221, pp. 205–213, 2015.
- [34] C. A. Biffi, J. Fiocchi, and A. Tuissi, “Selective laser melting of AlSi10 Mg: Influence of process parameters on Mg₂Si precipitation and Si spheroidization,” *J. Alloys Compd.*, vol. 755, pp. 100–107, 2018.
- [35] M. Krishnan, E. Atzeni, R. Canali, F. Calignano, D. Manfredi, E. P. Ambrosio, and L. Iuliano, “On the effect of process parameters on properties of AlSi10Mg parts produced by DMLS,” *Rapid Prototyp. J.*, vol. 20, no. 6, pp. 449–458, 2014.
- [36] A. T. Sutton, C. S. Kriewall, M. C. Leu, and J. W. Newkirk, “Powder characterisation techniques and effects of powder characteristics on part properties in powder-bed fusion processes,” *Virtual Phys. Prototyp.*, vol. 12, no. 1, pp. 3–29, 2017.
- [37] Q. B. Nguyen, D. N. Luu, S. M. L. Nai, Z. Zhu, Z. Chen, and J. Wei, “The role of powder layer thickness on the quality of SLM printed parts,” *Arch. Civ. Mech. Eng.*, vol. 18, no. 3, pp. 948–955, 2018.
- [38] B. Cheng, S. Shrestha, and Y. K. Chou, “Stress and deformation evaluations of scanning strategy effect in selective laser melting,” in *ASME 2016 11th International Manufacturing Science and Engineering Conference*, 2016, p. V003T08A009-V003T08A009.
- [39] T. J. Fulcher, B.A.; Leigh, D.K.; Watt, “Comparison of AlSi10Mg and Al 6061 Processed

- Through DMLS,” in *Proceedings of the Solid Freeform Fabrication (SFF) Symposium*, pp. 404–419.
- [40] R. B. Uddin, S.Z.; Murr, L.E.; Terrazas, C.A.; Morton, P.; Roberson, D.A.; Wicker, “Processing and characterization of crack-free aluminum 6061 using high-temperature heating in laser powder bed fusion additive manufacturing,” *Addit. Manuf.*, vol. 22, pp. 405–415, 2018.
- [41] S. Maamoun, A.; Xue, Y.; Elbestawi, M.; Veldhuis, “Effect of Selective Laser Melting Process Parameters on the Quality of Al Alloy Parts: Powder Characterization, Density, Surface Roughness, and Dimensional Accuracy,” *Materials (Basel)*, vol. 11, no. 2343, 2018.
- [42] J. H. Tan, W. L. E. Wong, and K. W. Dalgarno, “An overview of powder granulometry on feedstock and part performance in the selective laser melting process,” *Addit. Manuf.*, vol. 18, pp. 228–255, 2017.
- [43] N. T. Aboulkhair, N. M. Everitt, I. Ashcroft, and C. Tuck, “Reducing porosity in AlSi10Mg parts processed by selective laser melting,” *Addit. Manuf.*, vol. 1, pp. 77–86, 2014.
- [44] L. Hitzler, J. Hirsch, M. Merkel, W. Hall, and A. Öchsner, “Position dependent surface quality in selective laser melting: Positionsabhängige Oberflächenqualität im selektiven Laserstrahlschmelzen,” *Materwiss. Werksttech.*, vol. 48, no. 5, pp. 327–334, 2017.
- [45] F. Calignano, D. Manfredi, E. P. Ambrosio, L. Iuliano, and P. Fino, “Influence of process parameters on surface roughness of aluminum parts produced by DMLS,” *Int. J. Adv. Manuf. Technol.*, vol. 67, no. 9–12, pp. 2743–2751, 2013.
- [46] X. Han, H. Zhu, X. Nie, G. Wang, and X. Zeng, “Investigation on selective laser melting

- AlSi10Mg cellular lattice strut: molten pool morphology, surface roughness and dimensional accuracy,” *Materials (Basel)*., vol. 11, no. 3, p. 392, 2018.
- [47] P. A. Hooper, “Melt pool temperature and cooling rates in laser powder bed fusion,” *Addit. Manuf.*, vol. 22, no. 548–559, 2018.
- [48] A. H. Maamoun, M. A. Elbestawi, and S. C. Veldhuis, “Influence of Shot Peening on AlSi10Mg Parts Fabricated by Additive Manufacturing.”
- [49] S. . Maamoun, A.H.; Elbestawi, M.; Dosbaeva, G.K.; Veldhuis, “Thermal Post-processing of AlSi10Mg parts produced by Selective Laser Melting using recycled powder,” *Additive Manuf.*, vol. 18, pp. 234–247, 2018.
- [50] Y. S. Lee, P. Nandwana, and W. Zhang, “Dynamic simulation of powder packing structure for powder bed additive manufacturing,” *Int. J. Adv. Manuf. Technol.*, vol. 96, no. 1–4, pp. 1507–1520, 2018.
- [51] P. Ma, K. G. Prashanth, S. Scudino, Y. Jia, H. Wang, C. Zou, Z. Wei, and J. Eckert, “Influence of annealing on mechanical properties of Al-20Si processed by selective laser melting,” *Metals (Basel)*., vol. 4, no. 1, pp. 28–36, 2014.
- [52] L. C. Liu, Y.J.; Liu, Z.; Jiang, Y.; Wang, G.W.; Yang, Y.; Zhang, “Gradient in microstructure and mechanical property of selective laser melted AlSi10Mg,” *J. Alloy. Compd*, vol. 735, p. 1414–1421., 2018.
- [53] A. J. C. Langford, J.I.; Wilson, “Scherrer after sixty years: A survey and some new results in the determination of crystallite size,” *J. Appl. Crystallogr.*, vol. 11, pp. 102–113, 1978.
- [54] P. S. Prevey, “X-ray Diffraction Characterisation of Residual Stresses Produced by Shot Peening,” in *Shot Peening Theory and Application*, 1990, pp. 81–93.

- [55] R. . Carter, L.N.; Attallah, M.M.; Reed, “Laser Powder Bed Fabrication of Nickel-Base Superalloys: Influence of Parameters; Characterisation, Quantification and Mitigation of Cracking,” in *Superalloys*, J. Huron, E.S., Reed, R.C., Hardy, M.C., Mills, M.J., Montero, R.E., Portella, P.D., Telesman, Ed. Pittsburgh, PA, USA, 2012, pp. 577–586.
- [56] J. Prashanth, K.G.; Eckert, “Formation of metastable cellular microstructures in selective laser melted alloys,” *J. Alloy. Compd.*, vol. 707, pp. 27–34, 2017.
- [57] J. Akram, P. Chalavadi, D. Pal, and B. Stucker, “Understanding grain evolution in additive manufacturing through modeling,” *Addit. Manuf.*, vol. 21, pp. 255–268, 2018.
- [58] S. J. Foster, K. Carver, R. B. Dinwiddie, F. List, K. A. Unocic, A. Chaudhary, and S. S. Babu, “Process-Defect-Structure-Property Correlations During Laser Powder Bed Fusion of Alloy 718: Role of In Situ and Ex Situ Characterizations,” *Metall. Mater. Trans. A*, vol. 49, no. 11, pp. 5775–5798, 2018.
- [59] “Standard Test Method for Surface Finish of Powder Metallurgy (PM) Products BT - Standard Test Method for Surface Finish of Powder Metallurgy (PM) Products.” .